COMPUTATIONAL ELECTROMAGNETIC STUDIES FOR LOW-FREQUENCY COMPENSATION OF THE REFLECTOR IMPULSE-RADIATING ANTENNA

THESIS

Casey E. Fillmore, Capt, USAF

AFIT-ENG-MS-15-M-011

DEPARTMENT OF THE AIR FORCE
AIR UNIVERSITY

AIR FORCE INSTITUTE OF TECHNOLOGY

Wright-Patterson Air Force Base, Ohio

AFIT-ENG-MS-15-M-011

COMPUTATIONAL ELECTROMAGNETIC STUDIES FOR LOW-FREQUENCY

COMPENSATION OF THE REFLECTOR IMPULSE-RADIATING ANTENNA

THESIS

Presented to the Faculty

Department of Electrical and Computer Engineering

Graduate School of Engineering and Management

Air Force Institute of Technology

Air University

Air Education and Training Command

in Partial Fulfillment of the Requirements for the

Degree of Master of Science in Electrical Engineering

Casey E. Fillmore, B.S.A.E.

Capt, USAF

March 2015

AFIT-ENG-MS-15-M-011

COMPUTATIONAL ELECTROMAGNETIC STUDIES FOR LOW-FREQUENCY

COMPENSATION OF THE REFLECTOR IMPULSE-RADIATING ANTENNA

THESIS

Casey E. Fillmore, B.S.A.E.
Capt, USAF

Committee Membership:

Dr. Peter J. Collins
Chair

Dr. Andrew J. Terzuoli, Jr.
Member

Maj Michael D. Seal, PhD
Member

AFIT-ENG-MS-15-M-011

Abstract

The reflector impulse-radiating antenna (IRA) is considered to meet the requirement for a wideband, directional antenna with short temporal response and small electrical footprint. Standard reflector IRA designs are modeled and performance is simulated using full-wave computational electromagnetic (CEM) software. Characterization of the standard designs reveals the possible existence of wide, frequency-independent backlobes containing nearly 40% of the radiated power at high frequencies. These undesirable backlobes have never been hypothesized, predicted or measured, likely due in part to their alignment outside the primary measurement planes.

At the lowest operating frequencies, the reflector IRA is unaffected by backlobes, but is characterized by low radiation efficiency and high resistive losses. Simulated studies are conducted to identify options for enhancing the low-frequency performance of the reflector IRA, including novel multi-arm feed structures and varied resistor distributions and values in the matching circuit component of the antenna design. Both techniques are predicted to provide viable options for enhancing and tuning the performance of the reflector IRA at low frequencies.

Table of Contents

List of Figures

Figure Page

List of Tables

COMPUTATIONAL ELECTROMAGNETIC STUDIES FOR LOW-FREQUENCY
COMPENSATION OF THE REFLECTOR IMPULSE-RADIATING ANTENNA

I. Introduction

Electromagnetic radiation in various man-made forms surrounds us, and indeed, modern society increasingly seems to rely on wireless methods for communication, data transfer, sensing and probing—the wireless nature of which begins and ends with an antenna to couple the electronic signals from hardware devices into open space and vice versa. Despite the myriad antenna designs and manufacturers available, and even a standards document for describing antenna performance [2], there remain some characteristics of interest that are not well-defined or standardized, and are rarely listed or described on specification documents. This complicates the task of finding the perfect antenna to suit certain demanding requirements. The basic problem addressed in the thesis is the need for an antenna exhibiting both a large bandwidth and short temporal response, all within a small electrical footprint.

1.1 Problem Description

The antenna qualities mentioned in the introduction that have yet to be standardized are primarily related to the time-domain performance of the antenna. One time-domain characteristic that is of particular interest is the inherent tendency for an antenna to ring. Ringing is a description of a time-dependent behavior of antennas which—just as a tuning fork continues to vibrate and emit sound waves well after it is initially struck—continue to radiate electromagnetic waves long after the driving signal or excitation has been suppressed. Ringing is highly undesirable in our appli-

cations and in many others, but not many antennas have been designed to minimize it. One class of antennas that shows promise in this area is the impulse-radiating antenna (IRA). More specifically, we are interested in the reflector IRA, an example of which is shown in Figure 1.1.
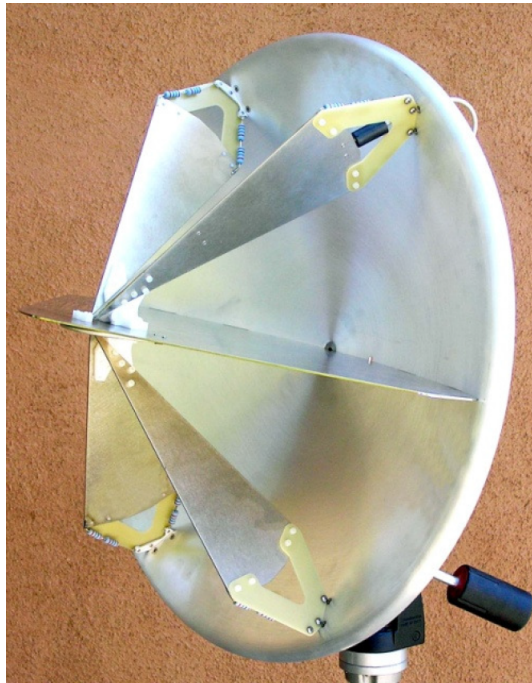
Figure 1.1. The Farr Fields model IRA-3Q is an example of an impulse-radiating antenna. It has an operating range from 250 MHz to 18 GHz and a time response less than 100 picoseconds [11].

The reflector IRA was first conceived by Baum in 1989 [5] for use in high-powered microwave and simulated nuclear electromagnetic pulse (EMP) hardness testing. The driving characteristic for which the reflector IRA has been designed and optimized is singular in nature: maximizing the radiated impulse-like field in a very narrow beam on antenna boresight when driven with a fast-rising step voltage. Based on the relationships between the time- and frequency-domain representations of signals, an antenna capable of radiating a very short-duration time signal must necessarily be capable of radiating over a very wide range of frequencies simultaneously. This ultra-wideband (UWB) characteristic is a proven capability of the reflector IRA design.

Suppression of ringing is also critical to maximizing the impulse-radiating performance of the antenna. Finally, the unique geometry of the antenna allows it to radiate in one direction, even at the lowest operating frequencies. All of these characteristics make it an attractive candidate for our needs, but radiating impulses is not the intended application. While the potential for other uses has been suggested [8, 12], especially given the UWB capability of the antenna, very little research has been performed to understand the antenna characteristics outside the impulse-radiating application.

The task at hand, then, is to fully characterize the reflector IRA design in the context of its frequency-domain performance. With an understanding of the antenna performance as currently implemented, studies can be performed to identify trade-offs in the design features to specifically enhance its low-frequency performance. To meet the requirement for compact electrical footprint, we are essentially interested in operating the antenna at the lowest frequencies and in the most compact form factor possible. If potential improvements are identified, optimization studies can be executed on the most promising parameters.

1.2   Research Motivation

There are two primary applications of immediate interest that motivate the use of an IRA. While not directly related, the two applications have similar requirements.

The first application is in radar cross section (RCS) measurement. The ability to accurately measure the RCS of aerospace vehicles in the very high frequency (VHF) radio band from 30-300 MHz has become increasingly important in recent years, and is an area where current capabilities are deficient in many respects. Typical antennas designed to operate at VHF frequencies often have omnidirectional radiation, which is undesirable for a measurement range. Directional VHF antennas are character-

ized by physically large and unwieldy, or highly resonant structures that exhibit the ring-down effect previously mentioned. As the antenna continues to radiate between pulses, the noise floor in the environment increases and has the consequence of reducing sensitivity and increasing uncertainty. This is especially problematic in RCS measurement, as many of the targets will have been designed to return as little energy as possible back to the antenna of the measurement radar. The National RCS Test Facility (NRTF) has investigated various antennas for use in VHF RCS measurements, and currently has a pair of reflector IRAs with 12-foot diameter reflectors. These were designed using the impulse-radiating application in mind, and because this class of antenna is still somewhat experimental in nature, a full performance specification is unavailable. Modeling and simulation to predict the performance of these specific antennas will ensure that they can be used safely as intended and provide additional insight into how to best employ them in the RCS measurement role.

Figure 1.2. 12-foot reflector IRAs built by Farr Fields LC for the NRTF.

The second application that motivates the use of an IRA is the Air Force Institute of Technology (AFIT) noise radar system. The availability of a wideband digital noise

radar has enabled multiple avenues of research, including through-wall imaging and radio frequency (RF) tomography, low probability of detection (LPD) and low probability of intercept (LPI) simultaneous communications and ranging [14], autonomous indoor navigation [25], and radio frequency distinct native attributes (RF-DNA) fingerprinting. While varying degrees of success have been demonstrated in these areas with the current noise radar system, a major limiting factor has been the lack of availability of a compact antenna that is both matched to the bandwidth of the radar and exhibits low ringing and waveform distortion. The noise radar currently operates in the low ultra high frequency (UHF) radio bands from 300-750 MHz, and the current implementation of an AFIT noise radar station makes use of a pair of printed circuit board (PCB) logarithmic-periodic (log-periodic) array antennas that are nearly matched on bandwidth, but which perform very poorly with respect to ringing and mutual coupling. An example of the AFIT noise radar station setup showing the log-periodic antennas is shown in Figure 1.3. Just as in RCS measurement, ringing contaminates the RF environment, which generally increases uncertainty in the data collected and processed for any of the noise radar applications. In addition to improving existing capabilities, use of an antenna that can radiate and receive very short-duration pulses will enable additional areas of research with the AFIT noise radar, such as investigation of the transient behavior of systems and devices under test in an RF-DNA fingerprinting context.

1.3   Research Goals and Scope

The overall goal of the thesis effort is to fully characterize the performance of the reflector IRA, as it is currently designed and implemented by *Farr Fields LC*, and to identify and recommend modifications that may be beneficial for adapting the reflector IRA design for use in RCS measurement in the VHF bands, and for use with
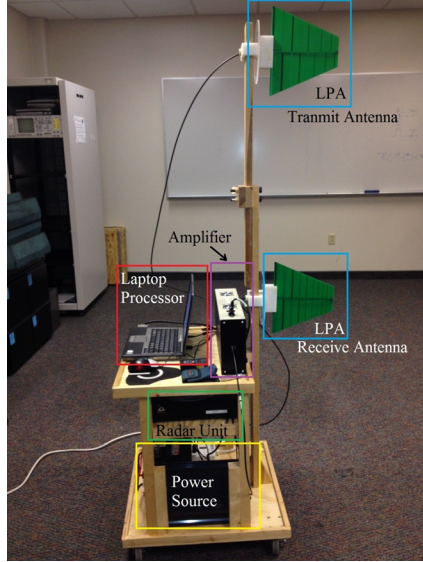
Figure 1.3. An AFIT noise radar station. The current transmit and receive antennas are log-periodic array antennas designed for operation from 400-1000 MHz.

the AFIT noise radar in the UHF bands. Two main lower-level goals will help in this effort.

- **Develop High Fidelity Computational Models.** Much of the theory and published research on reflector IRA performance incorporates assumptions which are not valid for a complete understanding of the antenna behavior, especially at the lowest frequencies. These analytical simplifications include the use of high-frequency physical optics approximations, the neglect of aperture blockage and feed structure diffraction effects, and the assumption of a perfect matching circuit at the end of the feed arms. Additionally, when characteristics such as beam widths and sidelobes have been considered analytically, numerically, and in experiment, the emphasis has been to look close to boresight only and not even for the full forward hemisphere. Finally, in published papers that made use of full-wave computational electromagnetic (CEM) codes to analyze reflector IRA performance, accurate representation of the matching circuit geometry and composition seems to have been ignored for ease of model

6

construction—typically only a single resistor is included at the end of each feed arm, and this is a gross misrepresentation of the nature of a realized reflector IRA. While CEM tools can never fully take the place of real-world measurement and observation, there appears to be here a void that can at least be partially explored with appropriate use of software. Therefore, the first major supporting goal for this thesis effort is to develop high fidelity, full-wave computational models of the reflector IRA. The geometry and layout of the antenna will be faithfully replicated to an unprecedented degree, and the model will be fully parameterized to allow for automated studies.

- **Apply Both Time- and Frequency-Domain Metrics.** The thesis discussion began by describing time-domain characteristics of antennas that are not yet defined or standardized; however, there have been some recent proposals to do just that [11]. To aid in a full antenna characterization, the second major supporting goal for this thesis effort is to apply these time-domain metrics along with and in comparison to the traditional frequency-domain metrics that are typically used to describe antennas. This requires the development of a set of algorithms to perform the necessary signal processing and computation on the results from the full-wave CEM simulations. A full antenna characterization using both metrics serves multiple purposes. First, the reflector IRA is typically described with time-domain metrics, so a direct comparison between computational models and published time-domain data on their physical counterparts aids in validating the use of the CEM models and verifying correct data processing techniques. Secondly, using both metrics will make this work useful to the both the impulse-radiating and traditional antenna user communities, and may demonstrate some fundamental relationships and trade-offs between time- and frequency-domain performance as various modifications are explored.

Even with the very brief introduction to the reflector IRA provided at this point, it is clear that there are several interrelated parameters and subsystems included in the design, so the scope of the investigation must be defined. The reflector IRA as a system includes a unique splitter balun design to achieve the necessary balanced feed and impedance matching conditions between signal source and antenna. The first major scope limitation is to omit this splitter balun, the cabling and its effects from the simulated antennas, and to focus instead on the antenna itself. Second, the initial scope for the thesis is limited to simulating reflector IRAs that either have been physically constructed or may be constructed following the same design guidelines as those built by *Farr Fields LC*. Additional details are provided in Chapter II.

1.4 Organization of Thesis

In this introductory chapter, the desired characteristics for a new antenna were discussed briefly, along with some of the challenges associated with obtaining such an antenna. The reflector IRA was identified as a candidate antenna to meet the requirements. Motivating applications for the use of an IRA or modified IRA were presented, and some additional areas of research that may be enabled or enhanced were also highlighted. The primary goals and overall scope of the research were discussed. Finally, the organization of the thesis document is presented as follows. Chapter II contains the information needed for the reader to understand the details of the research presented, including definitions of the chosen antenna metrics, an introduction to some typical UWB antennas and characteristics, and the specifics of the reflector IRA design. The research methodology is presented in Chapter III, and a detailed discussion and analysis of the results are found in Chapter IV. Chapter V contains the conclusions and recommendations for future work.

II. Background

2.1 Chapter Overview

With an idea of the end goal for the thesis, we now lay some groundwork to get there in a clear fashion. First, the notation, concepts and metrics used within the thesis are presented, including an introduction to some time-domain definitions and metrics. To flesh out the back story, a brief introduction to common UWB antenna designs and characteristics are described in the context of what has been tried or researched for the RCS measurement and AFIT noise radar applications introduced in Chapter I. Finally, a detailed system description of the reflector IRA and related studies are reviewed to orient the reader to the existing knowledge base, and to provide context for the contribution of this thesis work.

2.2 Terminology and Fundamental Concepts

Antennas are designed to radiate and receive electromagnetic waves. To answer the questions of "where?" and "how well?" we first need to define the appropriate coordinate system to describe the antenna performance in three dimensions. In all cases considered here, we are interested in the far field radiation characteristics of the antenna, so a spherical coordinate system is appropriate. The coordinate system and antenna alignment within it are shown in Figure 2.1.

The antenna being studied here is linearly polarized, with the electric-field vector oriented as shown in the figure, aligned with the y-axis. The direction of maximum radiation is in the $+z$ direction. With this in mind we define the following reference planes [2]:

- **E-plane:** the plane containing the electric-field vector and direction of maximum radiation. In this case, the E-plane is the y-z plane or $\phi = \pm 90°$ plane.

9
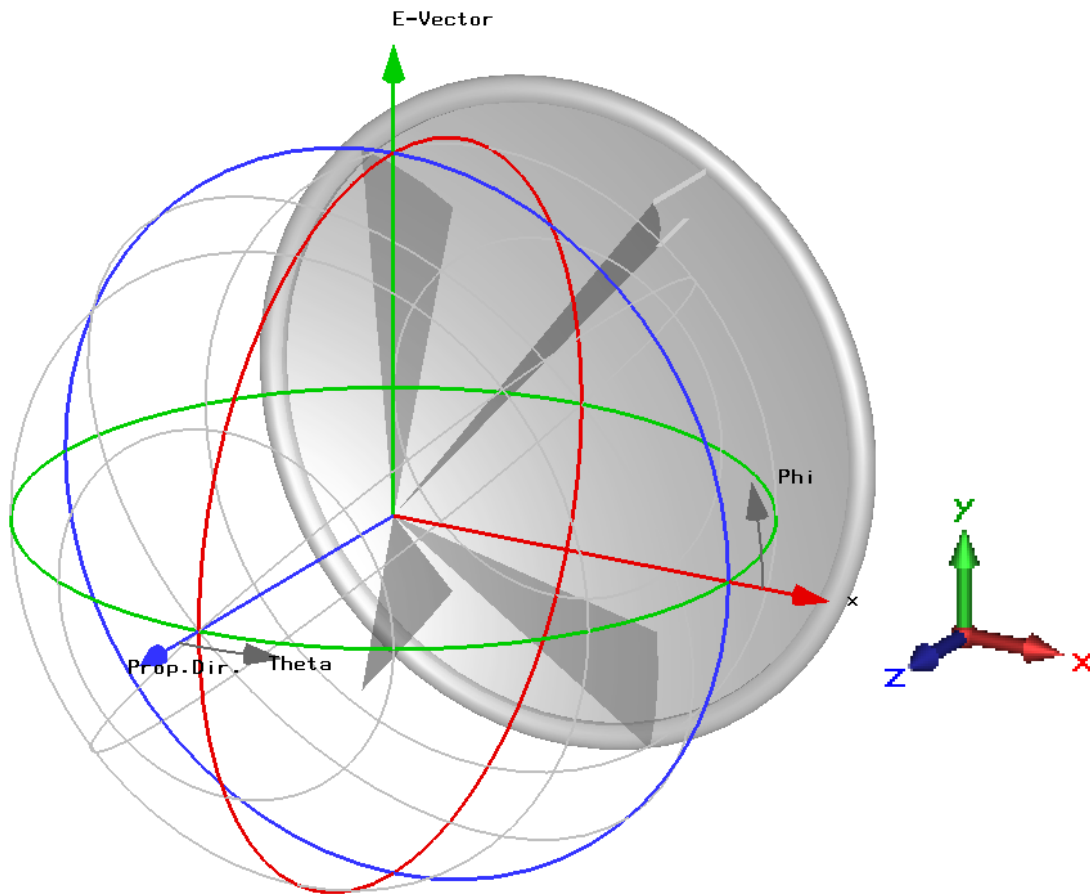
Figure 2.1. The spherical coordinate system and antenna alignment used throughout the thesis. The origin is placed at the focus of the paraboloidal reflector, which is also the apex of the feed structure in the standard IRA design.

- **H-plane:** the plane containing the magnetic-field vector and direction of maximum radiation. In this case, the H-plane is the x-z or $\phi = 0°$ plane.

Next, to describe how well the antenna radiates in a given direction into the far field as a function of frequency we will use the following standard terms [2]:

- **Gain:** the ratio of the radiation intensity in a given direction to the radiation intensity that would be produced if the power *accepted* by the antenna were isotropically radiated.

- **Realized Gain:** the gain of an antenna reduced by its impedance mismatch factor. In other words, the reference quantity for realized gain is the total *stimulated* power rather than just the accepted power.

10

- **Directivity:** the ratio of the radiation intensity in a given direction from the antenna to the radiation intensity averaged over all directions. In other words, the reference for directivity is the total *radiated* power.

- **Radiation efficiency:** the ratio of the total power radiated by an antenna to the net power accepted by the antenna from the connected transmitter.

- **Total efficiency:** the ratio of the total power radiated by an antenna to the stimulated power. Similar to the relationship between gain and realized gain, total efficiency accounts for the impedance mismatch factor or how much power is reflected at the antenna port.

All of these terms describe antenna performance in the frequency domain, considering the sinusoidal steady-state case. For UWB applications where the antenna may radiate multiple frequencies simultaneously, the time-domain performance of the antenna must be considered as well. We now look to some of the proposed definitions for how to describe and analyze an antenna in the time domain.

Baum, Farr [11] and others [24] have for many years applied linear, time-invariant (LTI) system theory to describe the performance of antennas using transfer functions and impulse responses, but there are various choices of normalization for these functions and as stated before, no standard terminology [2]. Following an approach based on power waves that is reminiscent of generalized scattering parameters [18], Farr has developed a simplified formulation that he has proposed for standardization [11]. The key results as they will be applied here follow.

The notation used by Farr will be copied here for consistency and ease of reference; in Chapter III the application of the formulas specific to the problem at hand is dealt with in more detail. First, after noting that the antenna behavior is different in transmission and reception, a fundamental law of reciprocity between the transmit and receive transfer functions in the frequency domain was derived:

$$\widetilde{F} = \frac{s\,\widetilde{h}}{2\pi\nu} = \frac{j\,\widetilde{h}}{\lambda}. \tag{1}$$

Here, the tilde indicates a frequency domain quantity; $\widetilde{F}$ is the transmit transfer function, $\widetilde{h}$ is the receive transfer function, $s = j\omega$ is the Laplace transform variable (although Fourier transforms can be and are also used where appropriate), ν is the velocity of propagation in the media (typically noted as c for free-space), and finally j and λ are the imaginary unit and wavelength in the media, respectively. Because the transmit and receive transfer functions are simply related, only one is required to describe the antenna performance, with the preference on $\widetilde{h}$ and its transform $h(t)$. Therefore, the antenna performance in transmission and reception in the frequency domain is formulated as follows:

$$
\begin{aligned}
\frac{\widetilde{E}_{rad}}{\sqrt{Z_{o2}}} &= \frac{s}{2\pi\nu}\frac{e^{-\gamma r}}{r} \quad \widetilde{h}\frac{\widetilde{V}_{src}}{\sqrt{Z_{o1}}} \\
\frac{\widetilde{V}_{rec}}{\sqrt{Z_{o1}}} &= \qquad\quad \widetilde{h}\frac{\widetilde{E}_{inc}}{\sqrt{Z_{o2}}},
\end{aligned}
\tag{2}
$$

where $\widetilde{E}_{rad}$ is the radiated electric field in a far field condition, $\widetilde{V}_{src}$ is the driving voltage signal at the port with reference impedance Z_{o1}, $\gamma = s/\nu = jk$, and r is the distance to the location where $\widetilde{E}_{rad}$ is observed. Z_{o2} is the characteristic impedance of the medium of propagation, and $\widetilde{E}_{inc}$ and $\widetilde{V}_{rec}$ are the incident field and received voltage at the port in reception.

Applying the inverse transform yields the results in the time domain:

$$
\begin{aligned}
\frac{E_{rad}(t)}{\sqrt{Z_{o2}}} &= \frac{1}{2\pi\nu r} \quad h(t) * \frac{dV_{src}(t')/dt}{\sqrt{Z_{o1}}} \\
\frac{V_{rec}(t)}{\sqrt{Z_{o1}}} &= \qquad\quad h(t) * \frac{E_{inc}(t)}{\sqrt{Z_{o2}}}.
\end{aligned}
\tag{3}
$$

Here, $t' = t - r/\nu$ is a retarded time to account for the propagation delay in transmission, and the "$*$" is a convolution operator. The receive impulse response waveform, $h(t)$, is the desired result that can be used to fully characterize the antenna performance. Functional dependencies were omitted for clarity in the notation, but it

is important to note that the impulse response is a vector quantity aligned with a particular field polarization, and also dependent on the observation location and time: $\vec{h}(\theta, \phi, t)$. We will look at the impulse response in the dominant polarization on antenna boresight, but analyzing the impulse response in other directions and polarizations may be of interest in some applications.

Now we briefly consider some desirable qualities for the $h(t)$ waveform. The metrics Farr derives from $h(t)$ directly are the peak value and the full width at half-max (FWHM), essentially the width of the main pulse [1]. However, not all antennas—even those with good time-domain performance—have such a strong, singular peak as the reflector IRA (which is the primary antenna in Farr's work). Wiesbeck suggests using the analytic impulse response, generated using the Hilbert transform of $h(t)$ [24]. The peak, FWHM and a ringing duration, τ_r, can be measured from the envelope of the analytic impulse response, which is denoted as $|h^+(t)|$. In brief, some of the values to look for in a good UWB antenna [24]:

- **Peak value of the envelope:** a high peak value is desirable.
- **Envelope width:** the FWHM should not exceed a few hundred picoseconds for high data rates in UWB communication or high resolution in radar applications.
- **Ringing:** the duration of ringing, defined as the time until the envelope has fallen from the peak value below a certain lower bound, should be negligibly small, i.e. less than a few envelope widths.

There are additional metrics to describe time-domain performance, but these are the main ones we will consider here.

2.3   Brief Introduction to Ultra-Wideband Antennas

In an excellent introductory article, Wiesbeck describes a few classes of antennas that facilitate charge acceleration, and thus radiation, over a very wide bandwidth [24]. We review them briefly now.

- **Traveling-Wave Antennas.** These are guided-wave antennas that offer smooth transitions from a transmission line type structure to free-space radiation. Examples are the Vivaldi and ridged horn antennas. These antennas offer high gain and narrower beams, but the low-frequency performance is limited by the physical size. Ludwig investigated Vivaldi antenna designs for the AFIT noise radar [15].

- **Frequency-Independent Antennas.** These antennas are characterized by shapes that are invariant to physical scaling, typically realized as constant-angular structures, such as biconical and bowtie antennas. Inevitably, the geometry must be truncated at some point, so physical size is again a limiting factor on low-frequency operation. Additionally, the radiation patterns are typically omnidirectional, which is undesirable for an RCS measurement range. Some AFIT noise radar applications may be possible with or even preferential to an omnidirectional antenna, but reduction of multi-path clutter with a directional antenna has been of greater importance in recent research areas.

- **Self-Complementary Antennas.** Fractal, sinuous and log-periodic spiral antennas are examples of self-complementary structures. The spiral antennas produce circularly polarized radiation, provided that the duration of the excitation signal is long enough to cover the entire radiating circumference. Multiple orthogonal radiation directions, some frequency-dependent time delays, and a rotation of the radiated field vector in time may make it more difficult to work with for the AFIT noise radar.

- **Multiple Resonance Antennas.** These are antennas formed of multiple narrow-band radiating elements, each covering a portion of the desired bandwidth. Log-periodic and some fractal antennas fall into this category. This type of antenna can be made fairly small with directional radiation, constant gain and beamwidths over the operating band, so it often appears as an attractive choice given our constraints. The AFIT noise radar is currently outfitted with log-periodic antennas, and the NRTF has tried using them, but as noted in the thesis introduction, the ringing effects can be problematic.

- **Electrically Small Antennas.** Wiesbeck notes that these antennas are "equally bad" with regard to UWB operation. Typical designs are various wide, rotationally symmetric monopoles above ground planes or planar monopoles integrated into printed circuit boards. A design like this might be interesting for the AFIT noise radar in an application where omnidirectional radiation was suitable.

Of course, not all antennas capable of UWB operation fit neatly into these categories. Some display elements of more than one category, and others may be in a class of their own. The reflector IRA may be the latter; we look at it next.

14

2.4 The Reflector Impulse-Radiating Antenna

Impulse-radiating antennas are designed for the radiation of high peak amplitude and very narrow pulses in time. In order to achieve this effect successfully, they must be capable of operating across a wide range of frequencies simultaneously and without dispersion. The initial concepts that led to the reflector IRA configuration were rooted in aperture theory. It was hypothesized that if the fields on an aperture could be "turned on" uniformly and instantaneously (as if driven with a step function), an impulse-like field could be radiated [5]. The reflector IRA design achieves this by employing a nondispersive transverse electromagnetic (TEM) feed structure that guides a spherical wavefront into a paraboloidal reflector. The reflector focuses the fields in the aperture and acts to differentiate the excitation signal. When employed in the impulse-radiating role, the excitation source is typically a fast-rising step voltage, the derivative of which is an approximate impulse. A final key feature of the reflector IRA is a resistive load or matching circuit between the feed structure and the reflector, which is intended to suppress spurious currents and reduce the late-time response.

The typical conically symmetric feed structure in a realized reflector IRA is composed of coplanar flat plates. The historical development first considered conical feed wires, which then developed into flat plates to reduce optical blockage of the aperture. The geometry of the coplanar plate feed arms can be described using the parameters shown in Figure 2.2.

As impedance matching is of critical importance in an UWB system, it is necessary to know or to be able to design the characteristic impedance of the TEM feed. An analytic solution was developed for the characteristic impedance of a single pair of arms, Z_{arm}. We use the formulation provided in [13]. First a β_0 angle is chosen; in a typical design this will be based on the geometry of the paraboloidal reflector, and will be defined as the angle from the focal point to the rim of the reflector. If this is

15
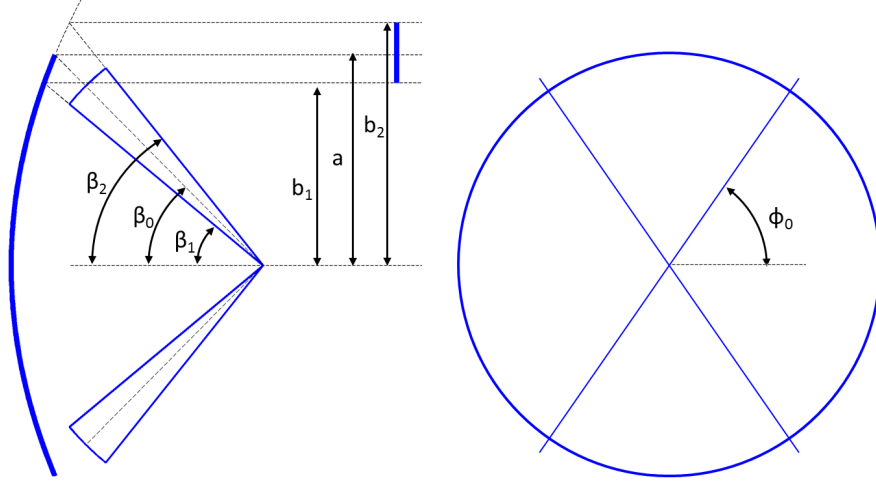
Figure 2.2. Geometric parameters that define the coplanar plate feed arms. The b-parameters are the projection of the β-angles into the aperture plane. The β_0 angle is typically chosen to align with the rim of the parabolic reflector.

the case and the focal-length-to-diameter ratio, f_d, is known, then β_0 can be solved from the equation of a parabola as

$$\beta_0 = \arctan\left(\frac{1}{2f_d - 1/(8f_d)}\right). \tag{4}$$

The desired impedance, Z_{arm}, will be related to the characteristic impedance of the medium by

$$Z_{arm} = Z_0 \frac{K(m)}{K(1-m)}, \tag{5}$$

where $K(m)$ is the complete elliptic integral of the first kind. This relationship is solved for the parameter m (numerically in MATLAB), and the remaining β angles are specified as

$$\begin{aligned}
\beta_1 &= 2\arctan\left[m^{1/4}\tan(\beta_0/2)\right] \\
\beta_2 &= 2\arctan\left[m^{-1/4}\tan(\beta_0/2)\right].
\end{aligned} \tag{6}$$

Note also that these relationships can be rearranged to solve the set of equations given any two of the following inputs: Z_{arm}, β_0, β_1, or β_2. Other formulations exist

that rely on the b/a ratios as shown in Figure 2.2 and/or a geometric impedance factor, $f_g = Z_{arm}/Z_0$, but for the purposes of this thesis the β angles and Z_{arm} were chosen to describe the geometry. This theory is for a single pair of feed arms; in practice, two pairs of feed arms are used and the ϕ_0 angle is used to describe the angle at which they are set to the horizontal plane of the antenna. Only in the case of $\phi_0 = 45°$ has the total feed impedance, Z_{feed}, been solved analytically [13]; the symmetry of the problem leads to $Z_{feed} = Z_{arm}/2$. For all other ϕ_0 angles the relationship must be calculated numerically or found experimentally, but once the relationship is known it is enough to simply specify the necessary Z_{arm}. To illustrate the general relationship between Z_{arm} and the resultant geometry, a progression of low to high impedance arms is shown in Figure 2.3. Low impedance arms are characterized by wider plate angles.
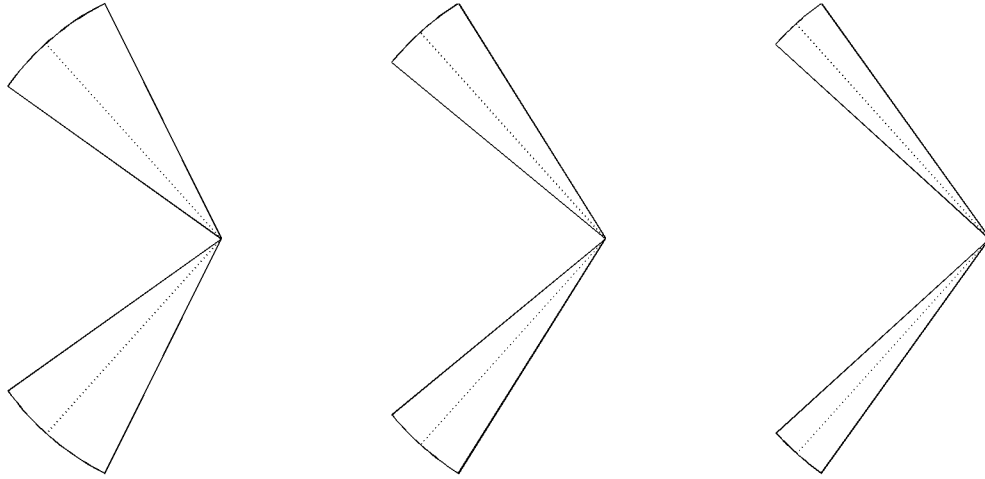
Figure 2.3. Side view of a set of conical coplanar plate feed arms for the reflector IRA, showing the relationship between Z_{arm} and the geometry. The Z_{arm} values shown are 300, 350, and $400\ \Omega$ from left to right; higher impedance values lead to narrower arms.

Now we take a brief aside related to the topics of impedance matching and feed design. In order to achieve reasonable arm geometries, high impedance arms are required. In the original reflector IRA designs, a pair of $400\ \Omega$ arms set to $\phi_0 = 45°$

were used to realize a $Z_{feed} = 200$ Ω. At this value, a 4:1 splitter balun design could be incorporated to match the typical 50 Ω cabling to the 200 Ω feed. The details of this splitter balun are not considered directly here, but its existence is noted, as it continues to be the standard for achieving the balanced feed for a reflector IRA and thus dictates designs with $Z_{feed} = 200$ Ω. A tool widely used in analyzing and locating impedance mismatches or discontinuities in transmission lines is a time-domain reflectometer, and time domain reflectometry (TDR) analysis is heavily used in experimental reflector IRA measurements. The concept of operation is much like a radar system, only completely contained within the transmission lines. Typically, a step pulse with a very fast rise time is propagated into the transmission line. Reflections are recorded in time can be analyzed both to understand the nature of any discontinuities as well as to physically locate the source of discontinuities in the lines. This capability makes the TDR a useful tool for assessing the quality of the splitter, and to aid in fine-tuning of the feed geometry, especially near the apex at the transition from coaxial cable to conical plate transmission line. As such, TDR measurements or responses are typically included in reports documenting experimental reflector IRA performance. Simulated TDR responses will also be used in this thesis. An example TDR response is shown in Figure 2.4.
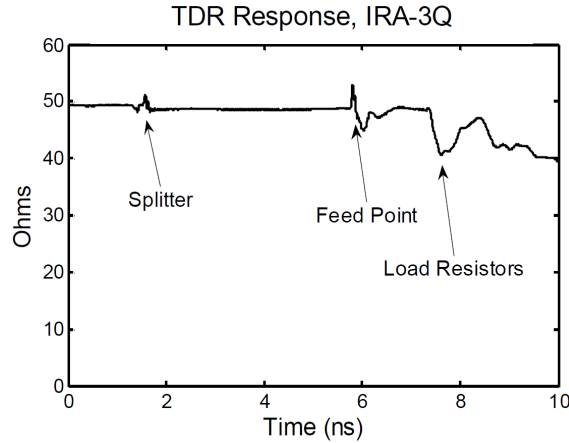
Figure 2.4. **Example annotated TDR response of the IRA-3Q from Figure 1.1 [1].**

2.5 Related Research

With an understanding of the basic layout and geometry of the reflector IRA as originally conceived, we can now discuss some historical research efforts to further improve reflector IRA performance. It is important to keep in mind that the primary motivation in all cases has been to maximize the radiated impulse-like fields.

- **Optimizing Feed Impedance and the ϕ_0 Angle.** As the basic assumption for reflector IRA performance is that of an aperture antenna, the field distribution on the aperture plays a large role in the nature of the radiated fields. A combination of theory [7] and numerical analysis [21] was used to optimize the feed geometry with the goal of maximum aperture efficiency at the early time of the excitation. The results of these efforts led to the current standard reflector IRA design, which has the feed arms set at $\phi_0 = 60°$. The aperture efficiency metrics do not take into account the effects of field interactions with the feed structure.

- **Empirical Experiments.** Building on the improved $\phi_0 = 60°$ design, a series of optimization experiments was performed with stated goals of further improving effective gain, reducing cross-polarized coupling, sidelobes, and reducing the reflections seen in the TDR measurements at the end of the feed arms [9]. A few of the findings are implemented as standards in the current commercial design, including the addition of a ground plane. Other experiments were deemed less successful, such as adding absorber foam to eliminate negatively polarized field contributions on the aperture. One key area of investigation in this report was the composition of the matching circuit elements; different types of resistors and inductive elements were tried in various configurations. While all the details of these particular investigations are not available in the report, the primary metric for assessing the performance of these modifications was the nature of the TDR response. More thoughts on this will be discussed in Chapter IV.

- **Novel Feed Arm Shapes.** Some of the more recent investigations on reflector IRA performance have focused on the feed structure. Various shapes deviating from the angular symmetry of the current design have been investigated, primarily with use of CEM software. Various tapers, β-angles, ϕ-angles, and Vivaldi-type feeds have been simulated [16], including a rather unique design that could be called a "back-to-back" Vivaldi taper [23]. In many cases, the modifications claim to bring performance improvements. However, various metrics and methodologies are in play which make comparison difficult, and not much in the way of experimental data is available to support these claims.

19

Having now briefly discussed the state of reflector IRA research topics, we address the context and contribution of the thesis. First, a primary goal is to understand the current reflector IRA design more thoroughly in a frequency domain context, and to use CEM tools to provide accurate predictions. This requires a build-up approach and careful attention to the details of the simulation and model antenna. Only after developing an understanding of the current antenna behavior will more exotic options be considered for performance improvement. Even so, with a desire to build and test these antennas, manufacturability becomes a concern. Finding performance enhancements within the current canonical geometries will therefore be preferred over complex new shapes of feed arms.

2.6   Chapter Summary

The groundwork has now been laid to begin describing the full details of the thesis research. The metrics that will be used to analyze the simulated antennas have been specified, and the UWB context in which the reflector IRA is conceived has been briefly introduced. The detailed geometry used to describe the antenna is made clear, and these parameters will be referenced heavily in Chapters III and IV. Some recent research topics related to the reflector IRA also give context to the research presented here.

III. Methodology

3.1   Chapter Overview

Having established the terminology and concepts necessary to understand the reflector IRA, its application and analysis in the time domain, we now focus on the detailed methodology of the thesis research. The choice of CEM tool and solver are considered, based on the desired data outputs. A set of simulation experiments designed to validate the choice of code and antenna modeling method is presented; the results indicate very close agreement with both analytical solutions and published measurements. The overall experimentation strategy is introduced to lay the groundwork for the results and analysis in Chapter IV.

3.2   Choice of Modeling Method

Of the CEM software suites available at AFIT, one stands out due to its comprehensive set of solvers and widespread use in the commercial sector: Computer Simulation Technology (CST) Microwave Studio (MWS)®. CST provides a full-wave three-dimensional (3D) electromagnetic (EM) simulation in a fairly user-friendly package. Because one of the thesis goals is to apply time-domain metrics to the antenna analysis, there is only one solver module within CST capable of generating the necessary time-dependent signals and field data: the Transient Solver, sometimes referred to as the time domain (TD) solver. As previously discussed, TDR analysis is widely used in the experimental evaluation of the reflector IRA, and a simulated TDR capability comes naturally with the TD solver. This simulated TDR is one of the primary tools for analyzing the feed structure and overall behavior of the reflector IRA models developed for this thesis. For optimizations and studies that do not require time domain results up front, the frequency domain (FD) solver module provides the capability to

perform more time-efficient simulations for a narrower frequency range. Results from the FD solver are also used for cross verification and an indication of the reliability and consistent behavior of the simulated antennas.

3.2.1 Transient Solver Overview.

In brief, the Transient solver in CST calculates the development of fields through time at discrete locations and at discrete time samples. The numerical method involved is called the Finite Integration Technique (FIT), and is based on a discretization of the integral forms of Maxwell's equations [3]:

$$
\begin{aligned}
\oint_{\partial A} \vec{E} \cdot d\vec{s} &= -\int_A \frac{\partial \vec{B}}{\partial t} \cdot d\vec{A}, & \oint_{\partial A} \vec{H} \cdot d\vec{s} &= \int_A \left(\frac{\partial \vec{D}}{\partial t} + \vec{J} \right) \cdot d\vec{A}, \\
\oint_{\partial V} \vec{D} \cdot d\vec{A} &= \int_V \rho \, dV, & \oint_{\partial V} \vec{B} \cdot d\vec{A} &= 0.
\end{aligned}
\tag{7}
$$

The resulting Maxwell's Grid Equations are solved as sets of matrix equations with a time-stepping update scheme. Some additional enhancements CST claims over traditional Finite Difference Time Domain (FDTD) methods are techniques to achieve more accurate modeling of complex boundaries. FDTD is typically limited to a staircase approximation of a complex boundary; CST employs in concert with the Finite Integration Technique methods known as the *Perfect Boundary Approximation* and *Thin Sheet Technique* which maintain the advantage of Cartesian grids while allowing accurate modeling of curved surfaces and thin perfect electric conductor (PEC) sheets [3].

3.2.2 Solver Settings Considerations.

It is important to discuss some of the initial choices on solver settings and model construction that remain consistent throughout all the simulations. In this subsection
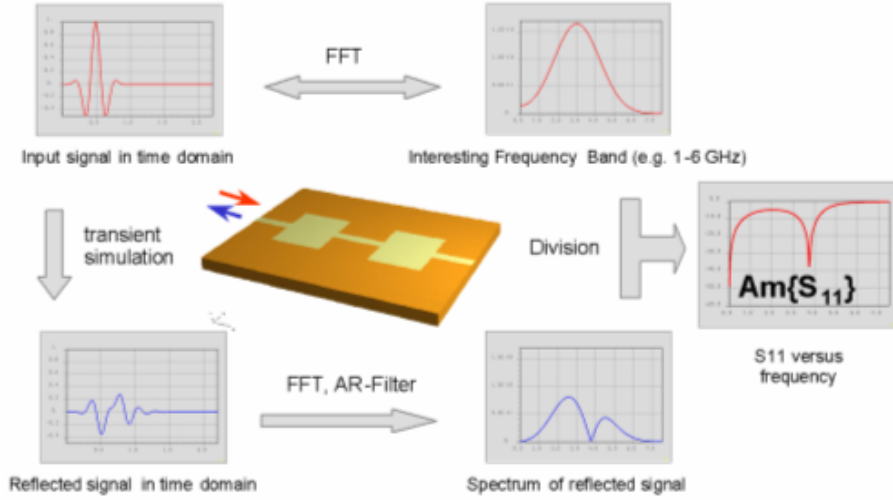
Figure 3.1. Generic CST workflow for calculating frequency-dependent data from time signals [4].

and the next, we look at some of the methods and settings that serve as the baseline for the simulation methodology, as well as any underlying assumptions that must be addressed. As more detailed models are introduced in Chapter IV, additional settings and assumptions are discussed as appropriate. The following list details some considerations in setting up the simulation domain.

- **Frequency limits.** Considering only the case of the AFIT noise radar application for a moment, there are two main drivers for the choice of frequency limits within the simulation: the operating range of the noise radar, and a desire to closely replicate a realistic band-limited impulse response measurement using standard cables and equipment. The low-frequency limit for the noise radar is about 300 MHz, and most standard cables and devices will begin to have degraded performance above 18 GHz. CST documentation recommends including some additional bandwidth outside the range of interest, so the upper limit is chosen to be 20 GHz. The choice of frequency limits also drives nearly every other simulation consideration to be discussed.

- **Excitation signal.** The TD solver extracts frequency-dependent data through Fourier transforms of the time signals (Figure 3.1), therefore the excitation signal must be spectrally matched to the desired frequency limits. By default, the solver generates appropriate excitation signals simply based on the chosen frequency limits, but there are some additional considerations. Defining the lower frequency limit at zero can speed up simulations by employing a short-duration Gaussian pulse that may reduce the overall number of time steps required. However, this baseband pulse will have a non-zero direct current (DC) component, and antennas cannot radiate a DC signal to the far field [10]. For simulating antennas and structures that tend to store some energy, reducing the DC and low frequency content can speed up the simulation, as the field energy in the domain dissipates faster. So, especially if very low frequencies are not required, an appropriate signal can be generated that reduces or eliminates the DC component of the signal. The trade-off with this strategy is that the duration of the excitation signal is typically increased significantly, which drives the total number of time steps required. An example is shown in Figure 3.2, where the excitation duration is nearly doubled when the lower frequency limit is set at 100 MHz instead of zero. One additional consideration drives the final choice for this thesis work: the simulated TDR can only be employed with a baseband Gaussian pulse or a fast-rising step signal (sometimes called a TDR pulse in this context). The TDR pulse is not well-behaved for domain transformations, so to generate all the required data and use the simulated TDR analysis simultaneously, the baseband pulse for 0-20 GHz is the appropriate choice. As a final note, user-defined excitation signals can be employed if the absolute performance of the antenna or device relative to a given input is of greater interest than simply assessing the general frequency-dependent characteristics.
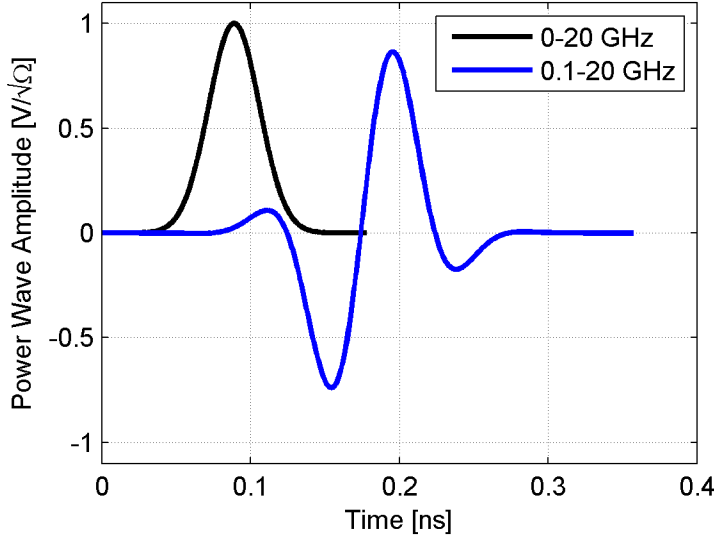
Figure 3.2. The excitation signal duration depends on frequency limits, and has the potential to impact the duration of the entire simulation. A 0-20 GHz Gaussian pulse is used for the majority of the thesis work.

- **Mesh.** The simulation domain is discretized by an orthogonal hexahedral mesh, and the computational effort is directly proportional to the number mesh cells in the domain. The upper frequency limit drives the required spacing or resolution of the mesh. A mesh that is too coarse will result in numerical dispersion and potential instabilities; a finer mesh increases accuracy but leads to a larger number of mesh cells for a fixed size model. Consider also, that even though the excitation signal is defined for 0-20 GHz, there will be some energy in frequencies above 20 GHz and numerical stability must still be ensured. This is accomplished automatically by the solver in choosing an appropriate maximal stable time step, which is inversely proportional to the size of the smallest mesh cell. So, while small mesh cells lead to a larger numerical effort, they also help to increase the maximal time step (to a point), which then reduces the total number of simulated time steps and simulation duration. Finding the most efficient trade between mesh cells and simulation duration was never explored during this thesis work; instead the choices for mesh definition were

25

made to ensure accurate results. More details will be discussed when describing the simulation experiments, but the majority of simulations used $\lambda/60$ mesh spacing at 20 GHz near the model and $\lambda/10$ in the surrounding space.

- **Domain size and boundaries.** The computational domain boundaries must be specified with care. For a radiation problem, sufficient open space around the antenna must be included in the computational domain, relative to the lowest frequencies of interest. This is to guarantee adequate angular and phase sampling around the domain for accurate near-field to far-field transformation, though the details of the algorithms employed in CST are not known. This introduces an additional trade-off between simulation feasibility and desired accuracy, as a domain sized appropriately for UHF wavelengths but meshed finely enough to support 20 GHz signals will have a massive number of mesh cells. The specific boundary settings and any caveats will be discussed for each simulation experiment, where appropriate. Additionally, the estimated reflection levels from the boundary layer can be specified; for all simulations in this thesis the settings were adjusted from the default -40 dB to an estimated -60 dB reflection. The increased computational cost is unknown, but is assumed to be insignificant compared to the other mesh and domain size considerations.

- **Symmetry conditions.** Much of the solver choices made thus far have a net effect of driving up the computational costs significantly. However, symmetry planes are used where appropriate to reduce the complexity of the model. Based on the geometry and electromagnetic behavior of the ideal reflector IRA, two symmetry planes can be defined that reduce simulation size by a factor of four. The E-plane of the antenna is defined with a magnetic symmetry condition, and the H-plane is defined with an electric symmetry condition (Figure 3.3). Some initial trials were conducted with and without the symmetry conditions in place

26

to verify that they were appropriately defined.
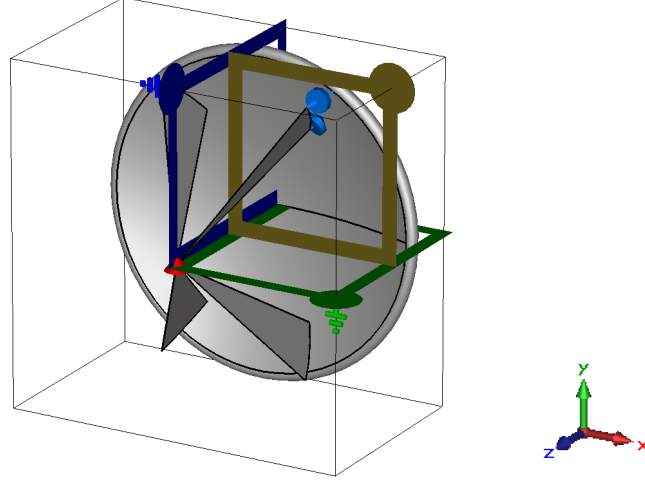
Figure 3.3. Symmetry planes reduce the numerical effort in the simulation. The reflector IRA can be defined with a magnetic symmetry in the E-plane (y-z plane) and an electric symmetry in the H-plane (x-z plane).

- **Port definition.** Power is fed into the simulation domain through a port and is either radiated, absorbed in lossy material, or reflected back out the port. The type of port chosen for these simulations was a lumped element discrete port defined in a gap at the apex of the feed arms. This is represented in the simulation domain by a wire with a lumped element power source and defined characteristic impedance, Z_{port}, and for which appropriate currents and voltages are induced in response to the excitation signal. For the most accurate return loss or S$_{11}$ calculations, the use of a waveguide port is typically recommended. However, in this model the appropriate waveguide is a coaxial cable that is very small relative to the full-size antenna, and to discretize the coaxial cable appropriately would introduce very small mesh steps that directly and negatively impact the simulation time. Additionally, the actual geometry at the feed of a reflector IRA is a rather discontinuous transition from coaxial cable to the conical TEM transmission line that may be well-represented by the wire dis-

crete port model. The discrete port perfectly feeds the balanced transmission line feed arms with no worry of inducing common mode radiation, or undesired coupling between the feed arm and coaxial cable.

3.2.3 Model Construction Considerations.

While a perfect digital representation of the actual reflector IRA may seem ideal, certain trade-offs must be made. Details on the construction of the computational model and the associated trade-offs are described in this subsection.

- **Physical dimensions:** the primary simulation model uses a 12-inch reflector. In constructing a reflector IRA, the paraboloidal reflector is the fixed starting point for the design; a few options have been identified for the AFIT noise radar, including 12- and 18-inch diameter reflectors. The 12-inch reflector designs are chosen as the primary emphasis for simulated experiments. At this smaller size, maximizing the low-frequency performance is the most challenging and represents the best scenario to explore the possibilities of what a reflector IRA can do as a compact low-frequency antenna. In the context of the simulation setup considerations discussed in the previous section, the physical dimensions of a 12-inch reflector IRA are also not so large that the computational expense of performing a full 20 GHz simulation becomes unreasonable. This allows the trade-offs between the time- and frequency-domain performance to be fully explored. Additionally, the frequency range of the AFIT noise radar relative to a 12-inch reflector IRA is almost directly analogous to the desired frequency range and physical size of the NRTF IRAs, so the key results can be scaled appropriately to get an idea of potential performance enhancements for the NRTF antennas without performing a full additional set of simulated experiments. Figure 3.4 shows the physical 12-inch reflector compared to the

currently employed log-periodic antenna of the AFIT noise radar system.
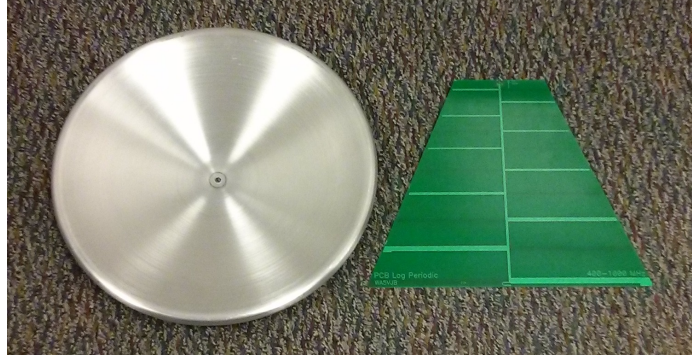
Figure 3.4. 12-inch reflector and current log-periodic antenna of the AFIT noise radar.

- **Material properties:** metal structures are modeled as PEC. This is a standard practice and starting point in many CEM methods. The increased fidelity of including lossy metals with finite conductivities is offset by the computational expense, and for the frequencies at which we are interested in characterizing and improving antenna performance, the effects are assumed to be negligible.

- **Feed arm thickness:** the feed arms are modeled as thin or nearly thin sheets of PEC. For the initial model buildup, we try to replicate the analytical case (infinitely thin sheets) as closely as possible. Use of finite thickness materials is recommended for the TD solver, but the chosen thickness (0.001λ at 20 GHz, about 0.015 mm) is still much smaller than actual materials that will be used for construction. After building confidence in the behavior and the results of the theory-based simulations, applying realistic dimensions is an option.

- **Feed gap geometry:** the feed gap is defined by a truncation of the geometry. The excitation source for the simulation is placed between the upper and lower feed arms, as in a balanced dipole feed. The necessary gap is defined by truncating the ideal geometry instead of translating the arms apart, as shown in Figure 3.5. The idea here is to maintain the radial lines originating

29
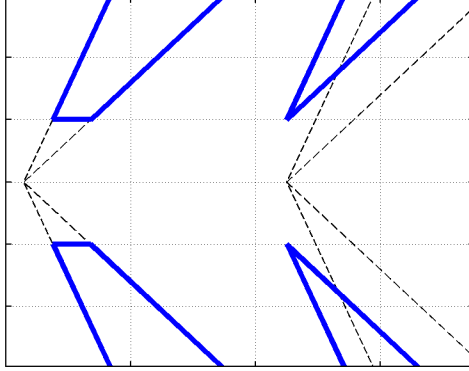
Figure 3.5. The feed gap is defined by a truncation (*left*) of the feed arm geometry, rather than a translation (*right*). A discrete port is defined between the lower and upper arms.

at the focus of the paraboloidal reflector and to avoid generating infinitesimally small dimensions that are unable to be accurately represented in the discretized model. This does result in an increase in the capacitance of the geometry at the feeding port, but it will be shown that this is a realistic phenomenon seen in the realized reflector IRA.

- **Reflector edge treatments:** the paraboloidal reflector is modeled with a rolled edge. All realistic reflectors that may be sourced to construct reflector IRAs for experimentation at AFIT have been treated with rolled edges, instead of an abrupt transition at the edge of the paraboloid. This will modify the edge diffraction characteristics. The computational model is parameterized to include a solid circular cross-section edge that is perfectly tangential to the parabola at the transition, as shown in Figure 3.6. Actual reflectors may not have perfectly circular or solid edges, but this is assumed to be a suitable starting point.

- **Matching circuit:** the matching circuit is composed of multiple resistors and wires with realistic geometry. The geometry and configuration of the resistors in the matching circuit are parameterized for ease of modification in various experiments. For cases where a simulation model is meant to replicate a real

Figure 3.6. Reflector cross-section. The reflector is modeled with a perfectly smooth transition from the parabolic surface to a circular rolled edge.

antenna, the geometry and resistor values are made to match as closely as possible. For the simulation-only experiments, the standard configuration is defined with the following characteristics:

1. Two chains of resistors attaching the feed arm to the dish.
2. Two resistors in each chain with equal resistance.
3. The inner chain follows the β_1 angle of the arm straight to the dish.
4. The outer chain is attached at the rim of the parabolic portion of the reflector.

This geometry was inspired by the design used for the 12-foot reflector IRA built for the NRTF, though in that case the dimensions are large enough to support or require more resistors in two pairs of resistor chains (see Appendix A). The specific geometry described here is shown in Figure 3.7.
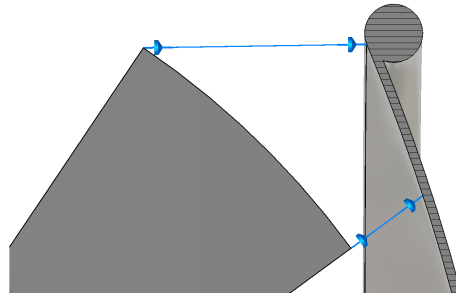
Figure 3.7. Resistor geometry for simulation experiments. PEC wires connect the lumped element resistors to the feed arms and reflector. For simulation models of real antennas, the geometry and resistor configuration is made to match as closely as possible.

3.3 Initial Verification of Model: Feed Structure

Impedance matching and the nondispersive nature of the feed structure on the reflector IRA are key to its UWB capability. It worthwhile, then, to develop a simulation technique for measuring and optimizing the characteristic impedance, Z_{arm} or Z_{feed}, of single or multiple pairs of feed arms. The initial verification of the models and CEM software focuses on assessing the capability of the simulated TDR tool, using the analytical cases for single feed arms and two pairs crossed at 90° as reference points. The "experiments" described in the following sections are performed purely in simulation.

3.3.1   One Pair of Feed Arms.

The first task in the build-up approach to modeling a complete reflector IRA is to model the feed structure supporting the spherical TEM wave. Just as in the analytical build-up described in Chapter II, the starting point is for a single pair of coplanar plates forming the conical transmission line, and for which the analytical solution of Z_{arm} is available [13].

Experiment 1-1: Simulated TDR. Technical documentation for the NRTF reflector IRA specifies the β-angles for the feed arms. These were used to model a single pair of arms for the initial simulation experiments, aligned in the y-z plane of the domain. First, a single simulated TDR response was produced, shown in Figure 3.8. The theoretical characteristic impedance was calculated to be $Z_{arm} = 331.40$ Ω, and is plotted as a blue dashed line. The simulated TDR curve shows the impedance as a function of time. The curve starts at $t = 0$ at the expected (defined in the simulation) value of $Z_{port} = 300$ Ω; an initial capacitive discontinuity in the geometry is observed as a dip in the impedance, then the curve then rapidly approaches the theoretical Z_{arm}. The final "measured" value for Z_{arm} is taken as a mean from t_m to $t_m+0.02$
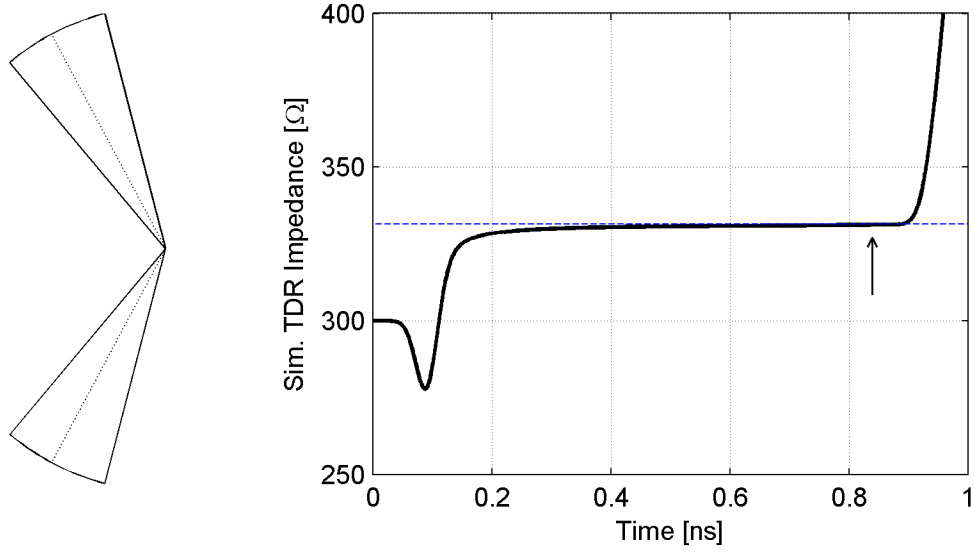
Figure 3.8. Simulated TDR response for the arms shown. Despite the mismatched $Z_{port} = 300\ \Omega$, the curve rapidly approaches to within $0.4\ \Omega$ of the theoretical value, $Z_{arm} = 331.4\ \Omega$, indicated by the blue dashed line. The scalar result for Z_{arm} is taken approximately where indicated by the arrow.

ns where

$$t_m = \frac{2 \times armlength}{c}. \tag{8}$$

For $armlength = 125$ mm as in this model, the result is $t_m = 0.834$ ns, just before the curve shows the pulse reflecting strongly from the end of the arm. The simulated $Z_{arm} = 331.02\ \Omega$, an absolute error of $-0.378\ \Omega$, or -0.11% compared to the theoretical value. This is an encouraging first result. Next we determine if the accuracy is sensitive to simulation parameter changes.

Experiment 1-2: Simulated TDR Stability. One goal for the CEM modeling effort is to use the simulated TDR to assist in designing or optimizing the TEM feed impedance for arbitrary angles and multiple arms; the next step to ensure accurate results in this regard is to modify simulation parameters for a set of arms with static geometry to assess the stability of the extracted value of Z_{arm}. The previous feed arm geometry was simulated with three different values each of mesh resolution, feed gap distance, and port impedance. For this and all subsequent simulated TDR measure-

ments, the value of Z_{arm} is extracted using the methodology presented in the first experiment. The overall consistency in the modeled Z_{arm} results is apparent, shown in Figure 3.9, and the maximum error was that of the first experiment (-0.11%).
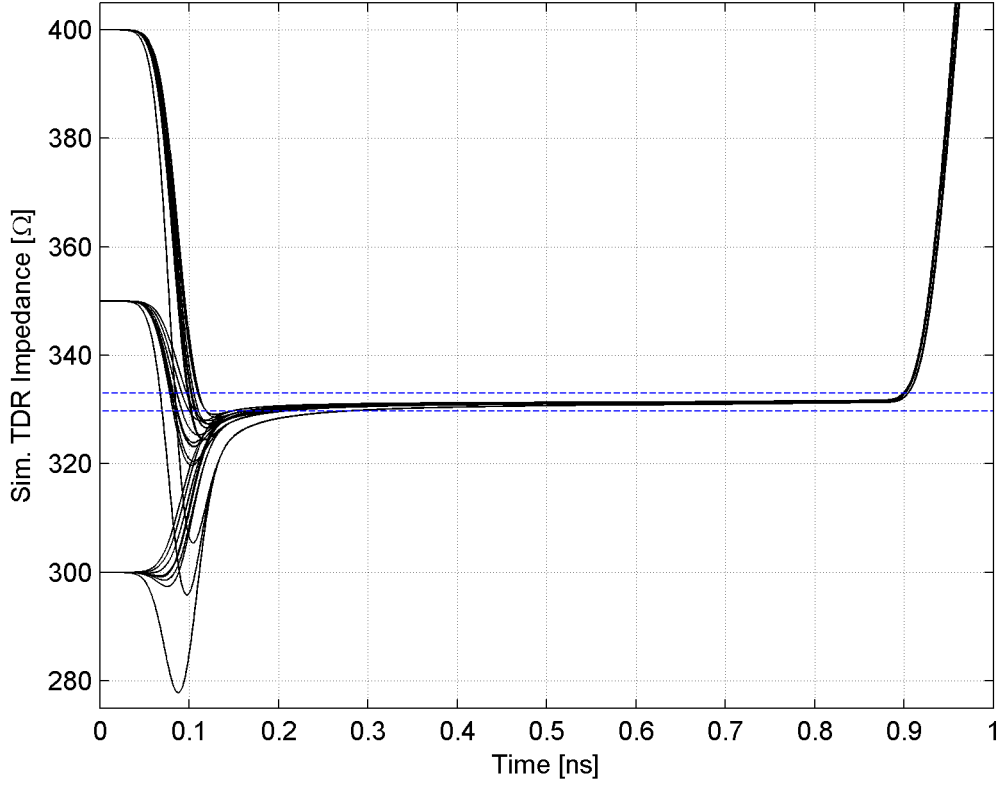
Figure 3.9. A composite TDR of the arms from Experiment 1-1 with mesh resolution, feed gap, and port impedance parameters varied. The extracted value of Z_{arm} is consistently within $0.38\ \Omega$ or 0.11% of the theoretical value. The blue dashed lines indicate $\pm 0.5\%$ error.

Experiment 1-3: Varying the Value of $\mathbf{Z_{arm}}$. Having shown excellent agreement with the analytical solution at a single data point, the next step is to vary the β-angles to achieve different values of Z_{arm}. The simulated TDR measurements are compared to the analytical solutions. The feed arm angles were varied at $10°$ increments for β_1 from $35°$ to $85°$, and $5°$ increments for β_2 from $(\beta_1 + 5)°$ to $110°$ for a 60-point data set. Two example arms of the extreme cases from the data set are shown in Figure 3.10, and the extracted results of the data set are plotted in Figure 3.11.

34
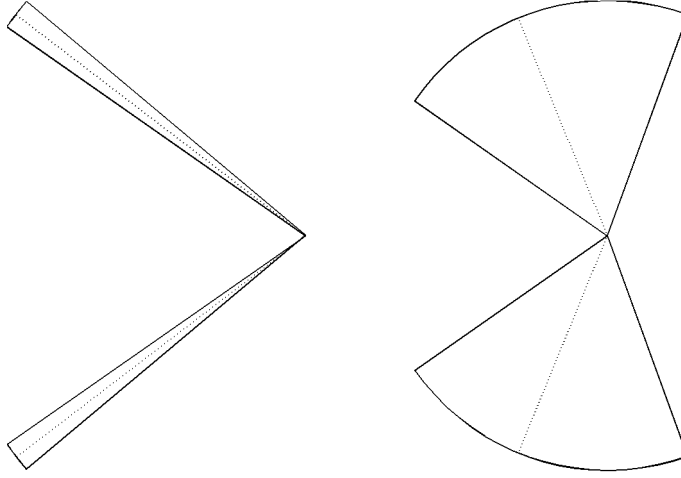
Figure 3.10. Two of the extreme cases of the feed arms simulated in Experiment 1-3. Left: $\beta_1 = 35°$, $\beta_2 = 40°$, $Z_{arm} = 482.2$ Ω. **Right:** $\beta_1 = 35°$, $\beta_2 = 110°$, $Z_{arm} = 205.2$ Ω.

The simulated TDR measurements agree very closely with the analytical solution in all cases. A closer look at the errors in the data set, shown in Figure 3.12, indicates that the very narrow arms associated with high b_1/a values are modeled with less accuracy. This larger jump in error can likely be attributed to an inability to accurately discretize the geometry near the feed, based on the chosen mesh settings; CST warning messages indicated that some mesh cells were completely filled with PEC as a result of the fine geometry features at the feed. Despite this, measurements are still within 0.5%. This is assumed to be accurate enough for our purposes.

Experiment 1-4: Adding a Third Dimension. Up to this point, the arms have been defined only in a single plane of the simulation domain at $\phi = 90°$, but the actual reflector IRA will have arms at various ϕ_0-angles. It is prudent to document the effects of a Cartesian hexahedral grid discretization on the modeled feed structure defined by 3D spherical angles. For this experiment, two sets of arms with different β-angles but both corresponding to $b_1/a = 0.8671$ or $Z_{arm} = 400$ Ω were generated, as shown in Figure 3.13. These were rotated through ϕ from 45° to 90° at a 3° increment.
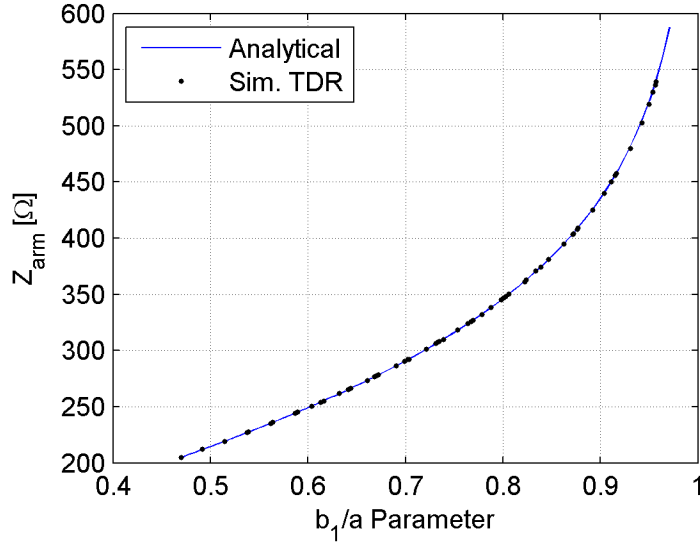
Figure 3.11. Simulated TDR values of Z_{arm} for a wide variety of β-angles (Experiment 1-3). The b_1/a parameter associated with each set of angles is used to provide a consistent reference.
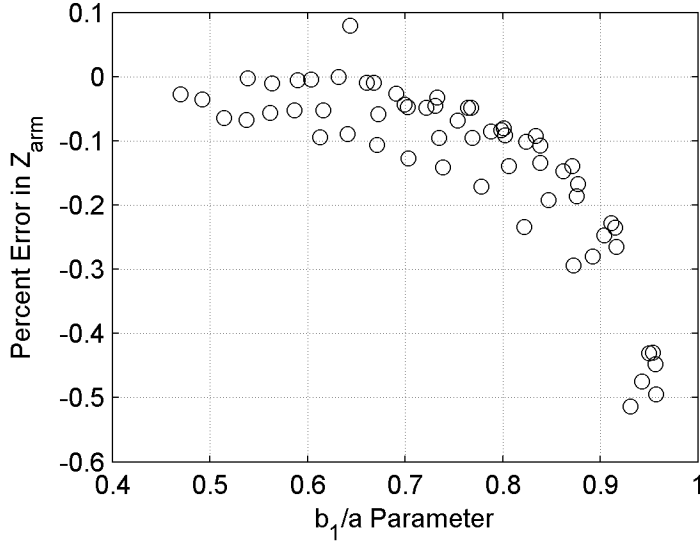
Figure 3.12. Error in simulated TDR values of Z_{arm} for a wide variety of β-angles (Experiment 1-3) indicates very strong agreement between the theoretical values and the simulation.
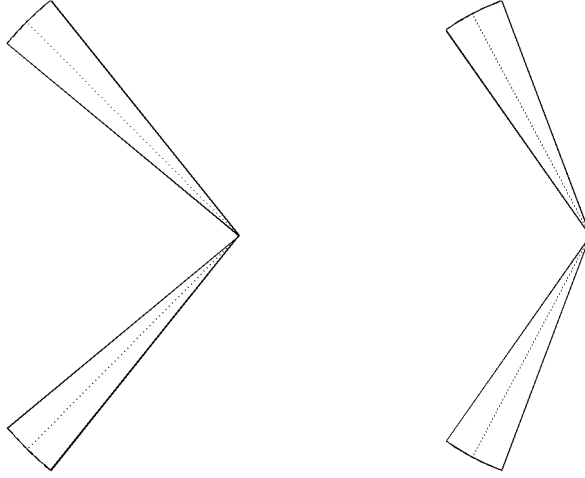
Figure 3.13. The arms from Experiment 1-4, modeled at various ϕ-angles. Left: $\beta_1 = 39.73°$, $\beta_2 = 51.33°$, $Z_{arm} = 400$ Ω. Right: $\beta_1 = 54.97°$, $\beta_2 = 69.36°$, $Z_{arm} = 400$ Ω.

The error in the simulated TDR measurements, shown in Figure 3.14, continues to indicate a high degree of agreement between the theoretical value and the simulated measurement. Interestingly, the magnitude of the error is least for the intermediate ϕ angles, and greatest at the "nice" angles of $\phi = 90°$ and $\phi = 45°$, though still within 0.2% of the theoretical values. Additionally, there is also a slight variance in the simulated measurements associated with the different β-angles of the arms, as both arms should have measured identically. This discrepancy is not enough to warrant further investigation.

3.3.2 Two Pairs of Feed Arms.

Having demonstrated a very high degree of agreement between the theoretical and simulated TDR values of Z_{arm}, the next task is to measure Z_{feed} with the simulated TDR for feed structures composed of multiple pairs of arms. We start with the standard reflector IRA configurations having two pairs of arms.

Experiment 2-1: Feed arms crossed at 90°. The analytical solution for

37
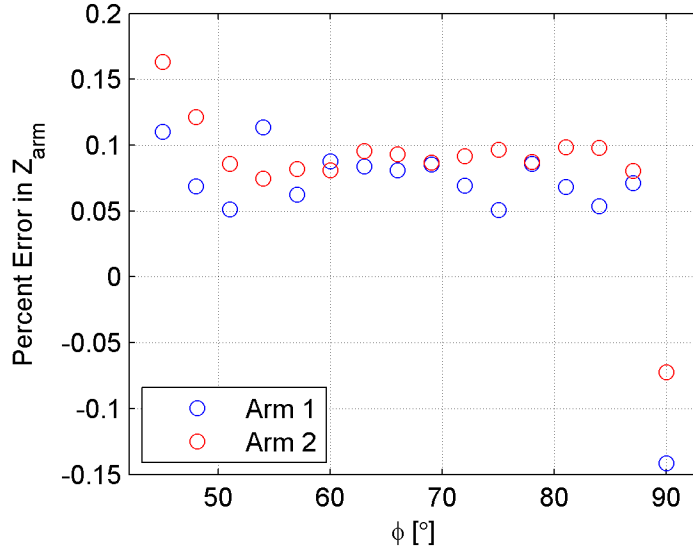
Figure 3.14. Low error in simulated TDR values of Z_{arm} for a variety of ϕ-angles indicates very strong agreement between the theoretical values and the simulation.

two pairs of feed arms crossed at 90°, or equivalently for $\phi_0 = 45°$, indicates that $Z_{feed} = Z_{arm}/2$. The original reflector IRA designs, therefore, used two pairs of arms with $Z_{arm} = 400\ \Omega$ to achieve a feed impedance of $Z_{feed} = 200\ \Omega$. This relationship was verified in simulation for sixteen sets of arms of varying β-angles for $Z_{arm} = \{300, 350, 400, 450\}$. The error in the simulated measurement ranged from 0.009% to 0.115%, with a mean error of 0.079%.

Experiment 2-2: Feed arms for $\phi_0 = 60°$. The current standard reflector IRA design has $Z_{feed} = 200\ \Omega$ composed of feed arms with $\phi_0 = 60°$. This change from the initial designs with $\phi_0 = 45°$ is driven by the results of theory and optimization experiments to increase the uniformity of the field distribution on the aperture [21]. A consequence of straying from the $\phi_0 = 45°$ design is that analytical solutions no longer exist for the relationship between Z_{feed} and Z_{arm}, so the design parameters must be determined numerically or experimentally. The NRTF antenna was designed for $Z_{feed} = 200$ at $\phi_0 = 60°$, so this feed structure is modeled using the parameters specified in the technical documentation, and a simulated TDR measurement will

38

determine if it results in $Z_{feed} = 200$ Ω. Surprisingly, it does not. Simulated TDR measurement puts the value of $Z_{feed} = 197.67$ Ω. This is close, but at an error of -1.17%, it is an order of magnitude worse than what has been demonstrated in CST thus far. Now, the opportunity to test the envisaged experimental process is presented. An optimization routine was performed in CST to find $Z_{feed} = 200$ Ω while varying only β_2; the resulting β-angles were input into the MATLAB script to reverse-solve for the correct Z_{arm} and then the script run again to design a set of arms with that Z_{arm} and β_0 appropriate for the NRTF reflector. The results of the experiment are shown in Figure 3.15 and in Table 3.1.
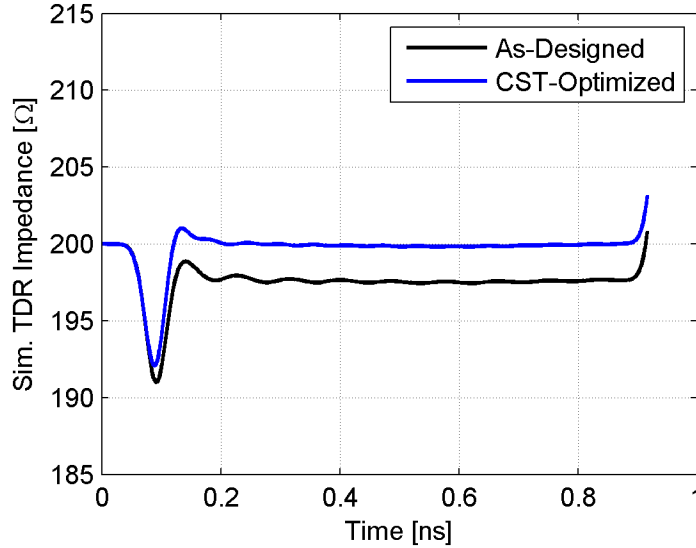
Figure 3.15. Simulated TDR of the as-designed and the CST-optimized feed arms for the NRTF reflector IRA. The design goal was for $Z_{feed} = 200$ Ω.

3.4   Calculation of Antenna Performance Metrics

The initial verification experiments suggest that the computational models of the reflector IRA feed structure behave as predicted by the theory. Now, full antenna models are developed and analyzed. Details of the sourcing for the antenna performance metrics are discussed in this section.

Table 3.1. Comparison of as-designed and optimized arms for $\phi_0 = 60°$ and $Z_{feed} = 200$ Ω specific to the NRTF reflector IRAs.

	Design	CST-Optimized
β_0	61.9275°	61.9275°
β_1	49.9334°	50.3486°
β_2	75.4221°	74.8992°
$\beta_2 - \beta_1$	25.4887°	24.5506°
Z_{arm}	331.4 Ω	335.9 Ω
b_1/a	0.7760	0.7834

3.4.1 Results Provided Directly from the Software.

As CST is a full-featured CEM tool that is regularly used to design antennas, many of the desired performance metrics are available directly from within the software. This comes with a caveat, of course; CST will always calculate and present results regardless of the simulation setup and user inputs. The onus is on the user to do due diligence in ensuring that the results are reasonably accurate. Given the detailed consideration of the simulation setup discussed previously, and the high-quality results of the initial simulation experiments, it is assumed that the automatically calculated results from CST can be trusted. If the accuracy of the results may be in question due to specific setup choices made for individual simulations, those will be discussed as necessary. In general, the following results are extracted from simulation without additional data processing and may be presented as such in Chapter IV:

- Ingoing and outgoing port signals
- S_{11} parameter
- TDR signals
- voltage standing wave ratio (VSWR)
- Complex input impedance, $\widetilde{Z}_{in}$
- Power quantities: accepted power, stimulated power, reflected power, radiated power, and power loss in lumped elements

- Efficiencies: radiation efficiency and total efficiency

- Field probe signals

- Farfield quantities: gain, realized gain, directivity

3.4.2 Results Requiring Additional Data Processing.

Some of the desired results are not calculated automatically, but can be extracted within CST using the built-in Template-Based Post-Processing tool. Some of these are composite results calculated with multiple built-in results. For example:

- **Front-to-back ratio.** The absolute value gain (in dB) of the antenna in the direction opposite boresight is subtracted from the boresight gain.

- **Sidelobe levels.** The antenna gain pattern cuts are analyzed for the value of the first sidelobe relative to the boresight gain.

- **Beamwidth.** The antenna gain pattern cuts are analyzed to determine the angular extent of the main beam for a -3 dB beamwidth.

- **Cross-Polarization performance.** This result is a unique setup specific to the work presented here. Because the simulated antennas have perfect symmetry, there is identically zero cross-polarized radiation on boresight. In reality, imperfections and asymmetries introduced in construction will fill in the nulls in the antenna patterns and introduce additional cross-polarized components in the radiated fields. Additionally, alignment errors can never be perfectly eliminated in practice, and cross-polarized radiation *is* observed. While there may be zero cross-pol exactly on boresight, the computational model does show some cross-polarization near boresight. The method used here to estimate the cross-pol performance is to search the $\pm 20°$ solid angle centered on the main beam for the maximum cross-polarized component and compare it to the maximum co-polarized component at each frequency. The results seem to agree in general with the trends shown in published data of actual measurements [9].

Other results exist within CST but means of displaying the data in a compact fashion are lacking. For example, the antenna pattern cuts as a function of frequency. This is a 3D data set for any particular pattern cut, where the gain is a function of frequency and observation angle. To present appropriate 3D plots, a combination of CST macros

41

and MATLAB routines were used to extract the data and compile it for processing and plotting.

3.4.3   Time Domain Data Processing and Verification.

Finally, the key results that require a significant data processing effort are the time-domain metrics. The remainder of this section is dedicated to explaining the specific methods used to generate the metrics from the output of CST simulations. To aid in verification of the data processing method, the commercially available IRA-3Q shown in Chapter I is simulated and the extracted results are compared to published data [1]. The CEM model of the IRA-3Q, created from available specifications and best judgment from photographs, is shown in Figure 3.16.
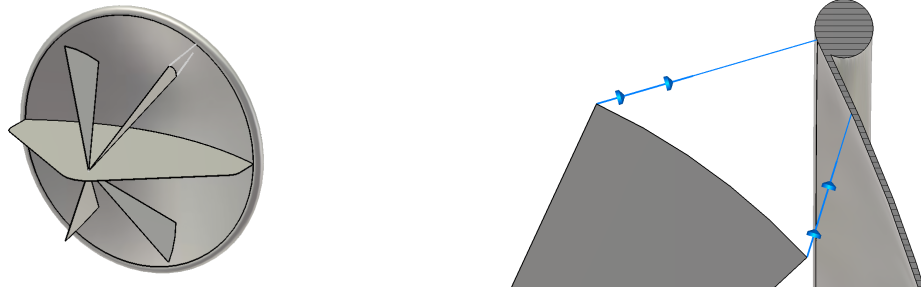
Figure 3.16. The IRA-3Q was simulated and the computed time domain results are compared to published data [1] for verification of the data processing technique.

Recalling the results of Farr's work [11], the goal is to determine the impulse response waveform, $h(t)$, which can be used to fully characterize the antenna performance. In the general formulation given by Farr, $h(t)$ is related to the time-dependent excitation signal and radiated E-field by convolution, as in

$$\frac{E_{rad}(t)}{\sqrt{Z_{o2}}} = \frac{1}{2\pi\nu r}h(t) * \frac{dV_{src}(t')/dt}{\sqrt{Z_{o1}}}, \quad t' = t - r/\nu. \tag{9}$$

Translating the quantities from this general formulation to the scenario of the simulation yields the convention used here (Table 3.2).

Table 3.2. Data sourcing for the impulse response calculation.

General	Specific	Source	Nominal Value
$E_{rad}(t)$	$E_{rad}(t)$	Simulated farfield probe	—
$V_{src}(t)$	$V_{src}(t)$	Simulation excitation	—
r	r	Simulated farfield probe range	5 m
Z_{o1}	Z_{port}	Simulation port impedance	200 Ω
Z_{o2}	Z_0 or η_0	Physical constant	376.7303 Ω
ν	c	Physical constant	299792458 m/s

A deconvolution procedure is required to obtain $h(t)$. Deconvolution is best performed in the frequency domain where algebraic manipulations can be employed. Therefore, the basic steps to extracting $h(t)$ are as follows:

1. Generate time signals in CST.

2. Transform time signals into frequency domain.

3. Solve for frequency domain transfer functions.

4. Inverse transform back to time domain for impulse response.

As with many things that appear simple at first, there are a significant number of details to consider for each step in the process. This is not intended to be an exhaustive primer on digital signal processing. There are infinite ways to accomplish the task using various windows, filters, upsampling and downsampling, truncating and zero-padding of signals. The intent is to describe the process used here that was determined to give reasonable and repeatable results. As a final prefatory note, it may be possible to start the process using the complex frequency-domain representation of the time signals provided by CST and essentially begin at step three, but for lack of signal processing experience and to aid in bookkeeping, the preference here is to begin and end with real time signals.

1. Generating Time Signals. Creating and extracting time signals comes easily with use of the TD solver in CST, especially for signals inside the computational domain. The $V_{src}(t)$ signal can either be extracted from the ingoing port signal or from

the excitation reference signal, both of which are expressed in CST as $V_{src}(t)/\sqrt{Z_{port}}$. The other time signal needed is the radiated transient E-field in a farfield condition, $E_{rad}(t)$. CST will calculate this automatically for a farfield probe defined in the desired observation location and for the polarization(s) of interest. The range at which the probe is defined can be arbitrary, as range effects will be factored out during data processing. In the data presented here, the range was typically set to 5 meters. Now, there is a question regarding the fidelity of the supplied time signal. The farfield condition is not met within the computational domain, so we rely on CST's near-field to far-field transformations to provide the probe signals. This means that we are starting with a signal that is the result of various transforms, has been subject to filtering or windowing, and there will be some artifacts of that process in the data. Increasing the accuracy settings of the simulation helps ensure that the initial time signals used in the transformation have decayed sufficiently to avoid large truncation errors. The default critera for ending the simulation is when the energy in the domain has decayed to -30 dB relative to the peak value during the simulation. A CST tutorial suggests that a setting of -40 dB is high accuracy, and -50 dB very high; the setting chosen for these simulations was -60 dB. This is only a feasible option because the reflector IRA efficiently radiates and absorbs most of the power right away with minimal resonance.

2. Time- to Frequency-Domain Transformation. Before performing the domain transformation on $V_{src}(t)$ and $E_{rad}(t)$, some initial processing is required to ensure that the discrete time steps for each signal are equal. The Δt of the farfield probe signal provided by CST is much coarser than the excitation signal, but of sufficient resolution to get the necessary detail from the final impulse response, $h(t)$. After investigating the various effects and consequences of oversampling the probe signal to match the excitation, oversampling both signals, or undersampling the

excitation to match the probe, the latter was chosen. The excitation signal provided by CST begins with a very small timestep, and the amount of information lost by undersampling is negligible (see Figure 3.17). The adjusted timestep is nominally $\Delta t = 5$ ps; this gives a frequency domain bandwidth of $\frac{1}{\Delta t} = \frac{1}{5 \text{ ps}} = 200$ GHz, which more than satisfies the Nyquist criterion for the 20-30 GHz in the simulation domain. The time domain signals are also zero-padded to ensure a sufficiently useful step width in the frequency domain. Because the transient signals start and end near zero and were allowed to decay sufficiently, this operation is very well-behaved. The actual transformation is accomplished through use of the MATLAB Fast Fourier Transform (FFT) function. A graphical depiction of the process to this point can be observed in Figures 3.17 and 3.18.

3. Solving for Transfer Functions. Having generated the appropriately scaled frequency domain signals $\widetilde{E}_{rad}$ and $\widetilde{V}_{src}$, the next task is to solve for the transfer function, $\widetilde{h}$. While the relationship between the transmit and receive transfer functions was made clear [11],

$$\widetilde{F} = \frac{s\,\widetilde{h}}{2\,\pi\,c} = \frac{j\,\widetilde{h}}{\lambda}, \tag{10}$$

and it is certainly possible to solve for $\widetilde{h}$ in one step, the decision was made to first solve for $\widetilde{F}$ to ensure the system was well-behaved. As this is an inverse problem, proper care must be taken to avoid exaggerated behavior in regions of low signal-to-noise. Rearranging the relationship in the general formulation [11],

$$\frac{\widetilde{E}_{rad}}{\sqrt{Z_{o2}}} = \frac{e^{-\gamma r}}{r}\,\widetilde{F}\,\frac{\widetilde{V}_{src}}{\sqrt{Z_{o1}}}, \tag{11}$$

45
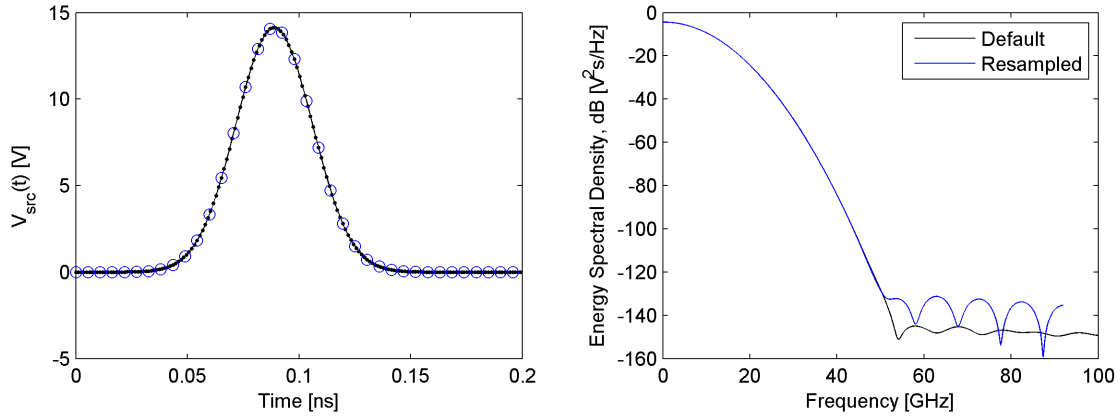
Figure 3.17. Time- and frequency-domain representations of the excitation voltage. In undersampling the excitation to match the probe signal, the frequency-domain bandwidth is reduced and the noise floor increased. These effects are sufficiently removed from the 0-20 GHz region of primary interest.
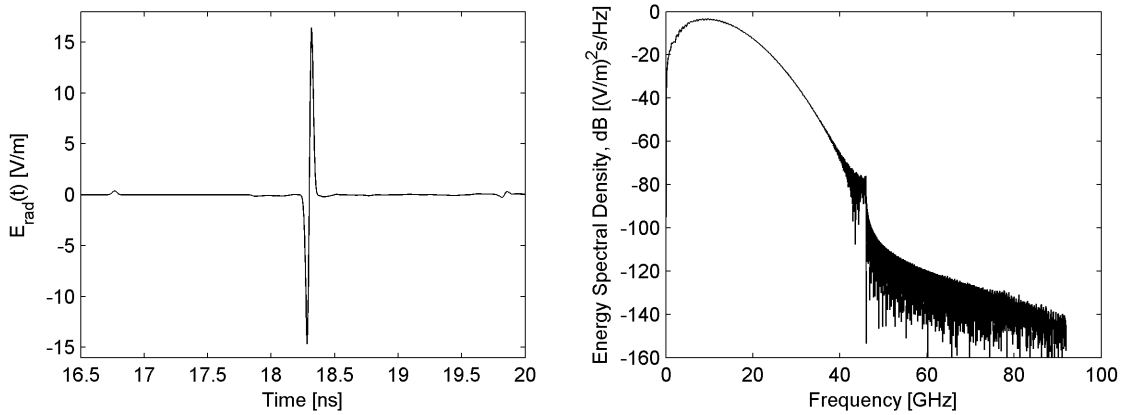
Figure 3.18. Time- and frequency-domain representations of the radiated field. Evidence of low signal-to-noise ratio and a previous windowing operation from the original near- to far-field transformation are evident in the higher frequencies. These effects are outside the 0-20 GHz region of interest, and will be suppressed in data processing.

and applying the specific variables of this problem leads to the following formulation:

$$\widetilde{F} = r \cdot e^{\ j2\pi fr/c} \ \sqrt{\frac{Z_{port}}{Z_0}} \ \frac{\widetilde{E}_{rad}}{\widetilde{V}_{src}}. \tag{12}$$

Various techniques were explored to perform the deconvolution and maintain stability in regions of low signal-to-noise, including a Wiener-deconvolution of the form [20]

$$\widetilde{F} = r \cdot e^{\ j2\pi fr/c} \ \sqrt{\frac{Z_{port}}{Z_0}} \ \frac{\widetilde{E}_{rad}\ \widetilde{V}_{src}^*}{|\widetilde{V}_{src}|^2 + \lambda_{noise}} \ , \tag{13}$$

where λ_{noise} is a maximum value of the energy spectral density in $\widetilde{V}_{src}$ outside the signal portion of the energy. Considering the noise to be anywhere outside the 99.9% energy window gave a nice amplitude taper and approximate -3 dB cutoff around 20 GHz, which was a good result. Unfortunately the method also decreases the amplitude of the transfer function within the passband. Another option was to apply a low pass filter of the form [13]

$$G(f) = \frac{1}{1 + (f/f_0)^{2N}} \ , \tag{14}$$

where f_0 is the cutoff frequency and N is an integer greater than one. Farr uses this filter in his work, and refers to it as a "modified Butterworth" filter. Choosing $f_0 = 20$ GHz and $N=6$ gave the desired results, and the effects on the deconvolution can be seen in Figure 3.19. Having solved for $\widetilde{F}$, getting $\widetilde{h}$ is a simple matter of rearranging Equation (10) for the result

$$\widetilde{h} = \widetilde{F}\frac{\lambda}{j}. \tag{15}$$

At this point we can also begin to compare some results of the test case of the simulated IRA-3Q with published measurements [1]. The $|\widetilde{h}|$ extracted from simula-

47
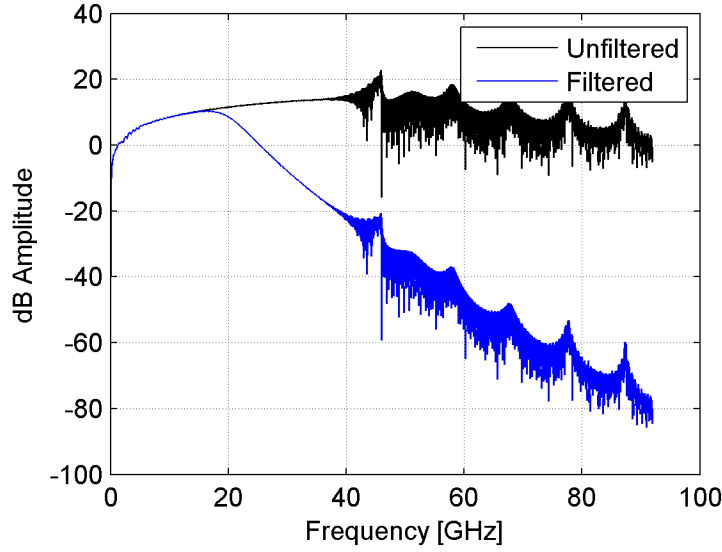
Figure 3.19. The magnitude of the transmit transfer function, $|\widetilde{F}|$, shown with and without filter applied.. The modified Butterworth filter, Equation (14), is configured with $f_0 = 20$ **GHz and** $N = 6$.

tion is overlaid on the published data in Figure 3.20. The most noticeable differences are at the higher frequencies, above approximately 5 GHz. This disparity is not likely attributable to the data processing employed, as Farr has stated a preference for the same filter and same cutoff frequency of 20 GHz [13]. The original intent for the comparison was simply to ensure that the simulated results are the correct order of magnitude, and the close agreement over most of the spectrum indicates that this is the case. The differences in high-frequency content, however, have a significant effect on the shape of the $h(t)$ waveform, as will be seen shortly.

4. Inverse Transformation. Having taken all the correct steps to this point, $h(t)$ is now obtained simply by applying the inverse transformation to $\widetilde{h}$. This is accomplished using the Inverse Fast Fourier Transform (IFFT) function in MATLAB. Finally, Parseval's theorem must be taken into account, to ensure that the energy in each domain is equal. In this case the appropriate normalization is to divide $h(t)$ by the discrete time step, Δt, associated with the data.

The final result of the data processing effort is now compared to the published data
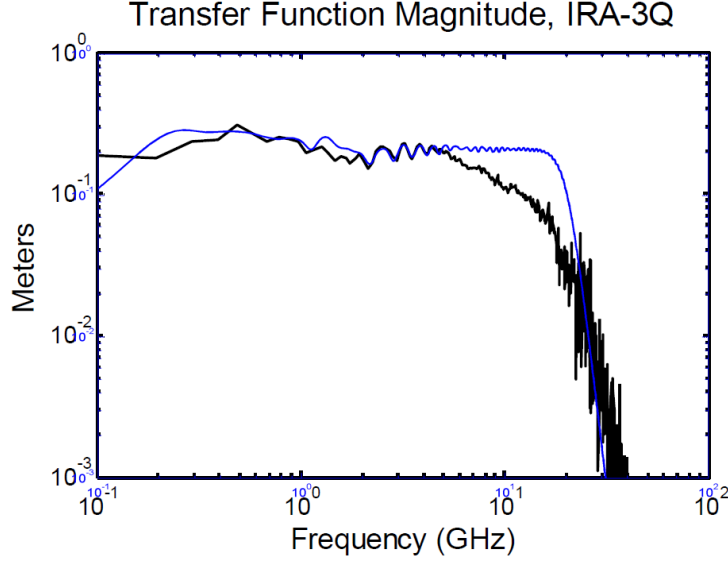
**Figure 3.20. A comparison of $|\widetilde{h}|$ for simulated and published data for the IRA-3Q [1].
The simulated data in blue is overlaid on the published plot in black.**

once again. The simulated $h(t)$ is plotted and overlaid on the measured $h(t)$ for the

IRA-3Q antenna in Figure 3.21 and Figure 3.22. The simulated result was translated

on the time axis to align with the published data, but was otherwise unchanged. The

pre- and post-impulse portions of the waveform show the correct general amplitudes.

The width of the pulse is correct. What is now made clear is that the peak value of

the waveform is highly influenced by the maximum frequency content in the signal, a

result of the nondispersive feed and resulting constant phase front on boresight for all

frequencies. Using the comparison as a check that the results are the correct order of

magnitude, the conclusion is that the data processing and normalization procedure are

suitable, and may be used to compare the time domain performance of the various

simulated antennas and configurations that follow. Still, the "close-but-not-quite"

nature of the comparison for $|\widetilde{h}|$ and $h(t)$ prompted a slightly deeper investigation

into the possible sources for the disparity, which can be reviewed in Appendix C.
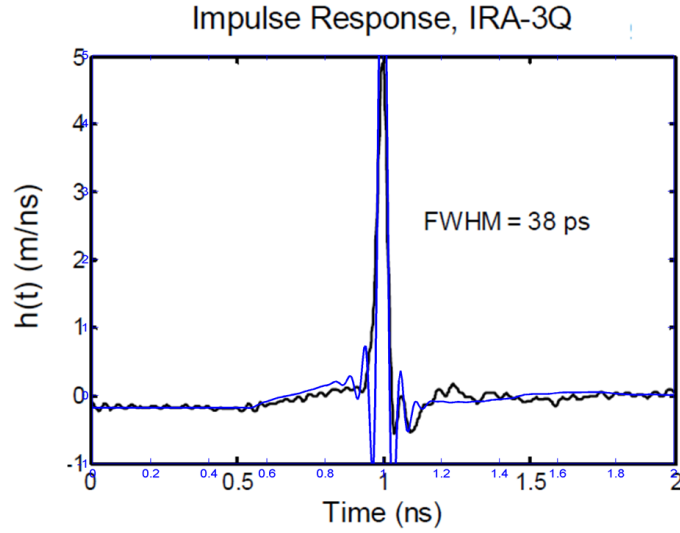
Figure 3.21. A comparison of $h(t)$ for simulated and published data for the IRA-3Q [1]. The simulation data plot in blue is overlaid on the published plot.
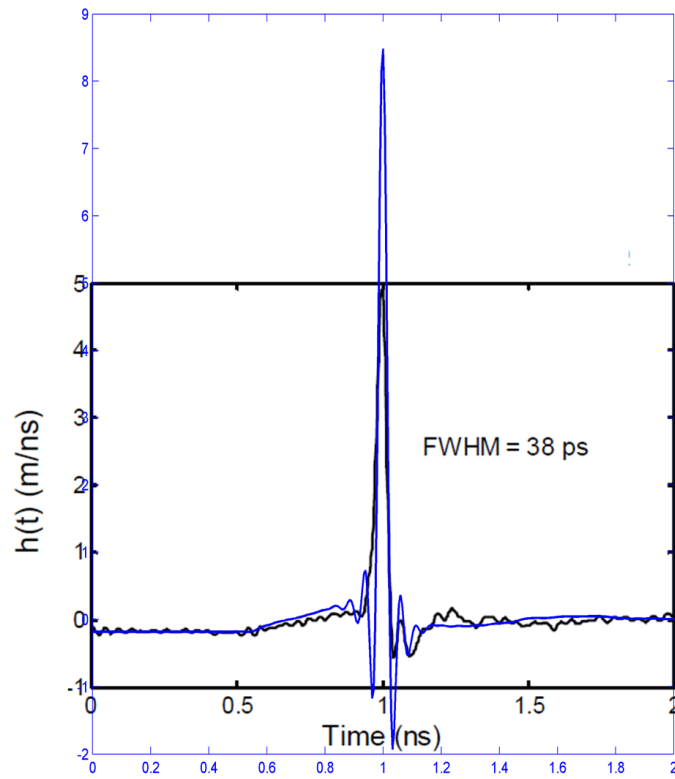
Figure 3.22. A comparison of $h(t)$ for simulated and published data for the IRA-3Q [1] with extended vertical axis. The simulated data has peak amplitude more than 3 m/ns greater than the measured data due to the greater high-frequency content which can be seen in Figure 3.20.

3.5 Overall Simulation Experimentation Strategy

Now that the simulation and data processing methodology has been explained in detail, and shown through various examples to be a valid approach, the overall experiment can be described. As mentioned previously, the primary experimental simulation model IRA is built on the 12-inch paraboloidal reflector. First, the performance of the standard designs using two pairs of arms at $\phi_0 = 45°$ and $\phi_0 = 60°$ is analyzed in both the time and frequency domains. To explore options for low-frequency performance improvements, the simulated TDR analysis is used to assist in designing novel feed configurations that have a good impedance matching characteristics. Parametric sweeps and optimizations are then performed at a lower computational cost using the FD solver at a reduced set of frequencies. Configurations with interesting results are re-simulated using the full bandwidth in the TD solver, so the effects on the time domain performance of the antenna can be assessed.

3.6 Chapter Summary

In this chapter, detailed considerations for the experimental methodology were described. The choice of CEM software, which solver module to use, and specific setup details for the primary simulation models were all thoroughly discussed. The validity of the simulated TDR analysis tool for measuring the characteristic impedance of the transmission line feed for the reflector IRA was demonstrated and the data processing techniques for extracting the time domain impulse response, $h(t)$, were also shown to be suitable. The results and analysis of the simulation experiments on full reflector IRA models are presented in Chapter IV.

IV. Results

4.1 Chapter Overview

With the framework developed and discussed in Chapter III, the foundation is set for analysis of various reflector IRA configurations. First, standard designs are constructed in simulation on the 12-inch paraboloidal reflector and analyzed for their general time- and frequency-domain characteristics. Various ideas to enhance the reflector IRA performance for low UHF operation are explored in simulation and the results are presented and analyzed.

4.2 Analysis of Standard Reflector IRAs

A path similar to the historical development of the reflector IRA was followed for the initial simulated performance characterization. The original design for two arms with $\phi_0 = 45°$ and the latest standard of two arms with $\phi_0 = 60°$, shown in Figure 4.1, were simulated and analyzed. The results serve as a performance baseline for modification experiments.
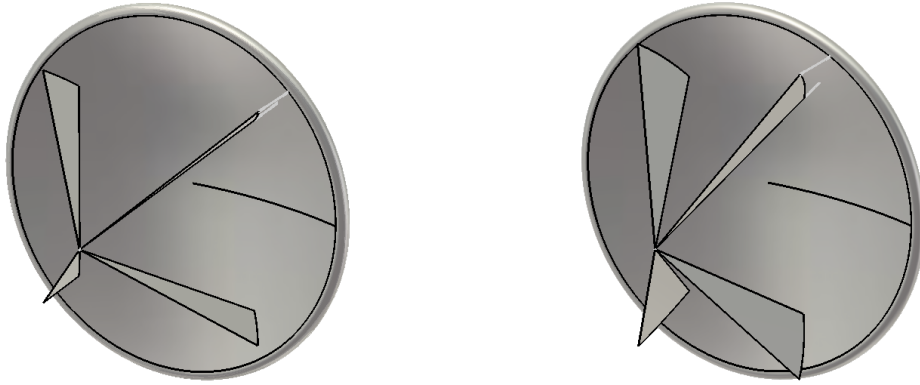
Figure 4.1. Computational models of the standard reflector IRA designs used in the initial characterization study. Left: $\phi_0 = 45°$**, Right:** $\phi_0 = 60°$**. The geometry for both is designed to achieve** $Z_{feed} = 200$ **Ω.**

4.2.1 Time Domain Performance.

Because the reflector IRA was designed with time-domain performance in mind, these results are analyzed first. The impulse response, $h(t)$, and the magnitude of the transfer function, $|\widetilde{h}|$, are shown in Figure 4.2 and Figure 4.3. The key metrics are listed in Table 4.1. These results are for the primary polarization on antenna boresight. Due to the varying methods of time-domain characterization, values derived both from the impulse response and its analytic envelope are presented.

Table 4.1. Time domain metrics of the standard IRA designs.

		$\phi_0 = 45°$	$\phi_0 = 60°$
Peak $h(t)$	[m/ns]	4.81	5.47
Peak $|h^+(t)|$	[m/ns]	4.83	5.49
FWHM $h(t)$	[ps]	29.6	29.1
FWHM $|h^+(t)|$	[ps]	58.0	57.1
Ringing, $\tau_{r,0.22}$	[ps]	39.8	39.3
Ringing, $\tau_{r,0.10}$	[ps]	85.5	83.6

The key take-away from this performance comparison is that the trend in the simulation results agrees with the theoretical and measured results; that is, the $\phi_0 = 60°$ IRA has increased performance across the entire bandwidth, resulting in a higher peak impulse response. One interesting thing to note is the different nature of the late-time response, seen at approximately 2.7 ns on the left side of Figure 4.2. The magnitude was too small to be considered in either the 22% or 10% ringing calculations, but it may be indicative of a lower-frequency resonance in the $\phi_0 = 60°$ IRA. Additionally, the simulated TDR response (Figure 4.4) shows a markedly different result. Note that the TDR response of actual measurements would be reduced by a factor of four compared to this plot. This is due to the splitter balun in the cabling, necessary to impedance match a 50 Ω source and cable system to a 200 Ω feed structure. The large dip at the end of the feed arms of the $\phi_0 = 60°$ IRA is typical in published measurements [1, 9]. The late-time response shown by the lossless simulated TDR
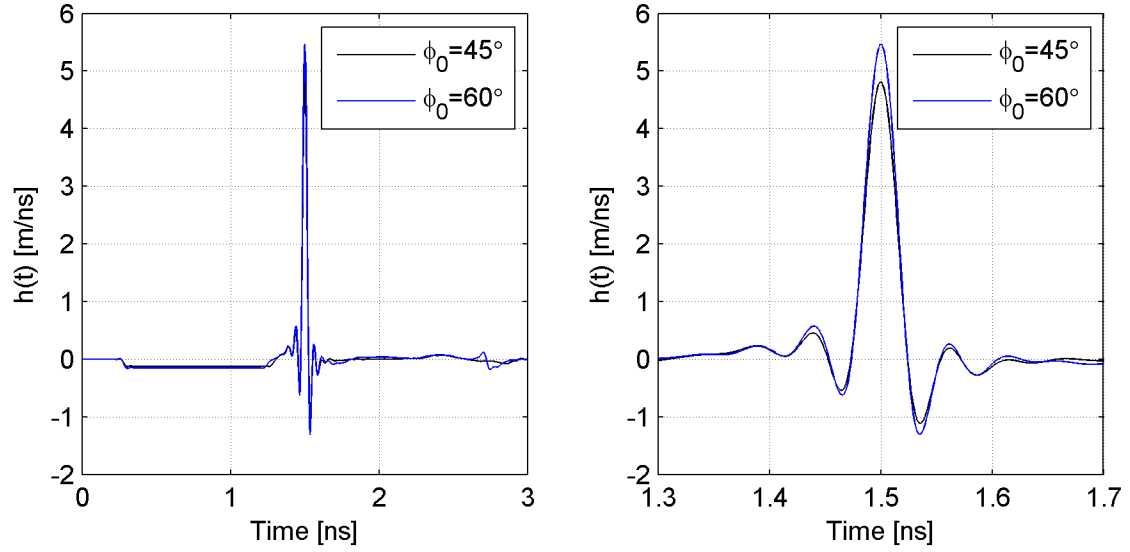
Figure 4.2. Impulse response, $h(t)$, of the standard IRA designs. A closer look at the impulse-like portion of the waveform is shown on the right.
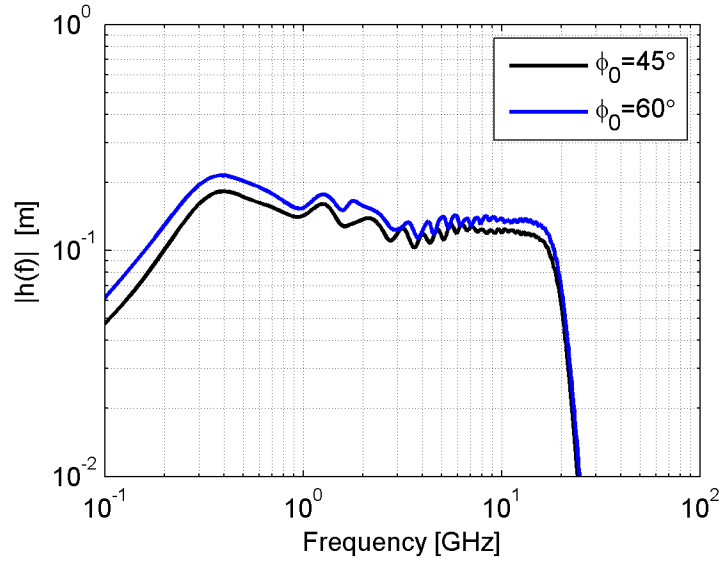
Figure 4.3. Transfer function magnitude, $|\widetilde{h}|$, of the standard IRA designs.

also indicates that the total resistance is matched to the characteristic impedance of the feed, Z_{feed}.
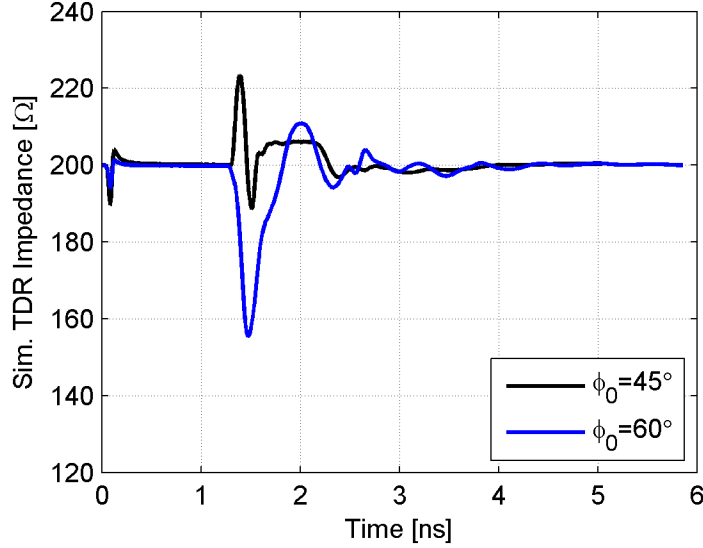
Figure 4.4. Simulated TDR response of the standard IRA designs. The discontinuity at the feed point is at $t \approx 0$ ns and the end of the feed arms is seen at $t \approx 1.3$ ns. The large dip observed on the $\phi_0 = 60°$ IRA response is typical in published measurements. The late-time behavior indicates a total resistance matched to the feed impedance.

4.2.2 Frequency Domain Performance.

Now we look to characterize the standard reflector IRA designs in terms of the frequency domain performance. Should a reflector IRA be considered a candidate antenna for a multi-role communication or radar system, these characteristics would be of greater interest.

First, the S_{11} and VSWR measurements of Figure 4.5 indicate a very high degree of accepted power (very low reflections) across the entire band. This is a necessary condition for good radiation performance, but it is important to note that low reflections alone do not indicate good radiation performance. A primary indicator of radiation performance is the gain of the antenna. Gain on boresight is shown in Figure 4.6.

Just as indicated in the time domain metrics, the performance of the $\phi_0 = 60°$
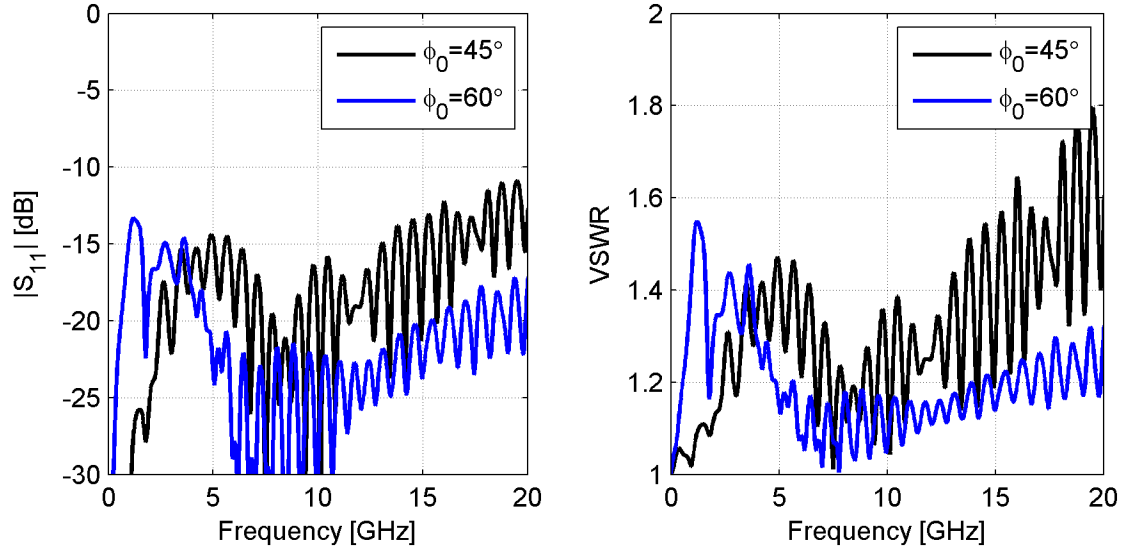
Figure 4.5. $|S_{11}|$ **and VSWR of the standard IRA designs.**

IRA is generally improved across the entire frequency band. Recall that the cross-polarization shown in the plot is an estimate of what may be observed in actual measurements; it shows the maximum cross-polarized component in the $\pm 20°$ solid angle centered on boresight. This estimate indicates a modest 1-2 dB improvement in cross-pol rejection at the higher frequencies for the $\phi_0 = 60°$ IRA. The boresight gain of the antenna decreases rapidly with decreasing frequency, but another look at the S_{11} plot shows very low reflections at the lowest frequencies. Power is accepted into the antenna, but appears that it is not radiated on boresight. We look next at the gain in directions other than boresight, to see if the power is radiated elsewhere.

Figure 4.7 and Figure 4.8 show the gain patterns of the standard reflector IRA configurations as a function of angle and frequency. The E-plane is the plane containing the E-field vector and the direction of propagation; in this case, the y-z plane or a vertical cut through the antenna. The H-plane contains the H-field vector and the direction of propagation; in this case, the x-z plane or a horizontal cut through the antenna. An initial observation is that the $\phi_0 = 60°$ IRA has fewer close-in sidelobes than the $\phi_0 = 45°$ IRA. While it is difficult to ascertain from these images,
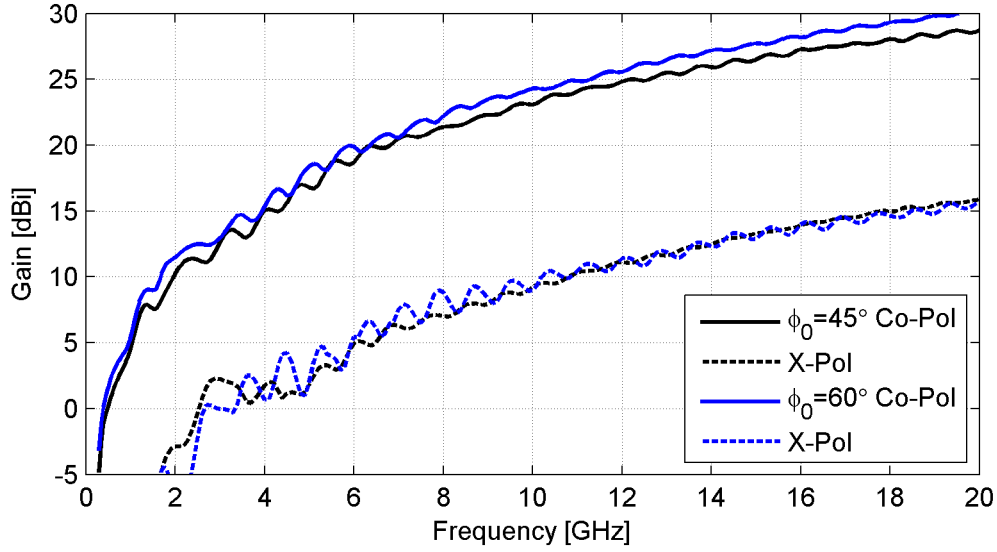
Figure 4.6. Boresight gain of the standard IRA designs.

the sidelobes are also lower in amplitude. This agrees with the findings of Tyo [22], who predicted better sidelobe performance from the $\phi_0 = 60°$ configuration using a physical optics approximation for $\pm 30°$ on boresight. What was not predicted in that paper was the significant perturbations in the sidelobe patterns as a function of frequency, a result of interactions with the feed structure of the antenna. Far out sidelobes and backlobes for the reflector IRA have never been predicted or presented in measurement, so we see for the first time that the H-plane has rather large backlobes at high frequencies. Still, the radiation seems to be confined in the forward hemisphere at the very low frequencies, so the search for the missing accepted power continues.

A unique insight that CEM solvers can provide over measurement in the physical world is the ability to monitor fields, currents, and other quantities without perturbing the measurements. We now use this ability to consider the power losses in the resistors as a percentage of the excitation power. Figure 4.9 makes it immediately clear that power losses in the resistors of the matching circuit are a significant factor at the lowest frequencies. In the limit that the excitation frequency approaches DC, the

57
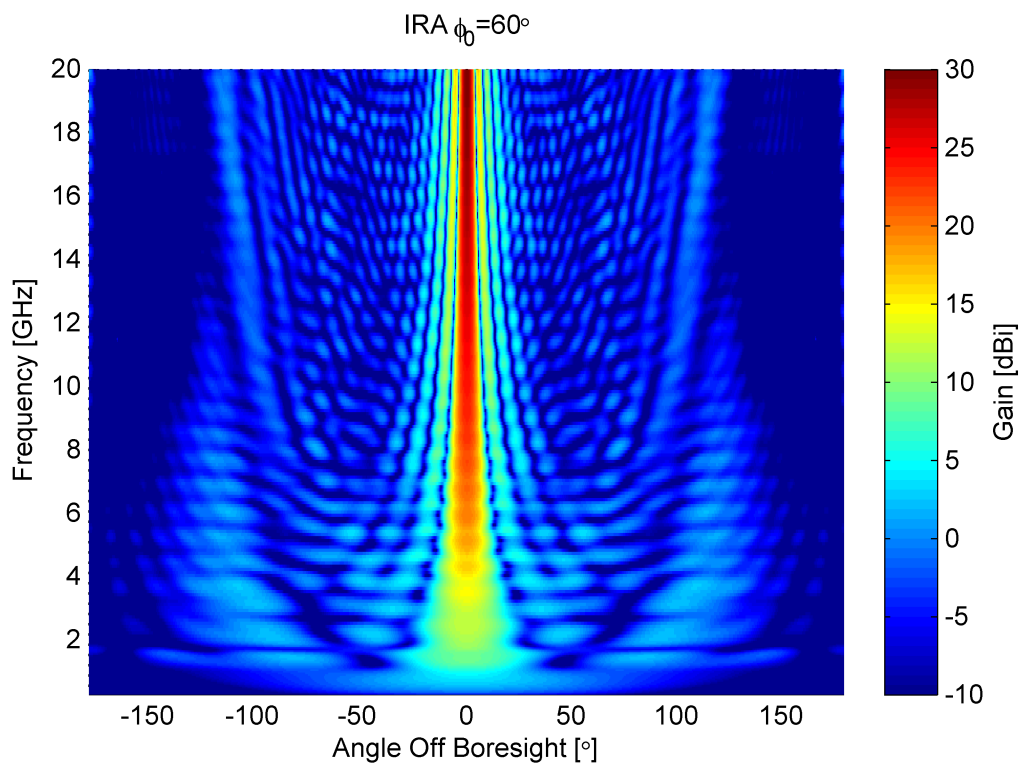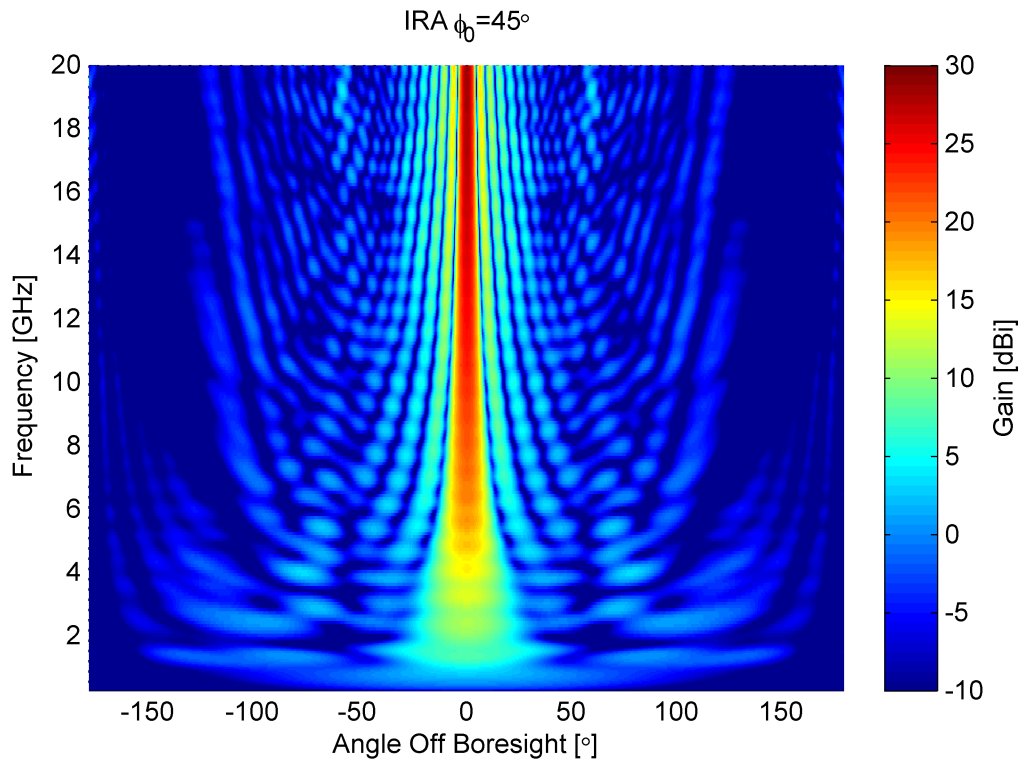
Figure 4.7. E-Plane gain pattern vs frequency for the standard IRA designs.

IRA ϕ_0=45°

IRA ϕ_0=60°
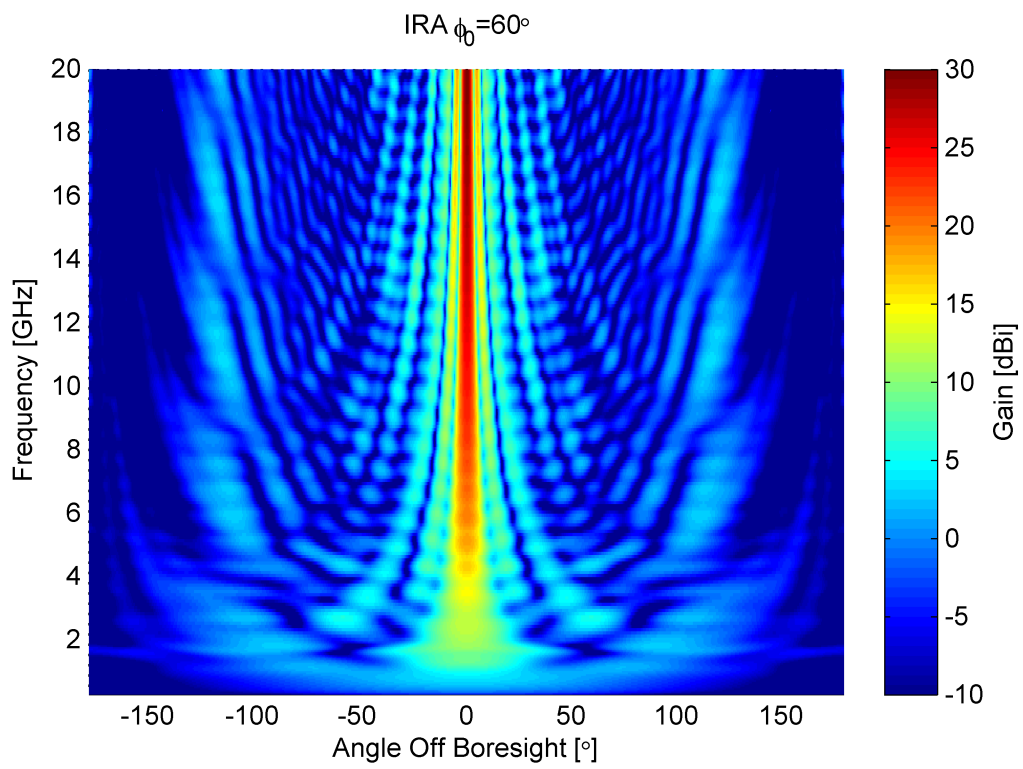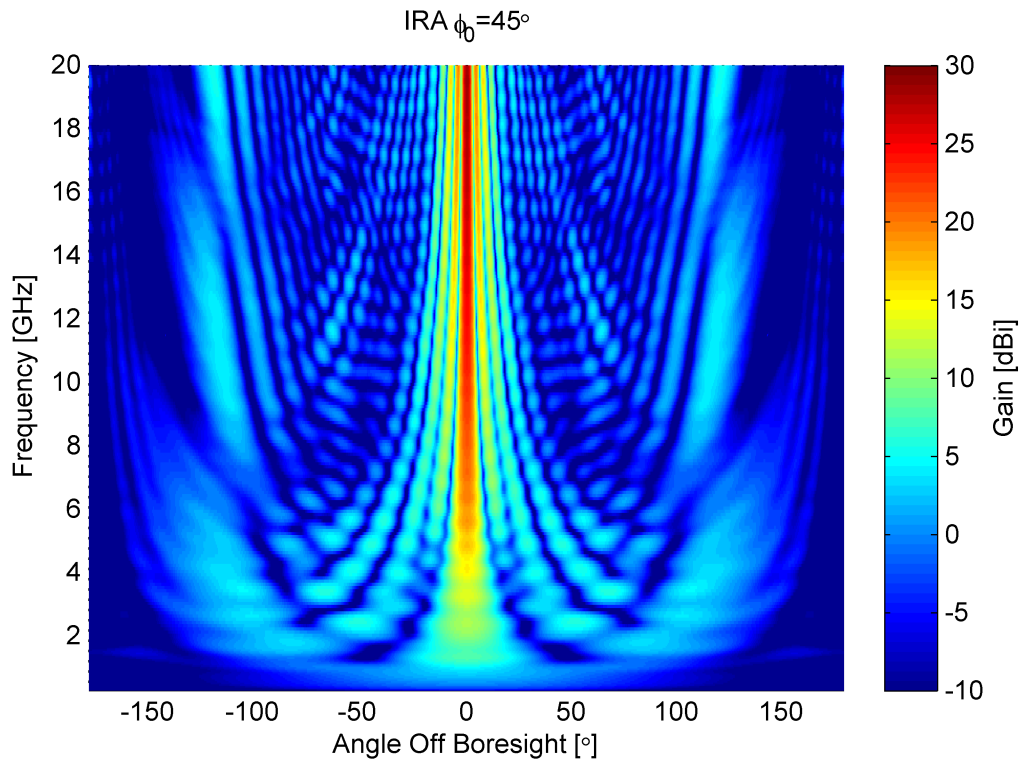
Figure 4.8. H-Plane gain pattern vs frequency for the standard IRA designs.
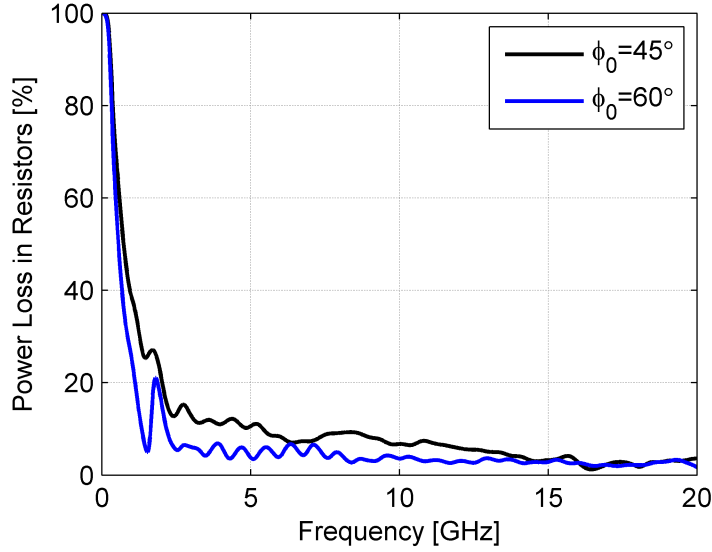
Figure 4.9. Power losses in the resistive elements of the standard IRA designs. For a total resistance that matches the feed impedance, and in the limit as the excitation frequency approaches DC, 100% of the power is absorbed in the resistors.

matching circuit absorbs 100% of the excitation power. This is noted as an area to investigate for improving low-frequency performance. It is also noted that very little power ends up in the resistive elements at high frequencies, and recalling the S_{11} performance, not much is reflected out the port either. It may be worthwhile to determine how much is radiated in the forward and rear hemispheres.

The total radiated power (TRP) was integrated over each hemisphere for the $\phi_0 = 60°$ IRA, and the result is plotted in Figure 4.10. Nearly 40% of the stimulated power ends up being radiated into the rear hemisphere at high frequencies! Armed with this knowledge, we take a more critical look in three dimensions at the radiation patterns of the reflector IRA. The findings are presented in Figure 4.11 and Figure 4.12.

We see now that the reflector IRA has a significant issue with backlobes, not directly opposite the boresight direction, but aligned in the $\phi = 45°$ planes. These lobes are wide and essentially frequency independent, which suggests the impulse response in these directions may also be significant, although this has not been investigated yet. It appears that the effectiveness of the matching circuit design at "catching" the
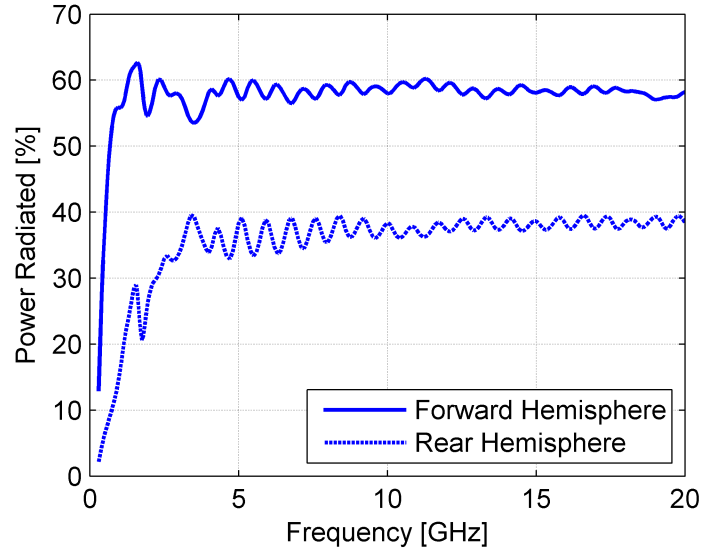
Figure 4.10. Radiated power by hemisphere as a percentage of the excitation power for the $\phi_0 = 60°$ standard IRA. A significant amount of power is radiated in the rear hemisphere at high frequencies.
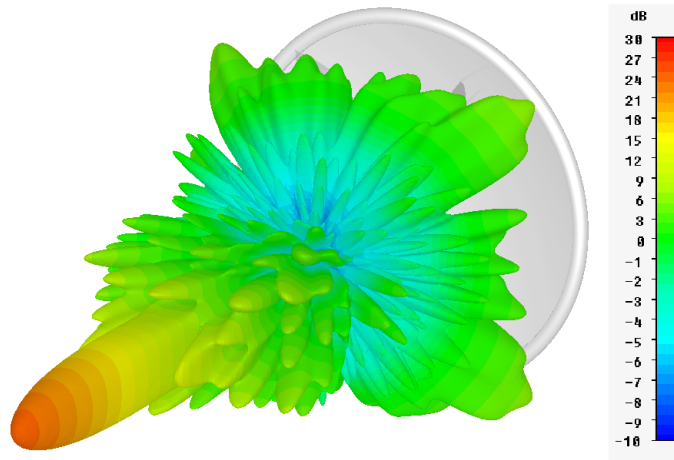
Figure 4.11. 3D gain pattern for the $\phi_0 = 60°$ standard IRA at 10 GHz, showing significant backlobes in the $\phi = 45°$ planes.

61
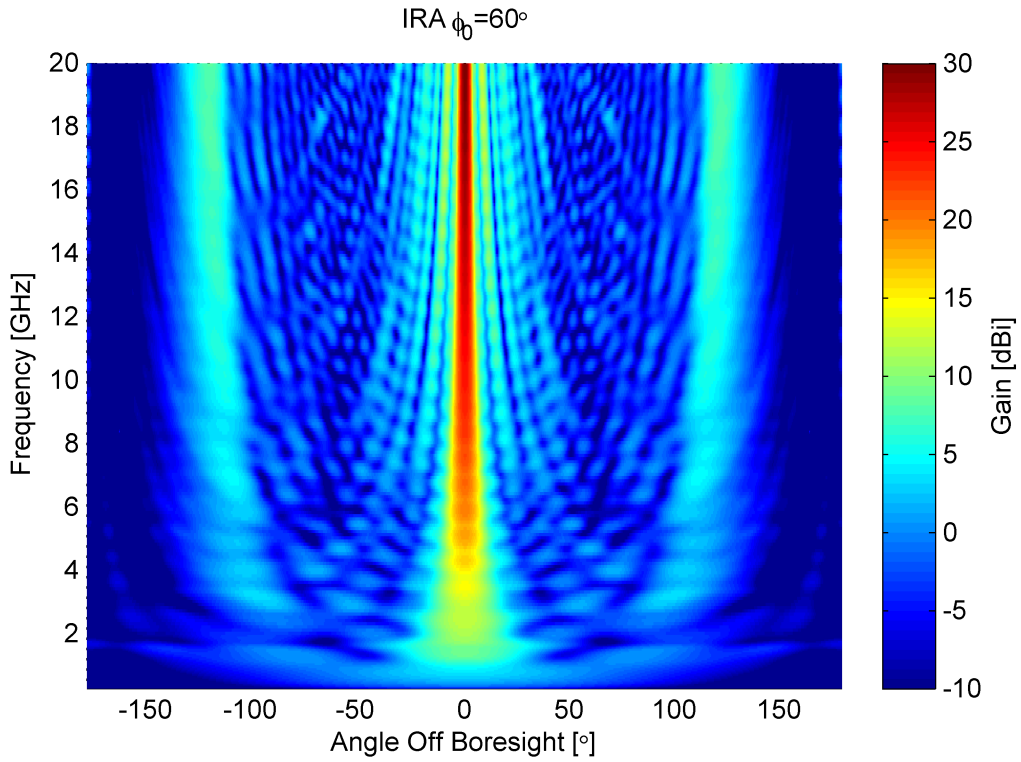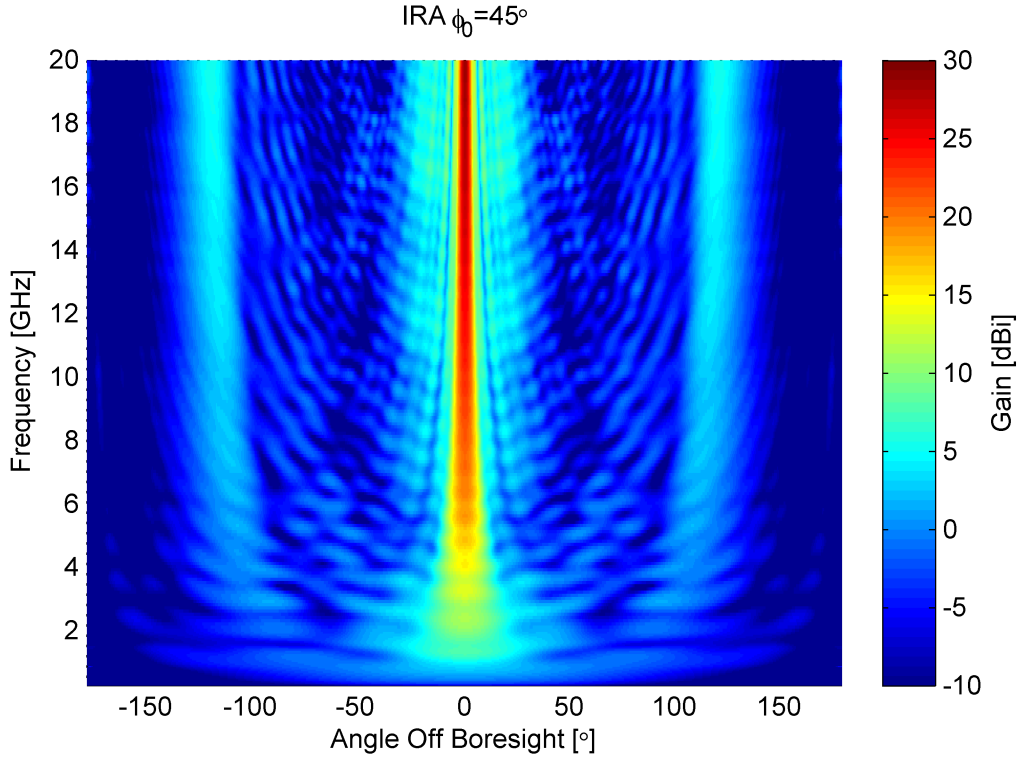
Figure 4.12. $\phi = 45°$ **plane gain pattern vs frequency for the standard IRA designs. Note the strong backlobes that are nearly constant across all frequencies.**

62

currents on the feed arms has been overestimated. The discontinuity presented in the transition from a wide planar conductor into thin wires results in a charge acceleration and quite efficient radiation to the rear of the antenna at frequencies above about 3 GHz. It appears also that the superposition of fields radiated rearward from each feed arm sums into the $\phi = 45°$ plane, regardless of the ϕ_0 angle of the arms, at least in the two cases observed here.

4.2.3 Section Summary.

In this section, the characteristics of two standard reflector IRA configurations were analyzed for time- and frequency-domain performance. The time domain performance on boresight was generally as expected with high peak impulse response and low ringing. A close look at the frequency domain performance in three dimensions revealed the existence of large, frequency-independent backlobes through most of the operating frequencies of the antenna. The existence of these backlobes has never been hypothesized or reported in the published literature. No record of actual measurements of a reflector IRA has been found that includes data for greater than 90° off boresight, but the alignment of these major backlobes outside of the primary E- and H-planes of the antenna may still make identification unlikely. Some have suggested the reflector IRA as a suitable candidate in a multi-role or multi-frequency application due to its UWB operating characteristics. However, the existence of these large backlobes likely precludes the reflector IRA from being utilized as a multi-role antenna at the higher frequencies, unless some effort is made to suppress or otherwise account for them.

Fortunately, the frequency range of interest for the AFIT noise radar is not affected by these backlobes. On the other hand, the performance at these frequencies is characterized by high resistive losses, low gain, and low radiation efficiency. The

$\phi_0 = 60°$ standard IRA is chosen as the baseline for comparison from this point forward, due to its superior characteristics in nearly all aspects over the $\phi_0 = 45°$ IRA. Before beginning simulation experiments to consider low-frequency performance improvements, a more detailed characterization was performed comparing a 12-inch $\phi_0 = 60°$ IRA to the existing log-periodic antenna of the AFIT noise radar. This was done to ensure that the baseline performance of the IRA was comparable enough to the log-periodic to be a realistic candidate for application to the noise radar, regardless of whether low frequency improvements were discovered. Results indicating that the 12-inch reflector IRA may be suitable for the AFIT noise radar can be reviewed in Appendix B.

4.3   Simulation Experiments

Having predicted a 12-inch standard $\phi_0 = 60°$ reflector IRA design to perform reasonably in the UHF band of the AFIT noise radar (Appendix B), some simulation experiments were performed to determine if any additional improvements could be found. The main goal was primarily to enhance the realized gain on boresight at the lowest operating frequencies of the antenna.

4.3.1   Initial Exploration.

It was noted early on that very few have researched the detailed effects of the matching circuit geometry and configuration on the reflector IRA performance. Some who performed full-wave simulation used simplified geometries with a single resistor and looked only to the effects on the radiated far field for a few different resistor values [19]. The results of changing resistor values was found to be negligible. Others have experimented in the lab or in the field with some resistor modifications, but used only the TDR response as a metric for assessing the effect of the modification [9, 17].

In this case the goal was to flatten the TDR response at the end of the feed arms as much as possible, and in all cases it was found to be impossible based on resistor values alone.

It was within this context that an initial exploration began to also attempt to flatten the simulated TDR response at the matching circuit. Recalling that much of the high frequency excitation is "immune" to the resistors, an attempt was made to smooth the transition from planar feed into the thin wires. The initial hypothesis was that an elliptical cutout at the end of the arm would both increase the impedance to counteract the large dip, and also smooth the transition into the wires of the resistors. The result of adding various elliptical cutouts was that the impedance at the end of the feed was increased as expected, and a larger amount of high frequency current was absorbed in the resistors. However, the large dip seen on the TDR was largely unaffected, and the general result was a decrease in gain on boresight. This was counter to the overall goal of improving gain at the low frequencies, so further exploration of shaping the ends of the feed arms was halted.

Next, an investigation of the resistors of the matching circuit was begun, still with a goal of flattening the simulated TDR and perhaps to try and replicate some measured data. The currents flowing through the resistors were analyzed, and it was noted that more current flows through the inner resistor chain. In an attempt to balance the current loads, the ratio of the resistance between inner and outer edges was modified, while keeping the total resistance matched to Z_{feed}. The current flowing through the outer chain was increased, and the current flowing through the inner chain was decreased successfully. A small but noticeable effect was seen in the TDR response. The change in resistance values also resulted in a decrease in performance in the mid-bands of the region of interest (400-500 MHz), but only by tenths of decibel values. Modifying the resistors to balance the current in the opposite

direction resulted in the expected effects on the current amplitudes, and also resulted in an increase in gain at the mid-band by a small amount.

Carl Baum noted in the very first paper that the matching circuit might be tuned to balance the electric and magnetic dipole moments of the reflector IRA for improved low-frequency performance [5], but no papers were found indicating attempts to do so. As the main goal for the impulse-radiating community has been to maximize aperture efficiency and the peak radiated fields, this is not terribly surprising. For this thesis, however, improved low-frequency performance is of interest.

A hypothesis began to take shape. The electric dipole moment is proportional to the distance and magnitude of the charge separation; the magnetic dipole moment is proportional to the current magnitude and the area of the loop of current. Considering the results of the resistor and current balancing attempt, the improved performance came when the current was forced to flow more through the inner resistor chain (smaller loop area), and high resistance on the outer edge improved the voltage hold-off capability and vertical distance of the charge separation. This suggested that an increase in the electric dipole moment and decrease in the magnetic dipole moment was in order.

Continued efforts at modifying performance of the standard IRA by distributing the resistance and balancing currents while maintaining a total impedance match were met with some success, but with modified gains of only tenths of decibels at best in the frequency range of interest. It was decided that increasing the total resistance would likely give better results by further increasing the voltage hold-off at the end of the feed arms and increasing the electric dipole moment. A small study where the total resistance was modified as a fraction of the feed impedance confirmed this hypothesis, and the results can be observed in Figure 4.13. It is seen that the gain in the mid-band of the AFIT noise radar monotonically increases with increasing total

66

Figure 4.13. Boresight gain with modified resistance values for a standard $\phi_0 = 60°$ IRA. The k_{tot} parameter indicates the total resistance of the matching circuit as a fraction of Z_{feed}. From this limited study, it is shown that there is more than 2 dB of performance variation achieved in the mid-band by simply modifying the resistor values.

Figure 4.14. VSWR results with modified resistance values for a standard $\phi_0 = 60°$ IRA. The k_{tot} parameter indicates the total resistance of the matching circuit as a fraction of Z_{feed}. The VSWR at the low end of the frequency range increased with increasing resistance.

resistance of the matching circuit. However, there appears to be an inflection point near 350 MHz, and below this value the trend is reversed, albeit with a much smaller effect. Searching through other metrics indicated that in the mid-band, radiation and total efficiency also improved with increased resistance; less power was lost in the resistors. However, this increased performance comes at a price. A look at the VSWR shown in Figure 4.14 indicates that while more power is radiated, more power is also reflected. What is particularly interesting is that the VSWR at the low frequencies can essentially be set by choosing the resistor values, so a maximum acceptable VSWR can be specified and resistance values can be modified to increase the boresight gain

under this constraint.

A look at the TDR response for this experiment shows the effect of the modified resistance at the late times (Figure 4.15). The effect is fairly dramatic, and for one interested in maintaining a flat TDR, these would be seen as poor results. However, a look at the rest of the spectrum in Figure 4.16 indicates that the effects observed are largely confined to the low frequencies. The nearly consistent performance across the rest of the spectrum should mean that the impulse response is also largely unaffected. Before investigating whether this is true, some other experiments were devised.
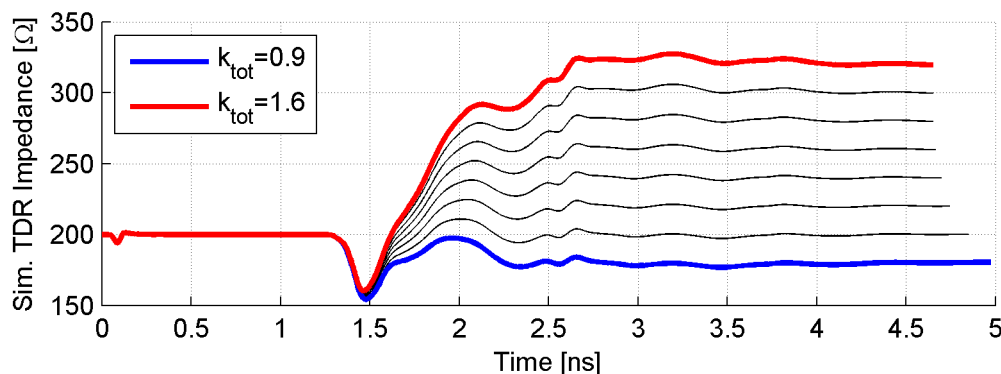
Figure 4.15. TDR results with modified resistance values for a standard $\phi_0 = 60°$ IRA. The k_{tot} parameter indicates the total resistance of the matching circuit as a fraction of Z_{feed}. The late-time TDR response matches to the $k_{tot} \cdot Z_{feed}$ value precisely.
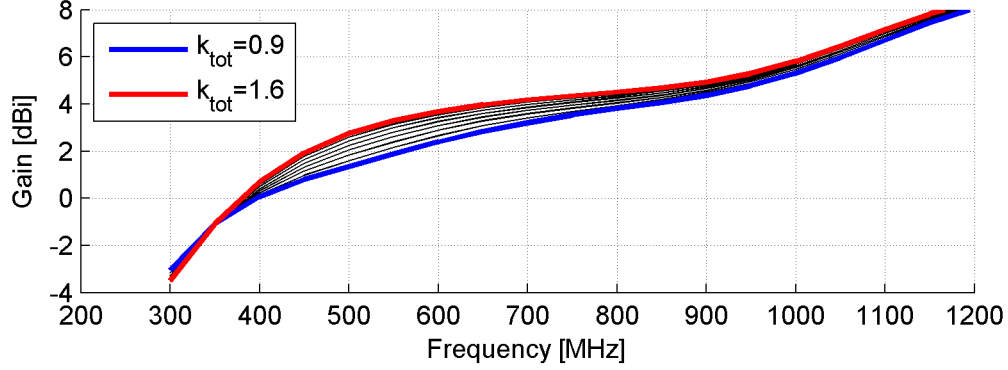

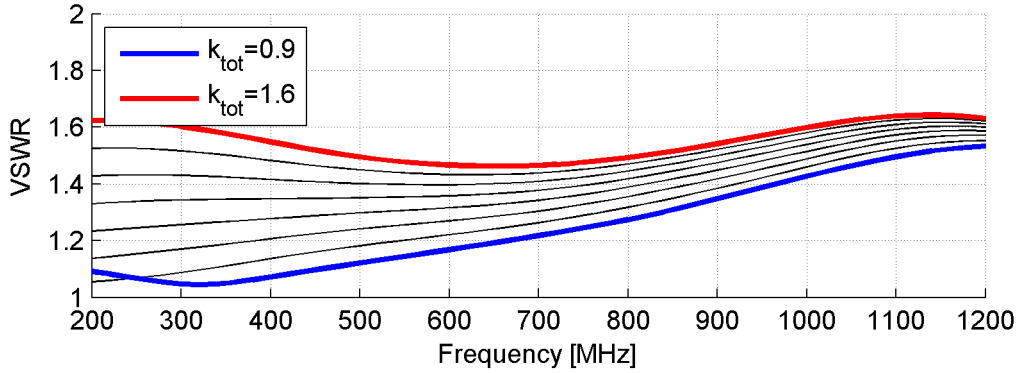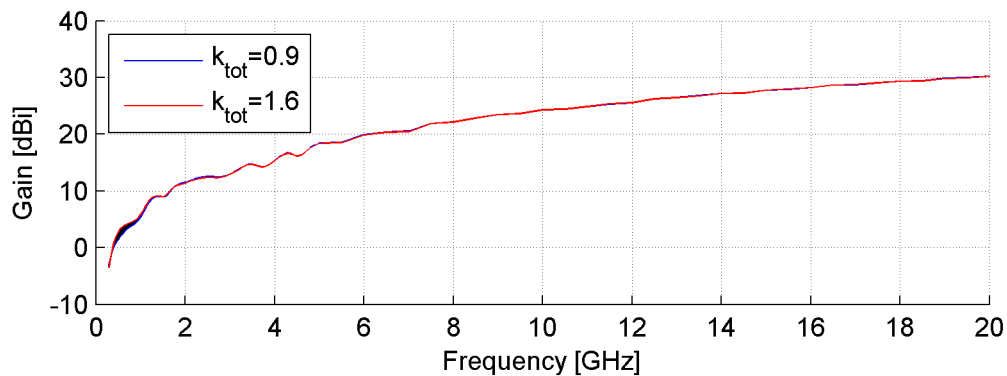**Figure 4.16. Full spectrum boresight gain results with modified resistance values for a standard $\phi_0 = 60°$ IRA. The k_{tot} parameter indicates the total resistance of the matching circuit as a fraction of Z_{feed}. The effects of modifying the resistor values are largely confined to below 2 GHz.**

As a brief summary on the simulation experiment thus far, it was determined

that some very modest improvements in gain at low frequencies could be effected by balancing resistor values and currents while maintaining the total match to the feed impedance; it was shown that an even greater variety of gain effects could be achieved by increasing or decreasing the total resistance relative to the feed impedance. The hypothesized means of achieving greater boresight gain at UHF frequencies was to increase the electric dipole moment of the antenna. An additional idea on how to accomplish this came from a paper describing efforts to optimize the field distribution on the aperture for improved impulse radiating performance [21]. In this paper it was suggested that adding additional non-blocking arms into the feed structure could improve the field distribution on the aperture. The hypothesis formed from combining these two ideas was this: adding a pair of purely vertical arms to the feed would give the best geometric configuration for maximizing the electric dipole moment at low frequencies, and may also act to improve the field distribution on the aperture for improving the impulse-radiating performance.

4.3.2 N-Arm Feed Design.

In order to maintain the impedance matching capabilities of the existing reflector IRA cabling system, the first goal was to design a new multi-arm feed with characteristic impedance $Z_{feed} = 200\ \Omega$. The capability to do this using the simulated TDR and optimization routines in CST was demonstrated during the initial model and methodology verification, so the same process was followed once again. The results of the original two-pair and some various three- and four-pair feed arm designs are compiled in Table 4.2.

An interesting observation is that as additional arms are added to the feed, the impedance of each arm pair increases to maintain the total feed impedance at 200 Ω, and high-impedance arms are thinner than low-impedance arms. This is a desirable

Table 4.2. Z_{arm} or b_1/a parameters required to achieve $Z_{feed} = 200\ \Omega$ for various multi-arm configurations. The data is grouped in two-, three- and four-pair arm configurations.

	ϕ_0	$Z_{arm}[\Omega]$	b_1/a
2-Arm	$45°$	400	0.8671
	$60°$	335.9	0.7834
3-Arm	$\{55°, 90°\}$	399.1	0.8662
	$\{60°, 90°\}$	364.4	0.8252
	$\{65°, 90°\}$	330.6	0.7747
4-Arm	$\{45°, 60°\}$	499.2	0.9396
	$\{55°, 65°\}$	404.6	0.8718
	$\{55°, 70°\}$	416.8	0.8835

result from the standpoint that the arm geometry will be less abrupt at the matching circuit. It may also introduce the possibility of building a reflector IRA in what is termed the *rigid* configuration [21], wherein the arms are fully contained inside the rim of the parabola (β_2 aligned to the rim of the reflector), without significantly adding to the undesirable components of the field distribution on the aperture. The rigid configuration may also be a way to control the backlobes. Thinner arms, on the other hand, will make the task of constructing a sturdy antenna more difficult and the total feed impedance may be more sensitive to geometric imperfections. With these considerations in mind, but also continuing the hypothesis that a purely vertical pair of arms would provide the best opportunity to balance the electric and magnetic dipole moments, a three-pair configuration with $\phi_0 = \{60°, 90°\}$ was chosen for further study. The standard design rule for β_0 aligned to the rim of the reflector was maintained.

4.3.3 Three-Arm IRA.

The IRA configuration with three pairs of feed arms at $\phi_0 = \{60°, 90°\}$ was constructed in simulation. The model is shown in Figure 4.17. Before starting experiments to further modify or optimize the performance of the three feed arm (3FA) IRA, its characteristics in the default matching circuit configuration are compared to
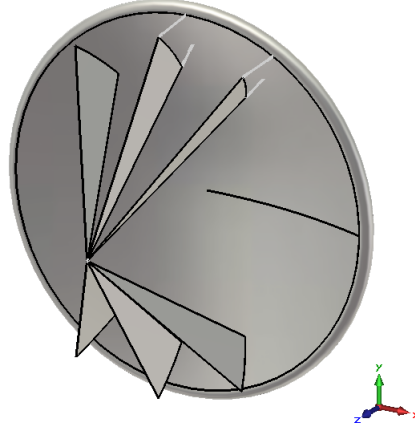
Figure 4.17. The three-pair feed arm (3FA) reflector IRA that was studied for improving low-frequency performance.

the baseline $\phi_0 = 60°$ IRA. The realized gain on boresight is shown in Figure 4.18. While there is a slight decrease in performance above 650 MHz, the 3FA IRA shows a modest improvement at the low end of the UHF spectrum, so it is deemed suitable to continue with the experiment.
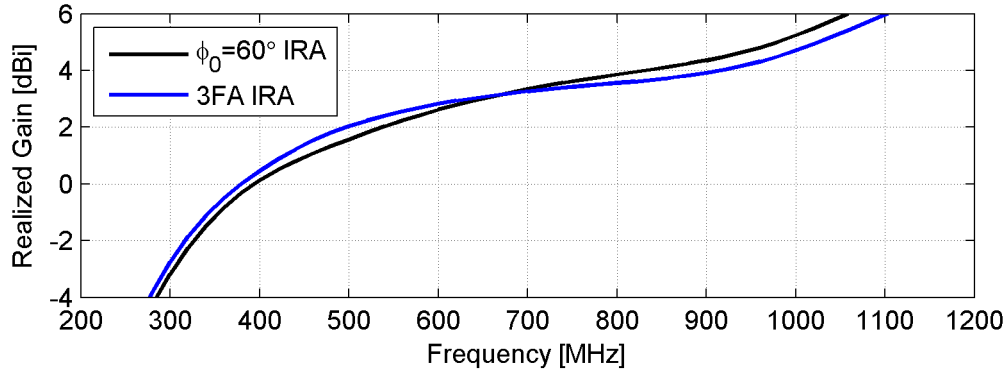
Figure 4.18. Realized gain for the baseline 3FA IRA and standard $\phi_0 = 60°$ IRA. The 3FA IRA shows a modest increase at the lowest frequencies, and is deemed suitable for further experimentation.

Now, because the primary goal was to improve the gain of the antenna (a frequency domain metric) at a limited set of frequencies, the computational resources available could be more effectively utilized by reducing the scale of the simulations. The frequency domain solver in CST is well-suited to this task. Before beginning

an extended set of parameter sweeps or optimizations, the results from both solvers were compared for cross-verification. The S_{11} parameter is a primary metric for mesh refinement in each of the solvers, and the realized gain is used as a metric for the optimization of performance, so these two results were compared for each solver, shown in Figure 4.19. The results are nearly indistinguishable, giving confidence that the FD solver can be used for the parametric sweeps and optimization experiment with no reservations.
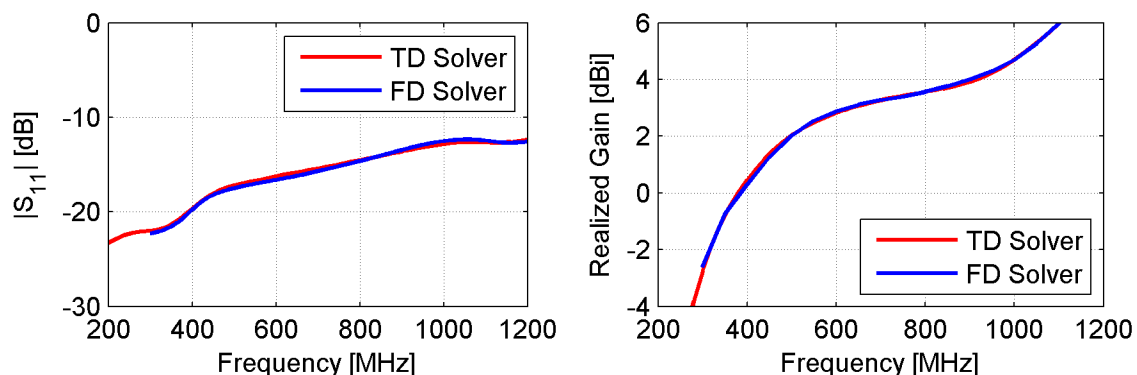
Figure 4.19. Comparison of $|S_{11}|$ and realized gain for the 3FA IRA calculated with two different solvers. The close agreement indicates consistent behavior between the solvers. The FD solver is used to perform parametric sweeps and optimization routine on the 3FA IRA matching circuit.

4.3.4 Single Parameter Sweep.

The addition of a third feed arm introduces new options for modifying performance while maintaining a matched resistance. One option that seemed promising was to vary the ratio of the resistance on the center feed arm relative to the outer feed arms, while maintaining the total resistance matched to Z_{feed}. The metric for comparison is the realized gain, so that if modifications result in higher power losses due to reflections, this is accurately accounted for. The parameter k_{arm} was implemented to describe the ratio of the total resistance on the middle arm to the resistance on an outer arm. This parameter was varied logarithmically from 1:10 (very low

resistance on the middle arm) to 10:1 (very high resistance on the middle arm), and the results are displayed in Figure 4.20. With three feed arms there is a greater degree
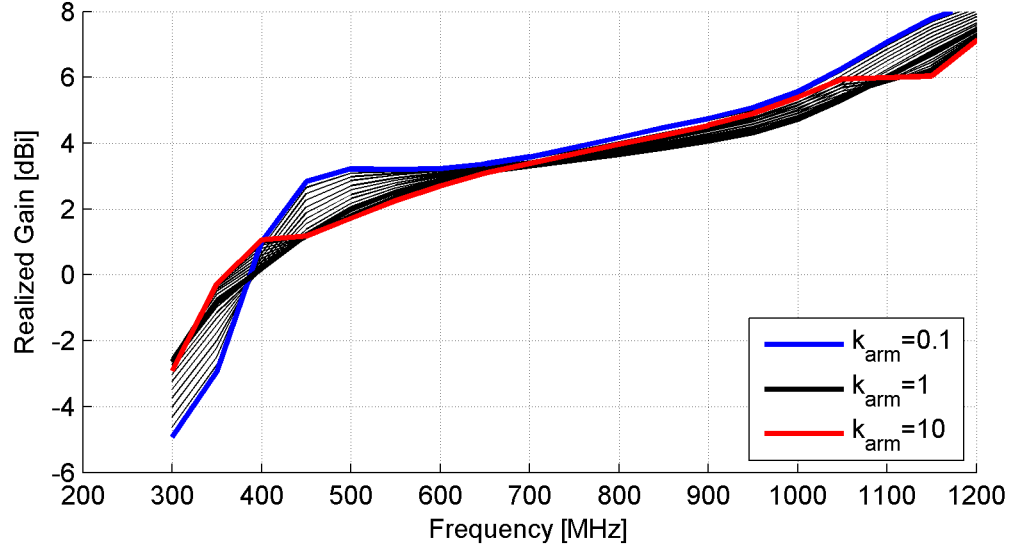
Figure 4.20. Realized gain for a parametric sweep of resistor ratios on the 3FA IRA. The k_{arm} parameter describes the ratio of resistance on the middle vertical arm to the resistance on an angled arm; the total resistance of the matching circuit was maintained as a match to Z_{feed} for this experiment.

of performance variation available from changing resistor ratios while maintaining a total match, when compared to similar attempts on a standard two feed arm IRA. The dependencies are slightly more complex. With a discrete set of sample points, the fine behavior is unknown, but it appears that strange resonances may be excited, especially at the extreme ratios. The behavior is not monotonic with the k_{arm} ratio across a wide frequency band, but has various inflection points where the nature of the k_{arm} effects are reversed. One ratio that showed a smooth behavior and slight performance improvement was $k_{arm} \approx 2$, or the resistance on the center arm twice that of each outer arm. This ratio was noted as a possible starting point for further exploration. However, the primary result from this simulation experiment was to demonstrate that varying the k_{arm} ratio alone had a significant effect on antenna performance, and was an additional option for tuning performance. Now, instead of

73

putting a significant effort into manually exploring the tradespace available in the matching circuit, the opportunity to employ automation was realized in the use of an optimization routine.

4.3.5 Optimization.

As noted previously, the default matching circuit configuration that was chosen on the standard IRA consists of two chains of two resistors each at the end of each feed arm. With the addition of a third pair of arms, the various possibilities for balancing the resistor values are increased to the point where manually sweeping through parameter sets and analyzing every combination becomes quite cumbersome. Instead, the genetic optimizer algorithm in CST employed to manipulate the configuration of resistor values. The model was set up to allow for varying resistance ratios within and between the two resistor chains attached to each arm, the ratio of the resistance between the arms, and the total resistance relative to the feed impedance. This resulted in a set of eight parameters for the optimizer to work with. A goal was set to achieve 1 dB of realized gain at 300 MHz. Given the range of values observed previously, this was deemed a bit unrealistic but was expected to generate some interesting results for further analysis. Nearly 300 separate configurations were run by the optimizer before it was terminated due to external influences. The available results were explored in terms of the realized gain across the bandwidth of interest, VSWR and S_{11}, and radiation efficiency.

Because of the limited optimization goal, the final "optimized" configuration wasn't necessarily the ideal configuration for the noise radar application. However, in attempting to achieve an optimized configuration as defined, the algorithm explored most of the trade space it was given. A composite plot of realized gain over all the optimizer configurations is shown in Figure 4.21, indicating quite a significant envelope

in which the 3FA IRA can be tuned simply by modifying resistor values. Highlighted on the plot are two specific configurations that were chosen for further study.
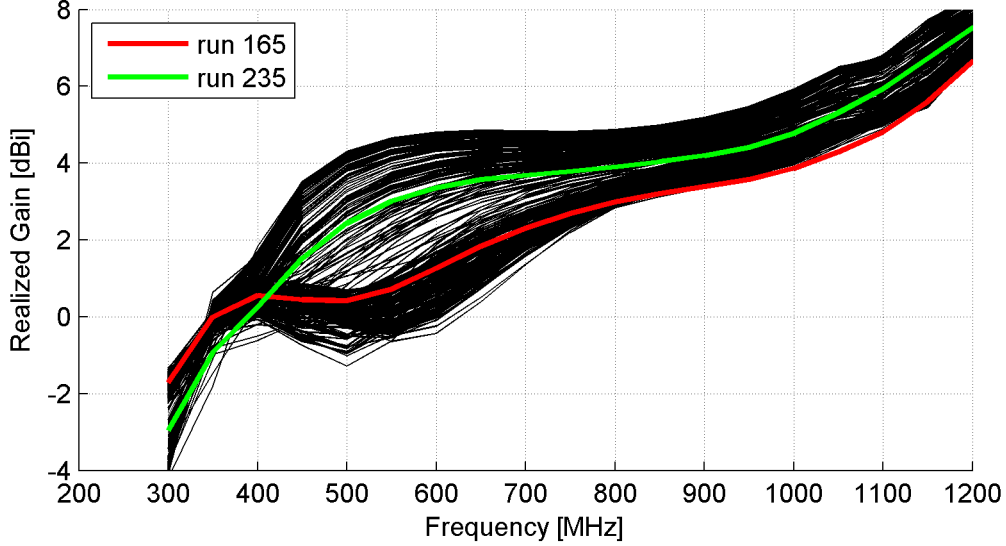
Figure 4.21. Composite realized gain for optimization of resistor values on the 3FA IRA. The data set indicates a significant envelope in which performance can be tuned simply by modifying the resistor values. Two configurations chosen for further study are highlighted.

The two highlighted resistor configurations can be briefly described as follows:

- **Run 165:** A high $k_{arm} \approx 3.5$ with a low $k_{tot} \approx 0.5$ means the middle arm has a greater resistance than the outer arms, but the total resistance in the matching circuit is decreased. The other parameters favor pushing the currents to the outer resistor chains, so the magnetic dipole moment of this configuration is likely greater than the standard configuration. The realized gain nearly matches the optimized configuration at 300 MHz, but the characteristics over the rest of the frequency range are smoother.

- **Run 235:** A moderate $k_{arm} \approx 1.3$ and a moderate $k_{tot} \approx 1.4$ indicate that the electric dipole moment of the configuration is likely greater than in the standard configuration, based on the initial experiments. This configuration was chosen for its fairly flat gain response across a wide band in the upper half of the frequency range of interest (about 550-1000 MHz).

Many of the configurations in the data set, especially those with the highest gain, are marked by high VSWR and S_{11}. Run 165 and 235 have good or acceptable

performance in this regard, as shown in Figure 4.22, which is one factor that led to their selection for additional study.
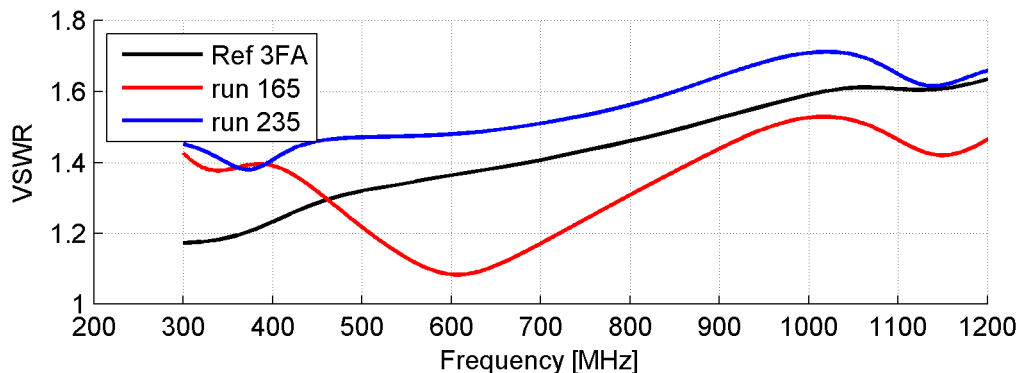
Figure 4.22. VSWR for two 3FA IRA designs with modified resistor configuration. The configurations of Run 165 and 235 were chosen in part due to the smooth behavior over frequency. Some of the more extreme cases (not shown) had much sharper features.

The configurations of optimizer Run 165 and Run 235 were re-simulated using the TD solver to generate data for a final comparison in both time- and frequency-domain performance. In the frequency domain, the boresight realized gain for the reference $\phi_0 = 60°$ IRA, the reference 3FA IRA and both modified designs is shown in Figure 4.23. The realized gain patterns in the two principal planes can be compared for all the same designs in Figures 4.24 and 4.25. For all designs, the patterns in both E- and H-planes are characterized by a single very wide main lobe oriented on boresight and essentially no side- or backlobes. The configuration of Run 165 has the greatest deviation from the rest of the patterns, especially in the H-Plane, where the reduced boresight gain around 500 MHz translates into a much wider beam. At the higher frequencies, all designs display a rapid narrowing of the main beam just before the first nulls and sidelobes are formed. This is a best-case scenario for the AFIT noise radar application, where a fairly consistent radiation patter across frequency is preferred; a larger antenna will begin forming sidelobes at lower frequencies which may be undesirable in this case.

In the time domain, the TDR response (Figure 4.26) shows that the total resistance

Figure 4.23. Realized gain for the reference $\phi_0 = 60°$, the reference 3FA and two 3FA reflector IRAs with modified matching circuit resistance values.

is the dominating parameter in determining the overall shape and especially the late-time response of the antenna. The large dip seen at the end of the feed arms is more severe in the 3FA designs than for the reference $\phi_0 = 60°$ IRA, but the consistency between the three 3FA designs suggests the dip is due more to the geometry of the antenna than the component values in the matching circuit. Without more data points for comparison, it is difficult to discern what effects the other resistor ratios may have on the TDR response, but it is possible that they may damp out or sharpen some of the secondary and tertiary reflections seen after the large dip.

The extracted boresight impulse response and the key time domain metrics are tabulated in Table 4.3. The 3FA reflector IRA designs show a slight decrease in the peak value relative to the $\phi_0 = 60°$ IRA, but are relatively stable between designs and modifications on most of the other metrics. The consistent behavior among the three 3FA designs continues to suggest that the matching circuit has very little impact on the high frequency behavior of the antenna, which was determined to be the most significant factor in shaping the boresight impulse response behavior. A comparison of the boresight gain of the two reference designs reveals the reason for the decreased peak impulse response. Figure 4.27 indicates a region of decreased performance on the 3FA IRA significant enough to reduce the peak impulse response, and likely due to a
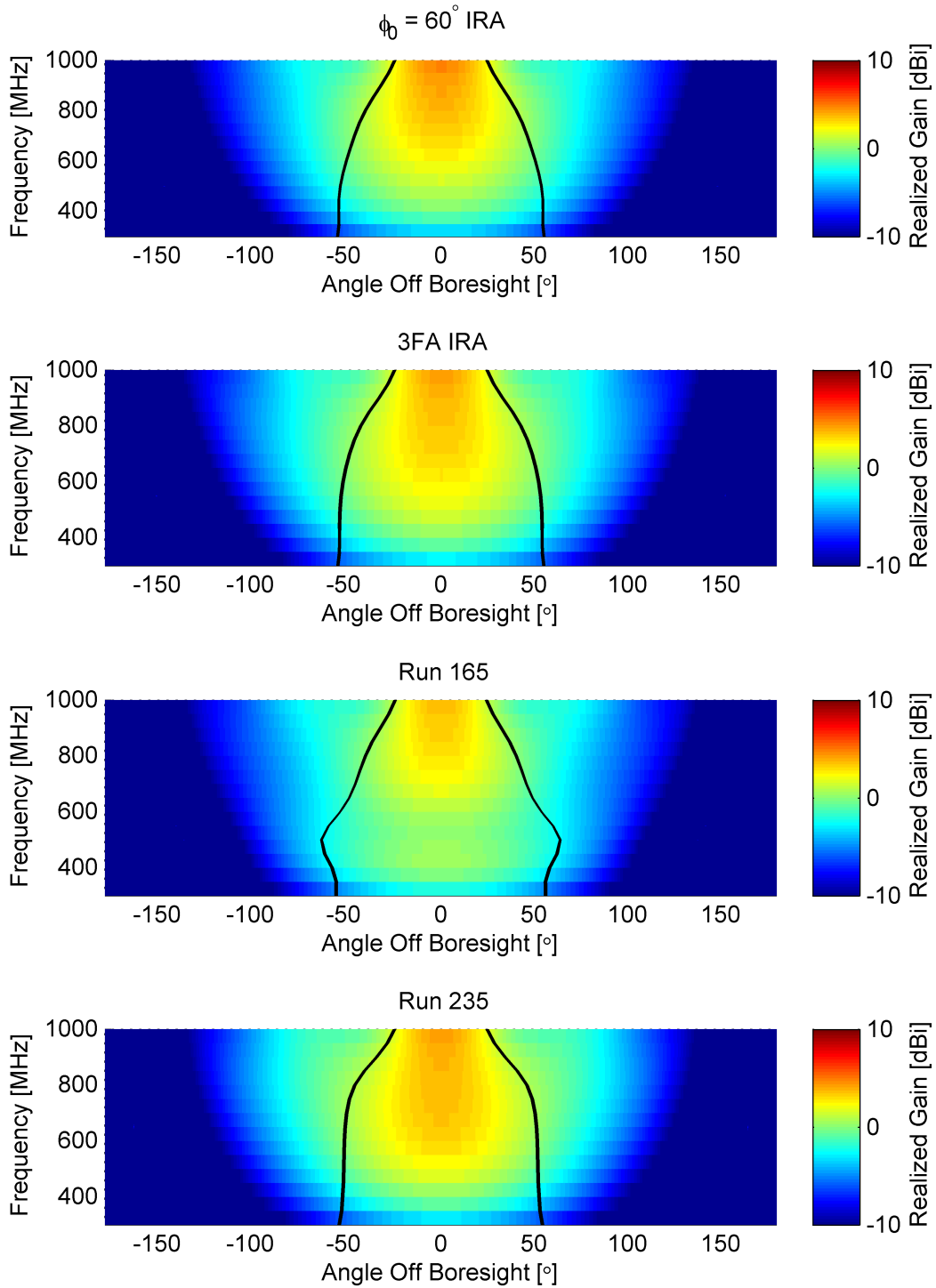
Figure 4.24. E-Plane realized gain pattern vs frequency showing the -3 dB beamwidth for the reference $\phi_0 = 60°$, the reference 3FA and two 3FA reflector IRAs with modified matching circuit resistance values.
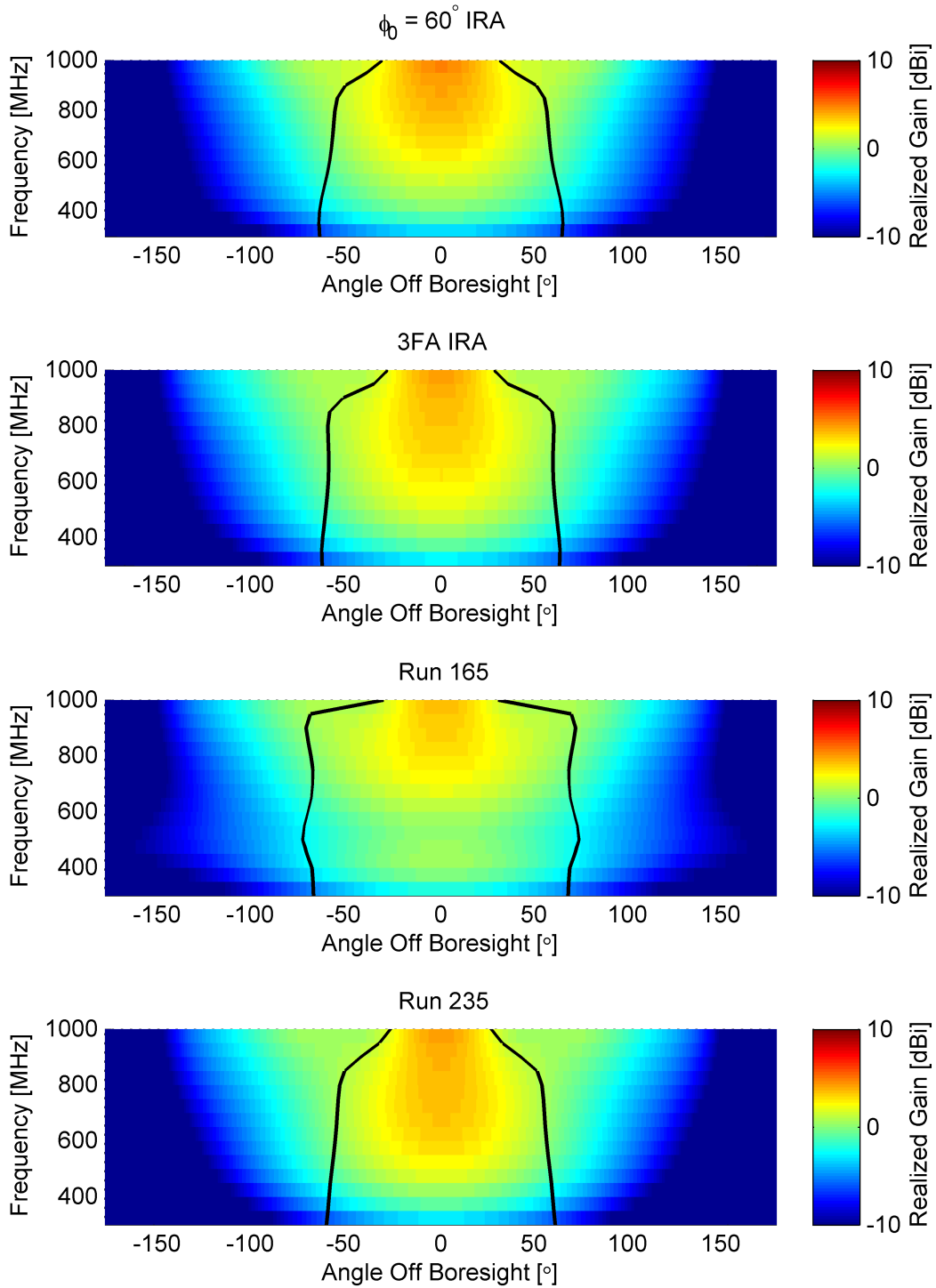
Figure 4.25. H-Plane realized gain pattern vs frequency showing the -3 dB beamwidth for the reference $\phi_0 = 60°$, the reference 3FA and two 3FA reflector IRAs with modified matching circuit resistance values.
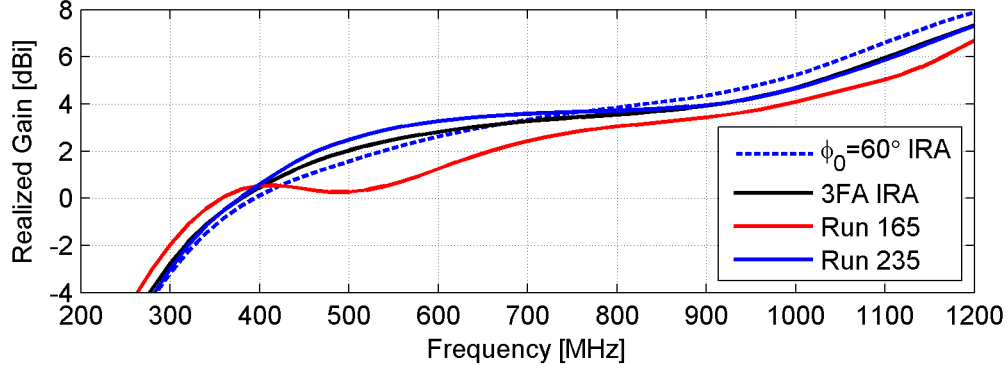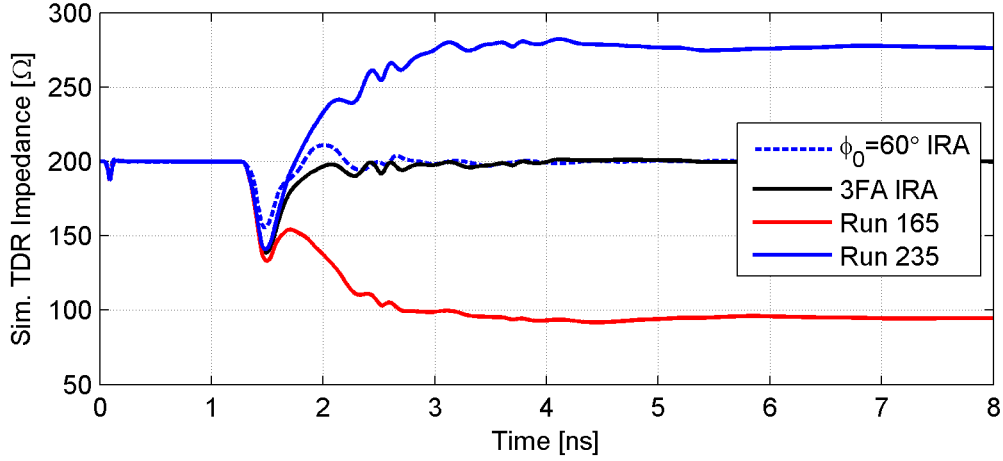
Figure 4.26. Simulated TDR response for the reference $\phi_0 = 60°$, the reference 3FA and two 3FA reflector IRAs with modified matching circuit resistance values. The total matching circuit resistance dominates in determining the overall shape and late-time response. The initial large dip at the end of the feed arms appears to be a consequence of the geometry of the antenna, and cannot be "fixed" by the matching circuit.

strong coupling of the reflected fields with the vertical arm of the feed. Interestingly, the 3FA actually displays better performance than the standard $\phi_0 = 60°$ design above 10 GHz.

4.3.6   Section Summary.

The simulation experiments described here have demonstrated two key results. First, we have demonstrated a means of designing feed configurations with additional arms, and have generated parameters needed to construct some various designs with three and four pairs of arms with a total feed impedance of $Z_{feed} = 200\Omega$. The benefit of adding arms includes a reduction in the necessary angular widths of the arms for a particular feed impedance. Higher ϕ_0-angles can be approached without the arms becoming unwieldy, and in theory, the field distribution on the aperture can be improved for better impulse-radiating performance. A new feed design with three pairs of arms was chosen for further simulation. In the simulated experiments, the peak impulse response was slightly decreased for the case of a third purely vertical

80

Table 4.3. Time domain metrics for some standard and modified reflector IRA designs, primary polarization on boresight. The consistent behavior of the three 3FA designs indicates that the matching circuit effects are negligible at higher frequencies.

		$\phi_0 = 60°$ IRA	3FA IRA	Run 165	Run 235
Peak $h(t)$	[m/ns]	5.47	5.34	5.32	5.34
Peak $|h^+(t)|$	[m/ns]	5.49	5.35	5.33	5.34
FWHM $h(t)$	[ps]	29.1	28.4	28.3	28.4
FWHM $|h^+(t)|$	[ps]	57.1	57.5	57.9	57.4
Ringing, $\tau_{r,0.22}$	[ps]	39.3	39.7	40.1	39.4
Ringing, $\tau_{r,0.10}$	[ps]	83.6	78.0	77.6	77.9
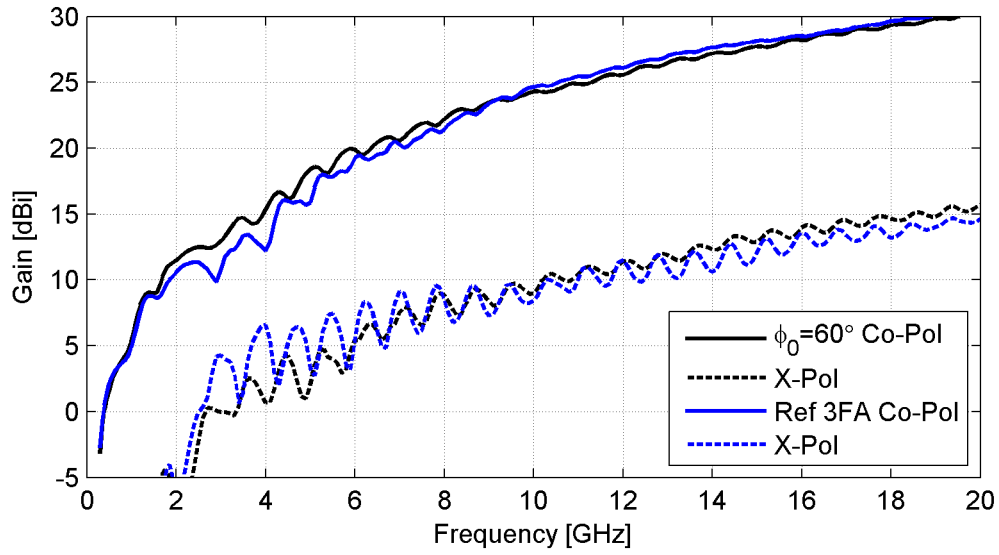
Figure 4.27. Boresight gain for the reference $\phi_0 = 60°$ and **3FA IRA** designs.

81

arm; this is likely attributable to the strong coupling of the vertical arm with the reflected fields, and a four-arm feed that maintains a centerline gap is probably the better choice for improving the peak impulse response. However, the vertical arm proved to be a useful additional means of tuning the low frequency performance. The second key result was to demonstrate that there exists a large envelope in which the low-frequency performance of the reflector IRA can be enhanced or tuned by simply modifying the resistance of the matching circuit at the end of the feed arms. This modification can be made to both the standard IRA configuration or one with three or more pairs of arms. This low-frequency tuning also seems to have a negligible effect on the high frequency performance, which dominates in determining the key time domain metrics for the boresight direction of the antenna.

4.4   Additional Analysis

In this final section of the chapter, additional thoughts and hypotheses on various topics regarding the performance and analysis of the reflector IRA are presented.

4.4.1   Discrete Performance Bands.

Having put a significant effort into analyzing various reflector IRA designs in simulation at various sizes, reflector characteristics, and matching circuit layouts (see also Appendices A and C) some trends can start to be seen across all the data. There appear to be two or three discrete frequency bands into which the performance of the reflector IRA can be empirically categorized, and they seem to be based primarily on the dimensions of the paraboloidal reflector. Of greatest importance is the focal distance, F. In all the designs analyzed here, the length of the feed arm is also set at F, which is a typical design guideline [6]. The reflector IRA performance is categorized as follows:

- **Low-Frequency.** The low-frequency performance that has been the primary interest in this thesis is characterized by unidirectional radiation on boresight with wide main beam and essentially no side- or back-lobes to speak of. There appear to be two primary mechanisms affecting performance in this region: the dipole-like nature of the feed structure, and the reflecting surface which is not yet operating as a focusing optic. Consider the matching circuit to be a "soft" extension of the dipole-like feed structure at the lowest frequencies. Then a lower resonance limit will be seen where the distance from the focal point to the rim of the reflector is $\lambda/4$, or where the full feed including the matching circuit approximates a bent half-wave dipole. On the 12-inch reflector, this distance is 8.45"; the corresponding $\lambda/4$ frequency is 349 MHz. This correlates well with the inflection point seen in Figure 4.13, where changes in the total resistance of the matching circuit seem to have no effect on the boresight gain. The lower limit for good performance comes at the hard half-wave dipole point, or where $F = \lambda/4$. This is due to both the strong half-wave dipole resonance of the feed and that the driven fields and the reflected fields will sum together on boresight. For the 12-inch reflector, $F = 7.2" = \lambda/4$ at 410 MHz. The driven and reflected fields approach a point of destructive interference at $F = \lambda/2$ at 820 MHz, and this serves primarily to flatten the performance, since the driven spherical waves and reflected not-quite-collimated waves don't perfectly cancel. It is in this region, 410-820 MHz, that the primary effects of the matching circuit are realized and radiation confined to only a main beam. Beyond 820 MHz, or the $F = \lambda/2$ frequency, the fields move back into a constructive beat pattern and the feed transitions from a bent dipole to a traveling or guided wave structure. The main lobe begins to rapidly become narrower as the focusing optic becomes more effective, and at the point where $F = 3\lambda/4$ or 1.23 GHz,

the first major sidelobes are fully realized in the E-Plane. Therefore, if the design goal for a reflector IRA is that of a unidirectional low-frequency antenna as in the applications considered here, the antenna should primarily be sized for $\frac{\lambda_{max}}{4} \leq F \leq \frac{\lambda_{min}}{2}$, with some leeway on either side.

- **Mid-Frequency.** The mid-frequency performance is empirically described by the region where the field interactions with the feed structure are the strongest, resulting the large oscillatory behavior in the main beam width and sidelobes that is not predicted by the optics approximations for the radiated fields. At the lower end, the first large features appear to be defined by resonances at approximately $F = 3\lambda/4$ and $F = \lambda$ (1.23 and 1.64 GHz for the 12-inch reflector), but beyond this the specific angles and geometry of the feed structure have a greater effect and the lobing is not quite as distinguishable as a function of F. Looking at both the patterns of Figures 4.7 and 4.8 and the boresight gain of Figures 4.6 and 4.27, an upper limit for the mid-frequency behavior might be defined around $F = 4\lambda$ or $F = 6\lambda$ (6.6 or 9.8 GHz for the 12-inch reflector).

- **High-Frequency.** At the highest frequencies, the behavior of the reflector IRA on boresight is well-approximated by the optical approximations and aperture theory, with only minor oscillatory behavior from the reflected field interactions with the feed structure. This region might be defined from the upper limits of the mid-frequency region to whatever physical limitations begin to deteriorate antenna performance.

These discrete performance bands are a first effort at modeling the reflector IRA behavior as a function of physical dimensions, but are likely to be useful only for those seeking an antenna to operate in the low-frequency limits, as more suitable antennas are easily found for the higher frequencies. Because the antenna seems to be dominated by a dipole-like behavior at the lowest frequencies, it may be interesting to

adjust the length of the feed arms to something greater than F, space allowing, to see if the lower limits can be pushed further. Multi-arm feed designs with narrower arms would facilitate a lengthening of the arms without further increasing the abruptness of the geometry at the matching circuit.

4.4.2   TDR Analysis.

The next topic of discussion addresses the use of the TDR analysis in assessing reflector IRA performance. For locating and fixing discontinuities and impedance mismatches in transmission line, the TDR is undoubtedly the right tool for the job. Both the splitter balun (which was not simulated) and the transitions from coaxial cable to the coplanar plate feed are well described as transmission line junctions. The feed structure itself is designed as a spherical transmission line, and the ability to measure and design the characteristic impedance of the feed using a TDR analysis was fully demonstrated in this thesis. Beyond this point, however, analysis of the TDR response becomes a task of questionable utility as the reflector IRA as a system is an antenna and not a transmission line. A TDR can be made to display the response of a device under test in terms of impedance, but it is not an impedance-measuring device. Rather, it typically measures a voltage as a function of time, which can (for a transmission line) be related to the discontinuity or impedance mismatch that would have caused a reflected voltage of the amplitude and polarity measured by the device. Therefore, when the TDR response of a reflector IRA is analyzed, particularly in the time region when reflections would be expected from the end of the feed arm, to characterize the behavior as a "dip in the impedance" or a "capacitive effect" is simply not justified. Most researchers who work on the reflector IRA are well aware of the reflected fields and their interaction on the feed structure, indeed noting that the reflected field will arrive at the feed point at the

same time as the current reflected from the end of the feed arm [6, 9], yet still treat the TDR response as if analyzing a transmission line. It is indeed a coupling of the reflected fields with the feed arms, and the resulting induced currents, that manifest as a large dip on the TDR. This is purely defined by the geometry of the feed and no variation in the matching circuit will have a significant effect on this initial dip. Otherwise, if the dip is decreased but the feed geometry hasn't been modified, this may actually be an undesirable outcome, as it would indicate a weakening of the reflected field and possibly a decrease in the peak impulse response. There is an example study where exactly this scenario took place. In [9], one experiment involved covering the matching circuit of the feed arm with absorbent foam. The initial dip on the TDR response was increased, and the modification was abandoned "[d]ue to the poor TDR", so a full impulse response measurement was never made. It has been demonstrated in this thesis that matching circuit modifications can have dramatic effects on the appearance of the TDR response, but with negligible effects on the impulse response of the antenna. This further calls into question the utility of attempting to "flatten the TDR response", especially when trying to optimize the impulse-radiating performance of the antenna. At least for the work demonstrated here, we are willing to accept what may be deemed a poor TDR response as a trade for increased performance at low frequencies.

4.4.3 Simulation Validity.

Finally, many of the results of the thesis and even much of the discussion on TDR analysis hinge on the behavior of the matching circuit in the simulation model. It must be stated that this is the one area where confidence in the agreement between simulation and reality is lowest. However, there are several items to consider in making an appropriate judgment on the validity of the simulations. First, we have

good agreement between two different solvers using different meshing techniques. The representation of the PEC wires in each of the meshes was slightly different, but the observed behaviors were nearly identical. In the time domain solver, the PEC wires are forced to meander along the orthogonal grid lines; in the tetrahedral mesh of the frequency solver the wires are represented by exact conformal mesh lines. The $\lambda/60$ spacing used for the time domain solver should eliminate most of the concerns up to the highest frequencies, but the reality is unknown because the FD solver was adapted for S-parameter convergence only up to 2 GHz typically and a one-to-one comparison is unavailable at the high frequencies where the backlobes dominate. Regardless, the low-frequency behaviors match between the two solvers. Secondly, there is a possibility that matching circuits in the simulation models are more effective than in reality. The models were defined with a perfect electrical connection and smooth geometry, especially with regard to the inner resistor chain matching the β_1 angle of the arm. The reality of a realized reflector IRA is of wires that are soldered or screwed down, which may represent an increase in the "geometric" discontinuity at the matching circuit. Finally, we have now some simulated metrics that should be fairly easy to obtain in measurement, namely TDR and VSWR as they relate to various resistor values. Whether the trends identified in simulation match the reality will be quickly discovered for these metrics even without a full antenna characterization. And indeed, if the real matching circuit of the reflector IRA is as ineffective at high frequencies as the simulation models suggest, then the existence of the newly-identified backlobes should be readily seen on an antenna range. So, the full validity of the simulated experiments remains to be seen, but once antennas are built for experimentation, it should be quick work to make a determination on the matter.

4.5   Chapter Summary

In this chapter the key results of the thesis were described in detail. First, two standard reflector IRA designs were simulated and characterized with time- and frequency-domain metrics. The simulation models were built to match the reality of a constructed reflector IRA as closely as possible, especially with regard to the matching circuit layout. The simulation characterization reinforced some ideas that have been previously demonstrated through theory and measurement, namely the improvements seen in the $\phi_0 = 60°$ design over the $\phi_0 = 45°$ legacy design. The detailed analysis also reveals that the matching circuit may not be as effective at suppressing currents as previously assumed; instead, the reflector IRA radiates nearly 40% of the stimulated power into the rear hemisphere in four large back lobes aligned outside the primary measurement planes of the antenna. Next, and as part of the investigation to improve the low-frequency performance, novel multi-arm feed structures were designed that retain a characteristic impedance of $Z_{feed} = 200\Omega$ but bring some additional benefits. These benefits include reduced arm widths, and possibly more ideal field distributions for increasing the impulse-radiating performance of the antenna. For this work, however, it was demonstrated only that a third pair of arms in the feed structure introduced a new and viable option for tuning low-frequency performance of the reflector IRA. Additionally, various modifications to the resistor values in the matching circuit reveal a fairly large tradespace in which the low-frequency performance of the antenna may be enhanced and tuned. Basic guidelines for predicting reflector IRA performance as a low-frequency antenna were also introduced, and applying this model to the NRTF antennas suggest that it is sized nearly ideally for the desired frequencies of operation. A more complete analysis is performed in Appendix A.

V. Conclusion

5.1 Chapter Overview

The research performed for this thesis was intended to support the use of the reflector IRA in a new role as a compact low-frequency antenna with good directional radiation characteristics and, more importantly, a reduced late-time response. As a result of the research, we conclude that the reflector IRA design may be adapted and suitable for application to both the AFIT noise radar and in RCS measurements at VHF frequencies. In the process of coming to this conclusion some additional insights were gained on the nuances of reflector IRA performance. In this chapter, the methodology used for the research will be briefly reviewed, as will the key results and contributions. While some of the detailed investigations may seem exhaustive (and left the author exhausted), many questions were left unanswered. Some ideas for continuing to flesh out the unknowns are presented as possibilities for future work.

5.2 Review of Methodology

The research was performed entirely in simulation, using the commercial CEM software of CST Microwave Studio. To ensure that the simulation results could be used with confidence in the absence of physical measurements, significant effort was put into understanding the capabilities and limitations of the CEM tools. Considerations for the simulation settings and construction of the model antenna were explored in detail, resulting in a framework geared primarily toward generating accurate results. A build-up approach was used to develop confidence in the model behavior and to verify performance with theory and measurements where possible. First, various iterations of a single pair of feed arms, or coplanar plate transmission line, were simulated, analyzed, and found to agree very closely with the theoretical models. The

two-arm feed structure common to the realized reflector IRA was also simulated in various configurations and found to agree with theory, where theory was available. The simulated performance of a full reflector IRA modeled on a commercial design was compared to the published data, and found to be in close agreement in many respects. This provided confidence in the simulation models as well as a verification of the data processing technique used to extract some time-domain performance parameters. Finally, with the simulation framework in place, new ground was set to be broken by exploring and characterizing standard and modified reflector IRA designs. The modifications were intended to enhance the low-frequency performance of the antenna, and focused primarily on two aspects of the antenna design: feed arm and matching circuit configuration. Novel multi-arm feeds were developed in simulation and the capabilities of the CEM tools were leveraged to explore the effects of varying the resistor values in ways that would be difficult or impossible to do in the lab.

5.3 Results and Contributions

The original goals to fully characterize the reflector IRA by way of high fidelity computational models and the use of time- and frequency-domain metrics were fully satsfied. In characterizing the standard reflector IRA designs and the effects of various modifications, several key results were obtained that will benefit both the impulse-radiating community and those interested in applying the reflector IRA design as a low-frequency antenna as intended here.

- Large backlobes were identified that have previously been unknown. These lobes appear to be the result of radiation from the ends of the feed arms where the matching circuit is ineffective at suppressing high frequency currents. For the current reflector IRA designs, it is estimated that as much as 40% of the stimulated power is radiated into the rear hemisphere, primarily in these lobes.

The lobes are aligned at approximately 45° between the primary E- and H-planes of the antenna, which may explain why they have never before been identified.

- Novel feed structures with additional arms were designed for the standard 200 Ω feed impedance. Instead of considering exotic shapes and geometries, these feed arms conform to the standard design for conical symmetry, making them easier to construct and measure. A design with three pairs of arms was demonstrated to improve low-frequency performance, but strong coupling between the vertical pair of arms and the reflected fields reduced the predicted peak impulse response slightly. A feed with four pairs of arms may avoid this coupling while simultaneously improving the field distribution on the reflector, resulting in an increased peak impulse response.

- Modifications to the resistor values on both the standard reflector IRA design and the novel 3FA design were shown to be viable options for tuning the low-frequency performance of the antenna. Additionally, these modifications were shown to have a negligible impact on the boresight impulse-radiating performance of the antenna, primarily due to the aforementioned ineffectiveness of the matching circuit at high frequencies. We expected to see a tradeoff between time- and frequency-domain performance, but for the boresight direction of the reflector IRA, the high frequencies dominate and the tuning effects at the lowest frequencies are insignificant overall.

- A basic analytical model was created to help size the reflector IRA design and predict the bandwidth performance as a low-frequency antenna with a single main beam. The low frequency limit is related to the focal distance of the paraboloidal reflector for typical reflector designs.

These key results will help guide the construction and measurement of antennas for application to the AFIT noise radar, where a low-ringing antenna is expected to enhance nearly every noise radar application and may introduce new capabilities such as transient RF-DNA fingerprinting. The characterization of the reflector IRA constructed for the NRTF provides a predicted performance assessment that was previously unavailable, shows that at the frequencies of interest they are unaffected any significant radiation lobes other than the wide main beam, so the antenna may be safely used as intended. Additionally, because the options identified for low-frequency performance enhancement are so simple, retrofitting the existing antennas is a reasonable option.

5.4   Future Work

A purely theoretical antenna or one that exists only in simulation is absolutely useless in the real world. As such, the primary future effort for this work must be to build and measure the simulated antennas. Measurement will serve to verify or disprove some of the claims made based on simulation results, but more importantly, the capabilities of the AFIT noise radar system stand to be further enabled by a proper UWB antenna with low ringing. There are some additional details that may be considered in simulation to aid in antenna construction, such as detailed modeling and design of the splitter balun and the feed transition at the apex of the reflector IRA, but the bulk of the design details are in place.

Appendix A. NRTF Reflector IRA Predictions and Analysis

One of the motivating applications for the reflector IRA discussed in Chapter I is that of RCS measurement in the VHF band. The NRTF has begun using 12-foot reflector IRAs in this application, but due to the experimental nature of the reflector IRA and challenge of obtaining detailed 3D measurements of large VHF antennas, many performance characteristics are unknown. Computational techniques are employed to predict the performance of the as-built antennas, as well as two retrofit options with modified resistor values.

A.1   Model and Methodology

The 12-foot reflector IRA shown in Figure 1.2 and Figure A.1 was simulated using the methodology of Chapter III, except the simulation bandwidth was limited to 1 GHz instead of 20 GHz. This compromise was done to ensure accurate results for the frequencies of interest (30-120 MHz) and enough bandwidth for a meaningful impulse response calculation while maintaining a feasible computational domain size. The simulation model was created using technical documentation used for physical assembly, along with some additional physical measurements and a detailed description of the resistor layout. The complexity of the matching circuit is the major difference between this antenna and all other reflector IRA variants simulated in the thesis. As shown in Figure A.1, the matching circuit is composed of two parallel resistor chains at each edge of the feed arm, for a total of four resistor chains. Each chain has 10 resistors with alternating low-high values, and the total resistance as currently configured is an approximate match to the intended $Z_{feed} = 200\Omega$ feed arms. The potential to tune the antenna performance at low frequencies was demonstrated in the main thesis work. Here, two additional scenarios are modeled to demonstrate this capability in a simple retrofit configuration, wherein the total resistance is increased by 50%
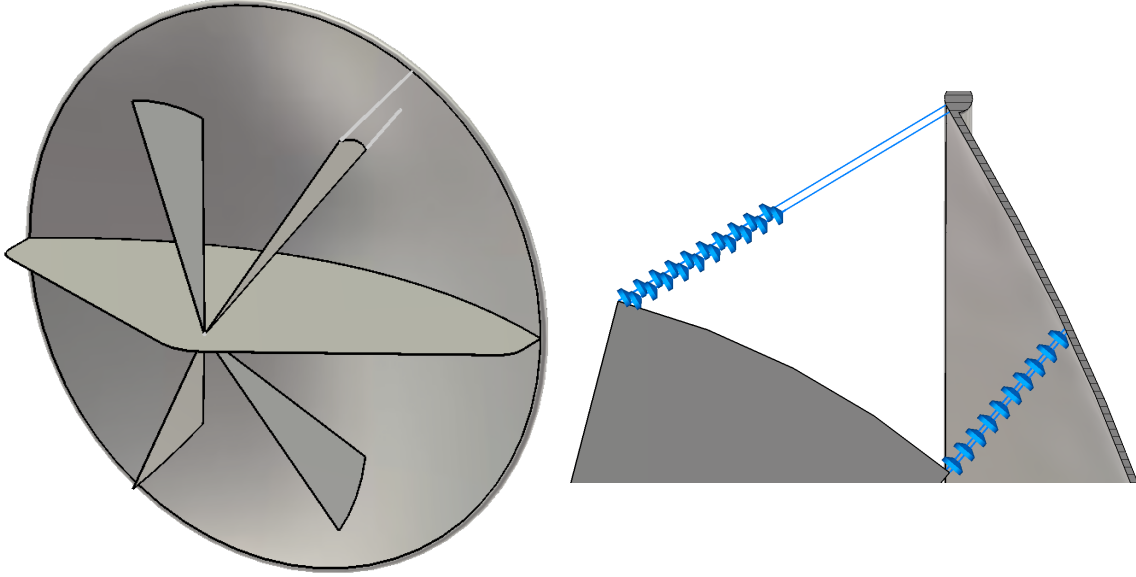
Figure A.1. Simulation model and resistor detail for the NRTF 12-foot reflector IRA.

and decreased by 50% relative to the as-built resistor values. As such, the results are labeled according to the resistance scale factor: the as-built antenna results are labeled as $k_{tot} = 1$, and the increase and decrease are labeled $k_{tot} = 1.5$ and $k_{tot} = 0.5$ respectively.

A.2   Results and Analysis

As with the other simulation models, the predicted performance of the 12-foot reflector IRA is characterized by high resistive losses and low gain at the lowest frequencies. Modifying the resistor values away from a perfect match increases reflections (Figure A.2) and reduces power losses in the resistors (Figure A.3) at the low end. An interesting resonance introduced for the $k_{tot} = 0.5$ case, noted at about 85 MHz in the S_{11} parameter and VSWR, manifests only as increased power loss and not as increased radiation (Figure A.4).

Application of the simple model introduced in Chapter IV suggests the following general boundaries for the low-frequency performance based on the reflector dimen-

sions:

- Lower inflection point, where the focus-to-rim distance (81.6 inches) equals $\lambda/4$ is approximately 36 MHz;

- Good performance begins where the focal distance (60 inches), $F = \lambda/4$ at approximately 49 MHz;

- Performance leveling just before sidelobes begin to form, where $F = \lambda/2$ is approximately 98 MHz;

- First major sidelobes are realized by $F = 3\lambda/4$ at 148 MHz.

Therefore, we should expect an increase in total resistance to improve performance above 36 MHz and a decrease in total resistance to improve performance below. Indeed the simulations show that the $k_{tot} = 0.5$ case has the least resistive losses (Figure A.3), the best efficiency (Figure A.4 and Figure A.5), and highest boresight gain (Figure A.6) below approximately 50 MHz. However, this improved performance comes at a price that is paid across the entire bandwidth of interest, namely in the directivity (Figure A.7). The radiation is no longer confined primarily on boresight, and this is manifest in the front-to-back ratio (Figure A.8), increased beam widths (Figure A.9) and sidelobe levels (Figure A.10).

For the increased resistance case of $k_{tot} = 1.5$, the model prediction of the lower inflection point appears to be correct; the boresight gain is fixed at approximately 36 MHz with reduced performance below, and increased performance above (Figure A.6). As opposed to the reduced resistance case, however, increasing the resistance is predicted to result in significant improvements over most of the desired operating frequencies. Above 50 MHz, the $k_{tot} = 1.5$ configuration has the lowest power losses (Figure A.3) and highest efficiencies (Figures A.4 and A.5). The gain (Figure A.6) and directivity (Figure A.7) are increased; the front-to-back ratio and cross-polarization rejection are improved (Figure A.8), the beamwidths are narrowed (Figure A.9) and the sidelobes are reduced (Figure A.10). Some of these improve-

ments are quite dramatic over the predicted performance for the as-built antenna. All of the trends can be seen at a glance in the E- and H-Plane gain patterns, which are presented both in absolute terms (Figures A.11 and A.12) and normalized to the main beam (Figures A.13 and A.14).

In the time domain, the impulse response and transfer functions (Figures A.15 and A.16) continue to indicate that the tuning value in the matching circuit is primarily limited to the low-frequency region of operation. The peak value of the impulse response is in the same order of magnitude as other reflector IRAs that have been modeled; the effect of increasing the physical dimensions is manifest on the time scale, where the pulse width and ringing are now measured in nanoseconds instead of picoseconds. The key results are presented in Table A.1. It is particularly interesting to note that the massive 12-foot reflector IRA still maintains a time response and ringing duration shorter than that of the 12-inch log-periodic of the AFIT noise radar (compare Table B.1).

A.3   Conclusion and Recommendations

The as-built 12-foot reflector IRA appears to have reasonable performance in the intended frequencies (30-120 MHz), especially given the reduced ringing afforded by the design. The first true sidelobes appear at or above 120 MHz, so increasing the operating frequency is not recommended. A general improvement in antenna performance may be achieved by fitting increased resistance matching circuit elements. Reducing the resistance may increase the boresight gain below 50 MHz, but will generally decrease the performance with regards to directivity, beamwidths, sidelobes and cross-polarization rejection. A larger effort to refit the antenna with a multi-arm feed may improve performance at the lowest frequencies without the negative performance effects associated with decreasing the resistance.
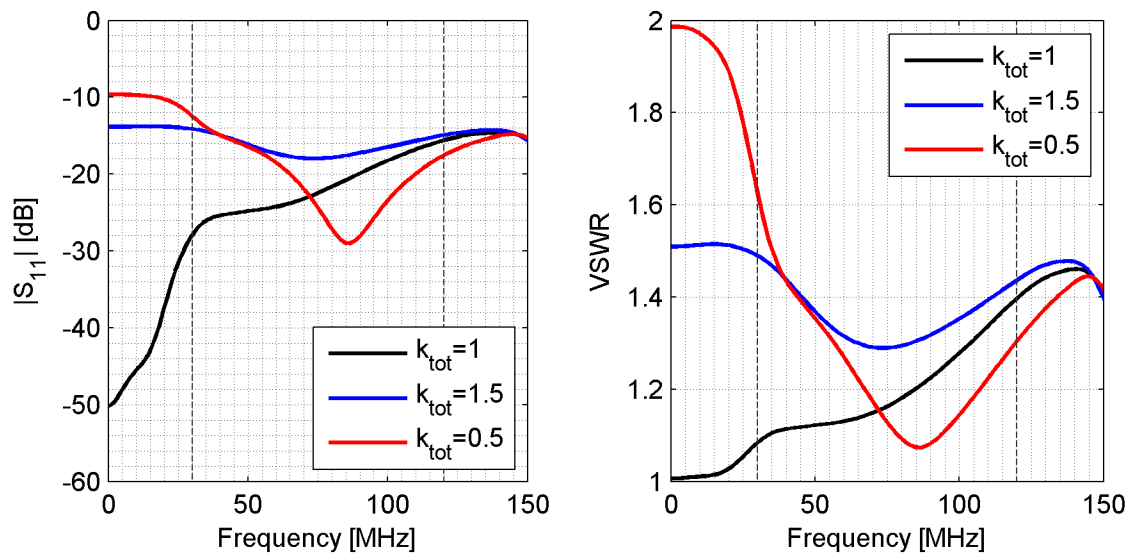
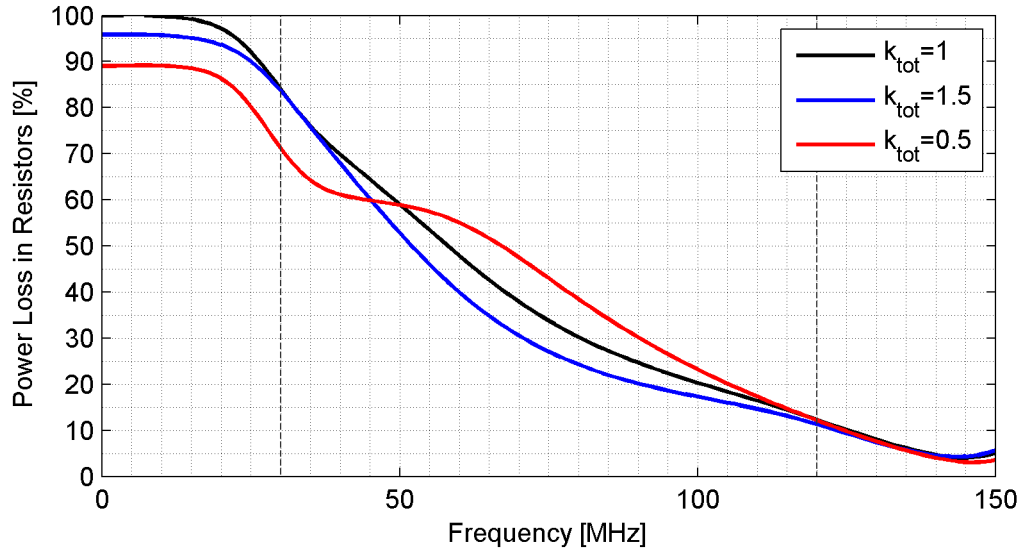**Figure A.2.** $|S_{11}|$ and VSWR of the NRTF IRA.
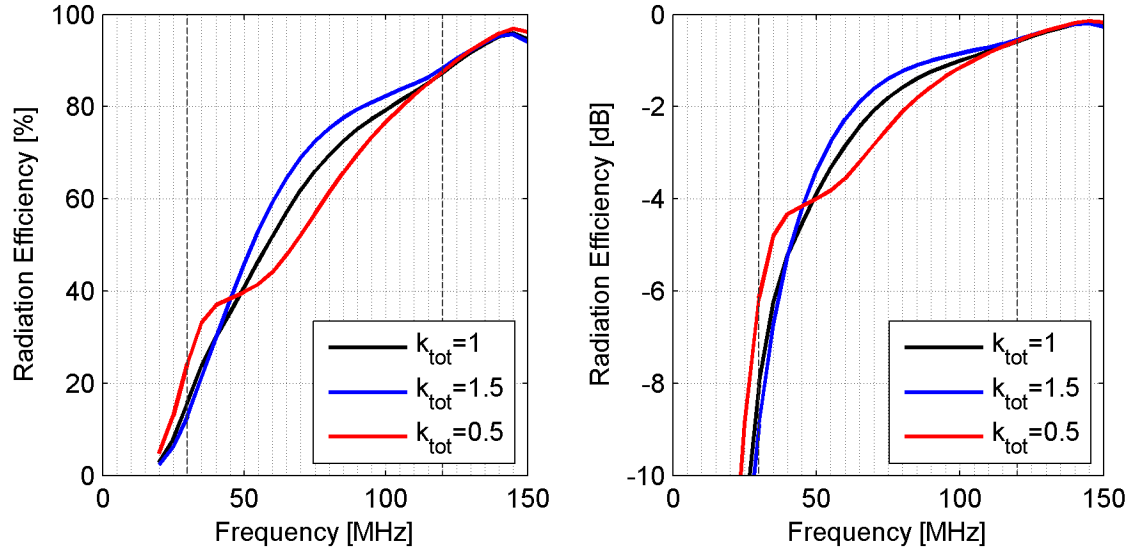

Figure A.3. Power loss in resistive elements.

Figure A.4. Radiation efficiency in percentage and decibel scales. Radiation efficiency is the ratio of the power radiated to the power accepted.
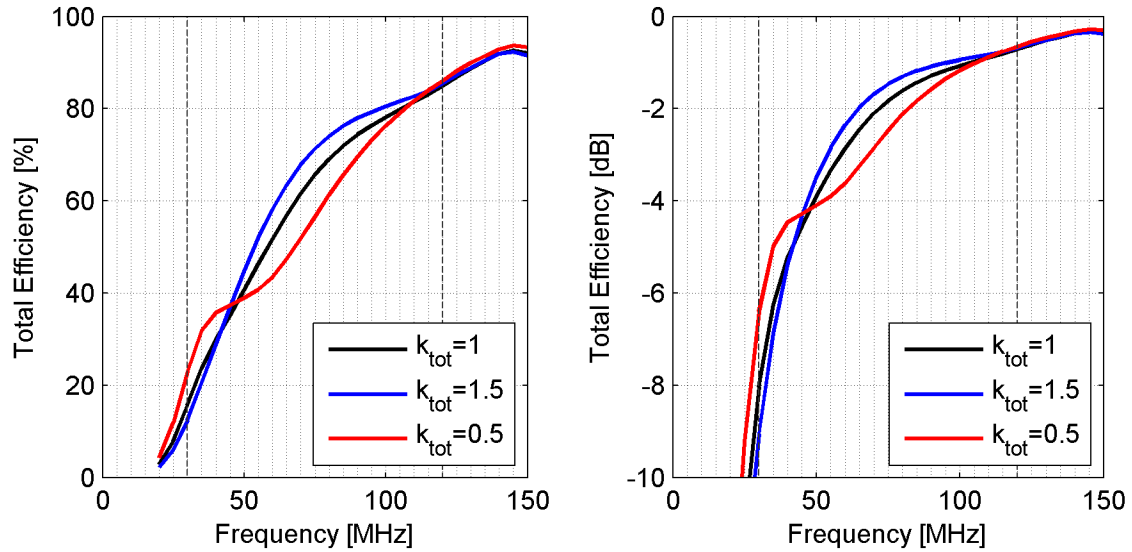

Figure A.5. Total efficiency in percentage and decibel scales. Total efficiency is the ratio of the power radiated to the power stimulated.
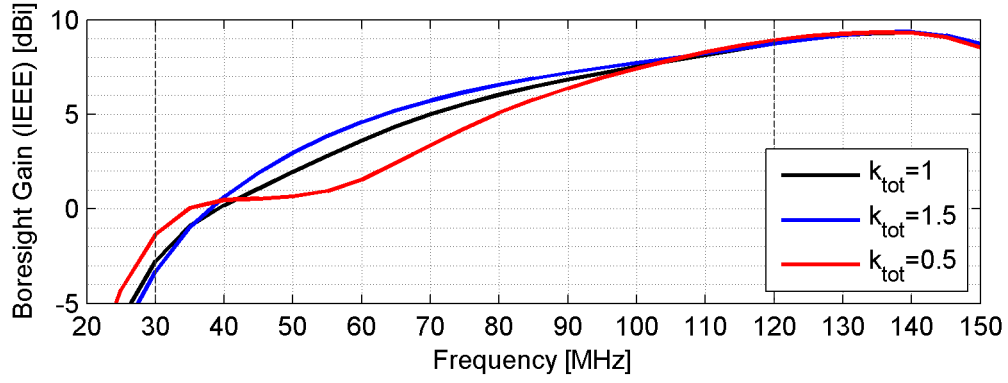
Figure A.6. Boresight gain.
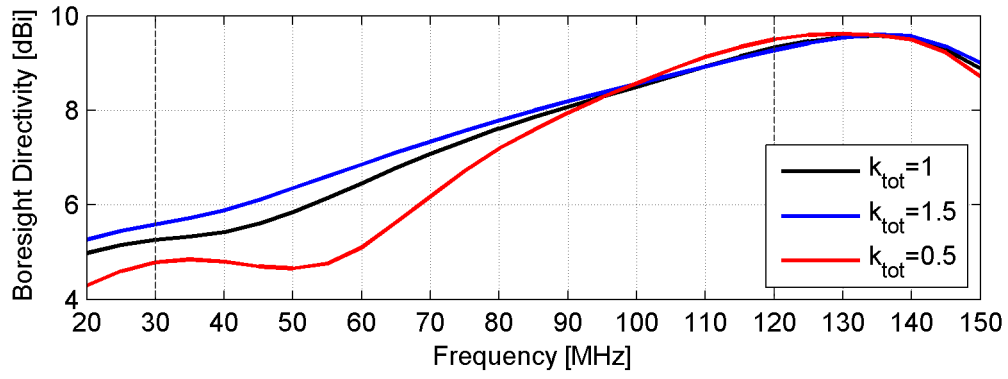
Figure A.7. Boresight directivity.
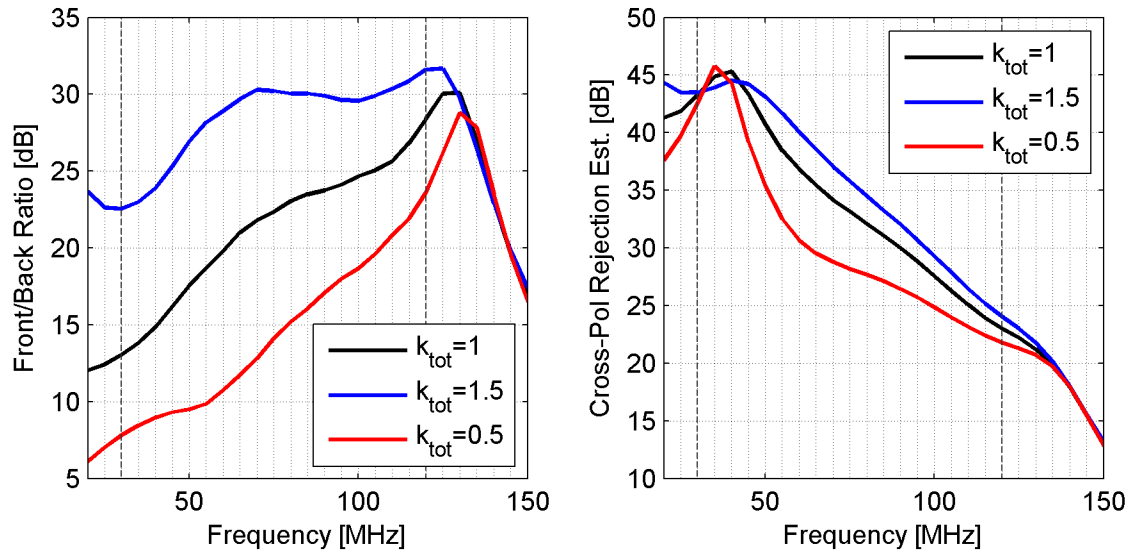
Figure A.8. Front-to-back ratio and cross-polarization rejection estimates. High values are desirable for both metrics.
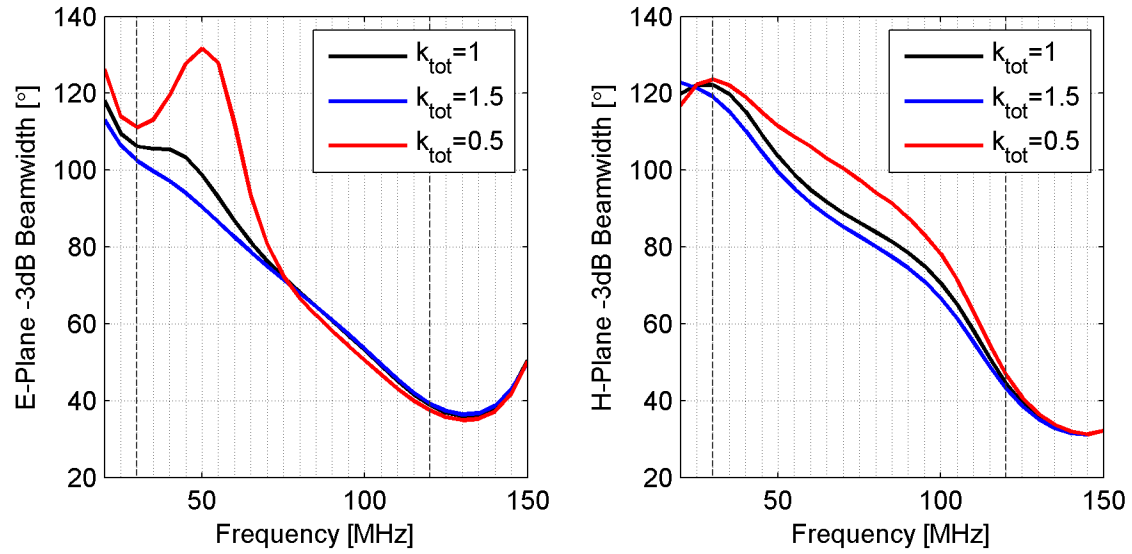
Figure A.9. Half-power beamwidths.
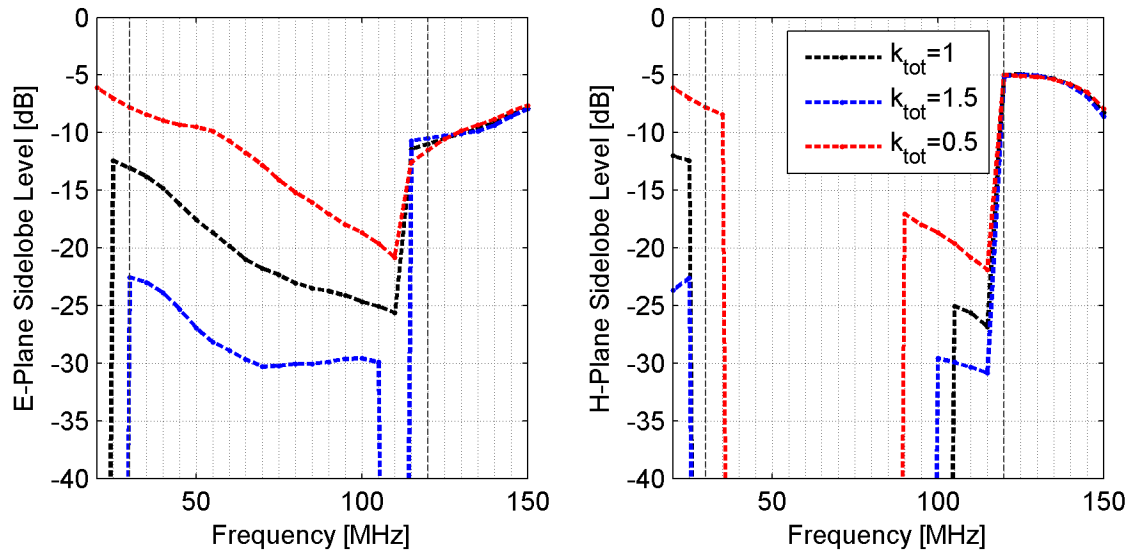
Figure A.10. Sidelobe levels. Below 120 MHz, the sidelobe level noted is typically a small backlobe in the cardioid pattern; the first primary nulls and sidelobes form at or above 120 MHz.
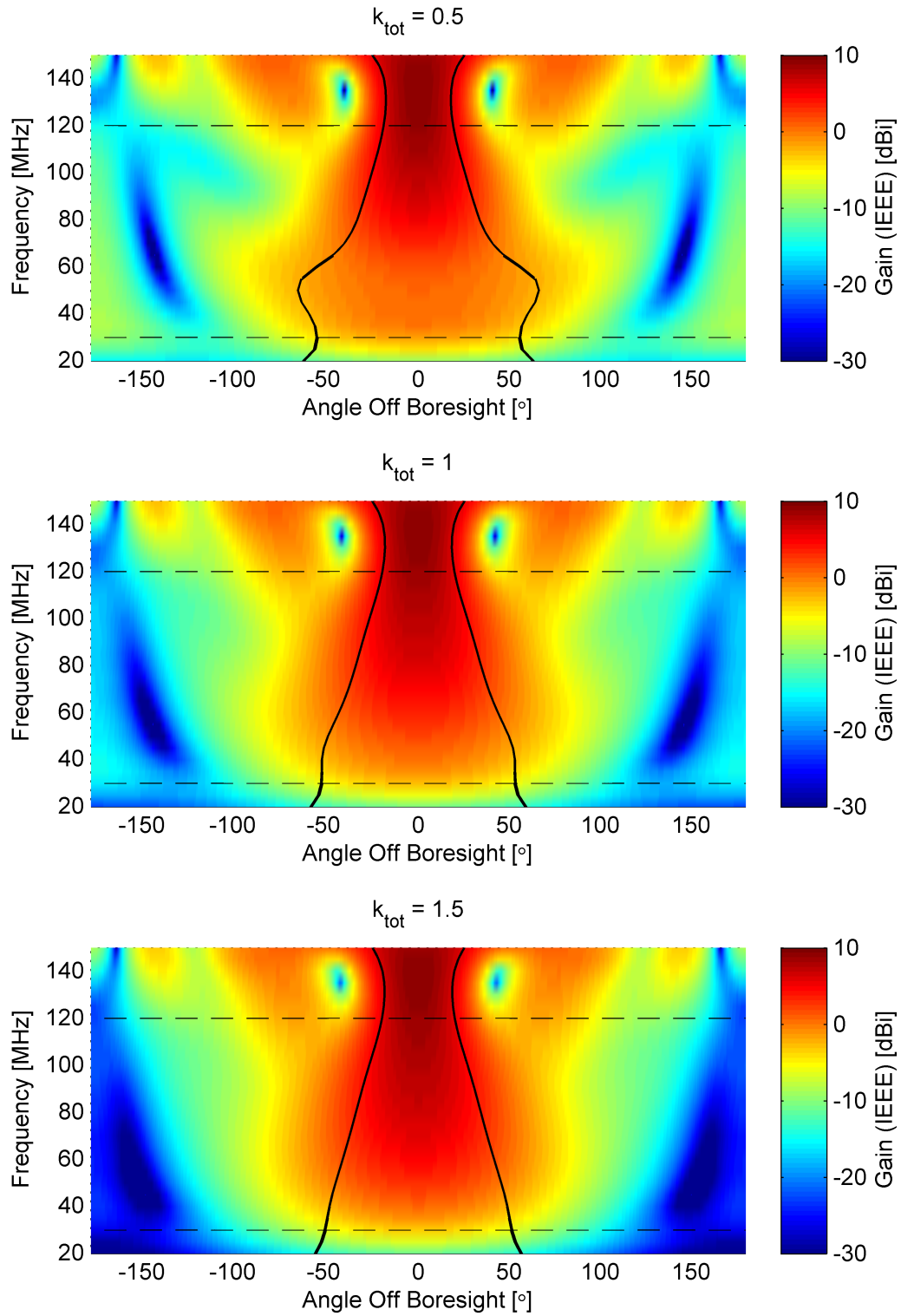
Figure A.11. E-Plane gain patterns. The -3 dB beamwidth is shown in solid and the frequencies of interest (30-120 MHz) are bounded by dashed lines.
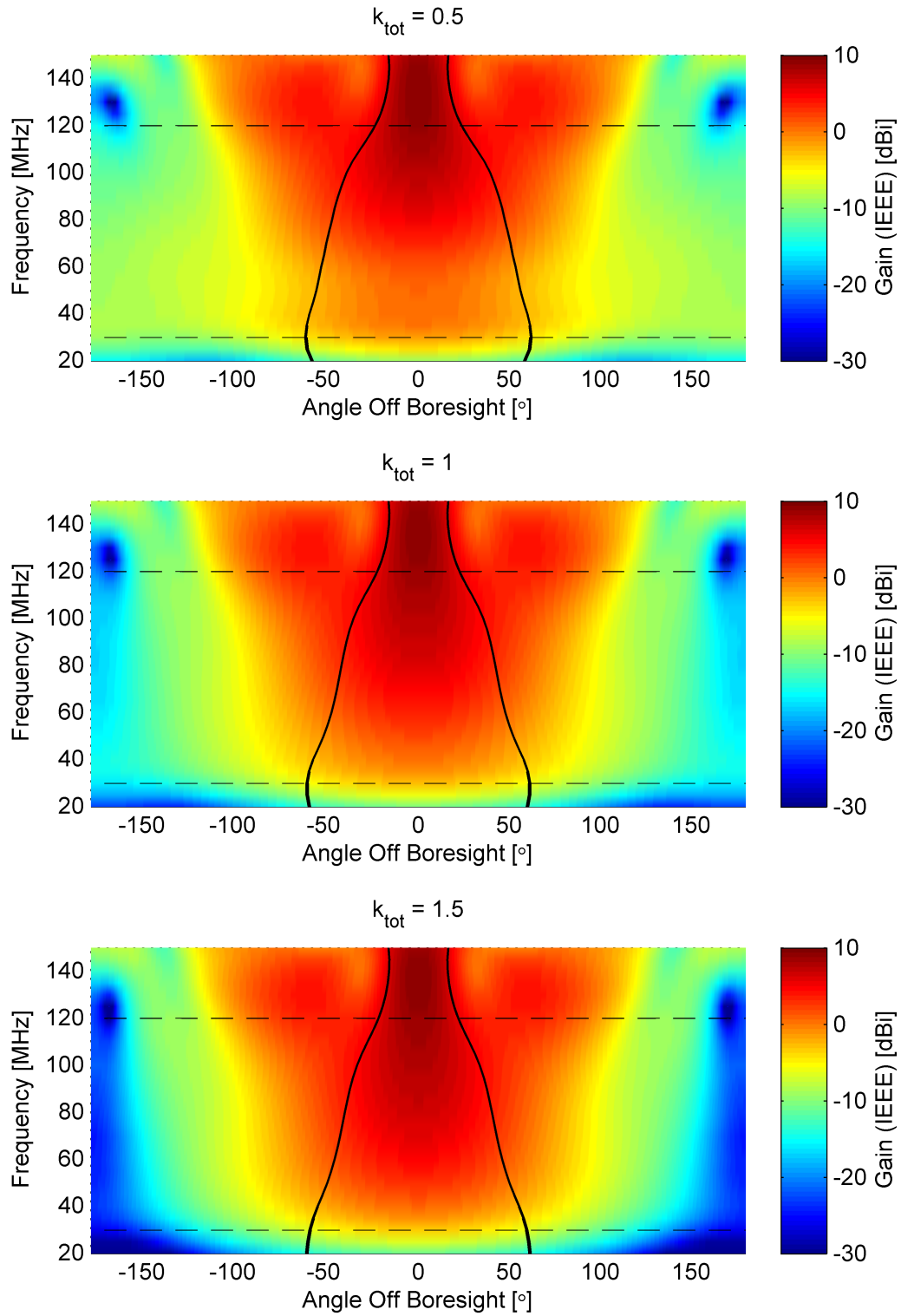
Figure A.12. H-Plane gain patterns. The -3 dB beamwidth is shown in solid and the frequencies of interest (30-120 MHz) are bounded by dashed lines.
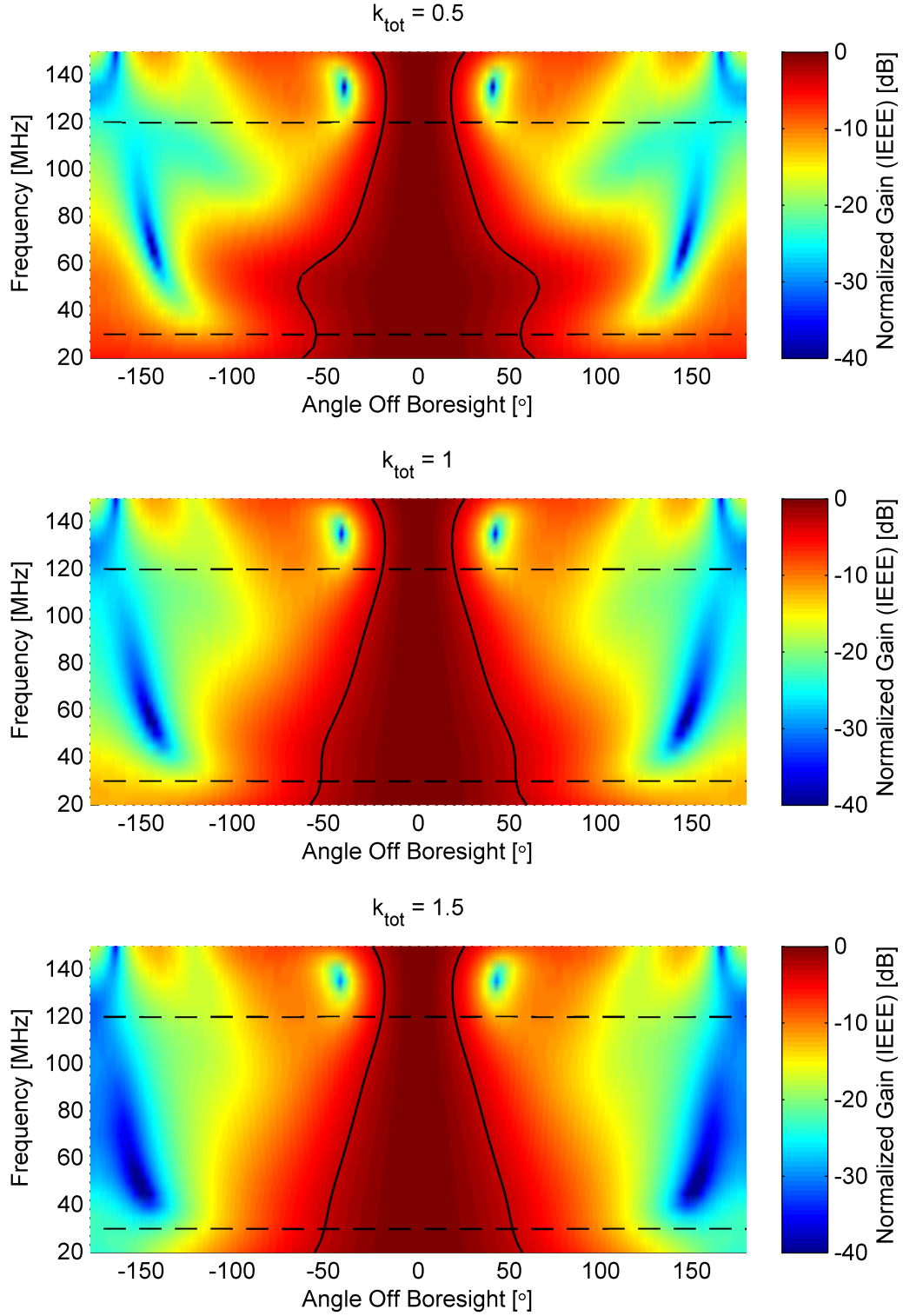
Figure A.13. E-Plane gain patterns normalized to the main beam value. The -3 dB beamwidth is shown in solid and the frequencies of interest (30-120 MHz) are bounded by dashed lines.
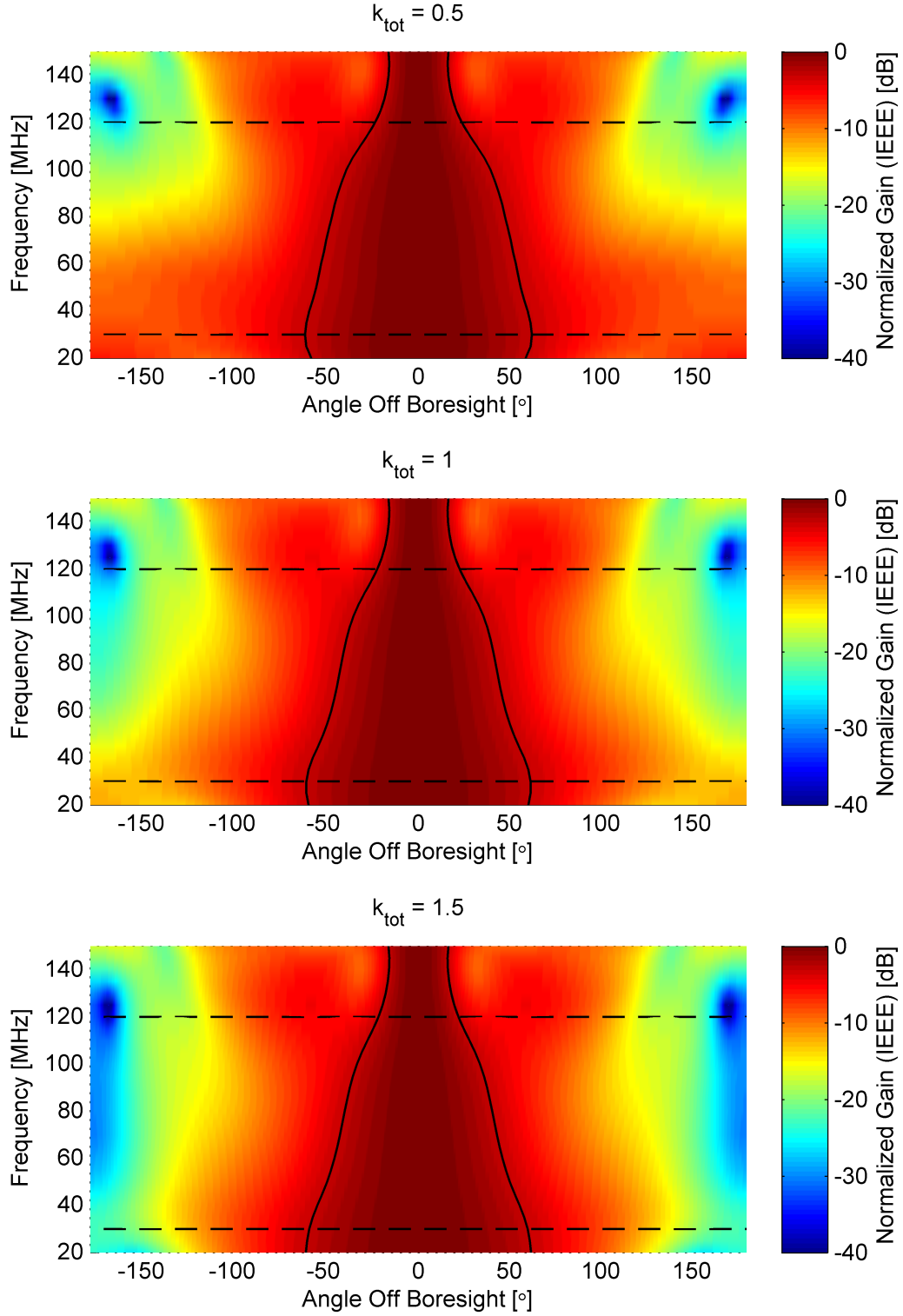
Figure A.14. **H-Plane gain patterns normalized to the main beam value. The -3 dB beamwidth is shown in solid and the frequencies of interest (30-120 MHz) are bounded by dashed lines.**
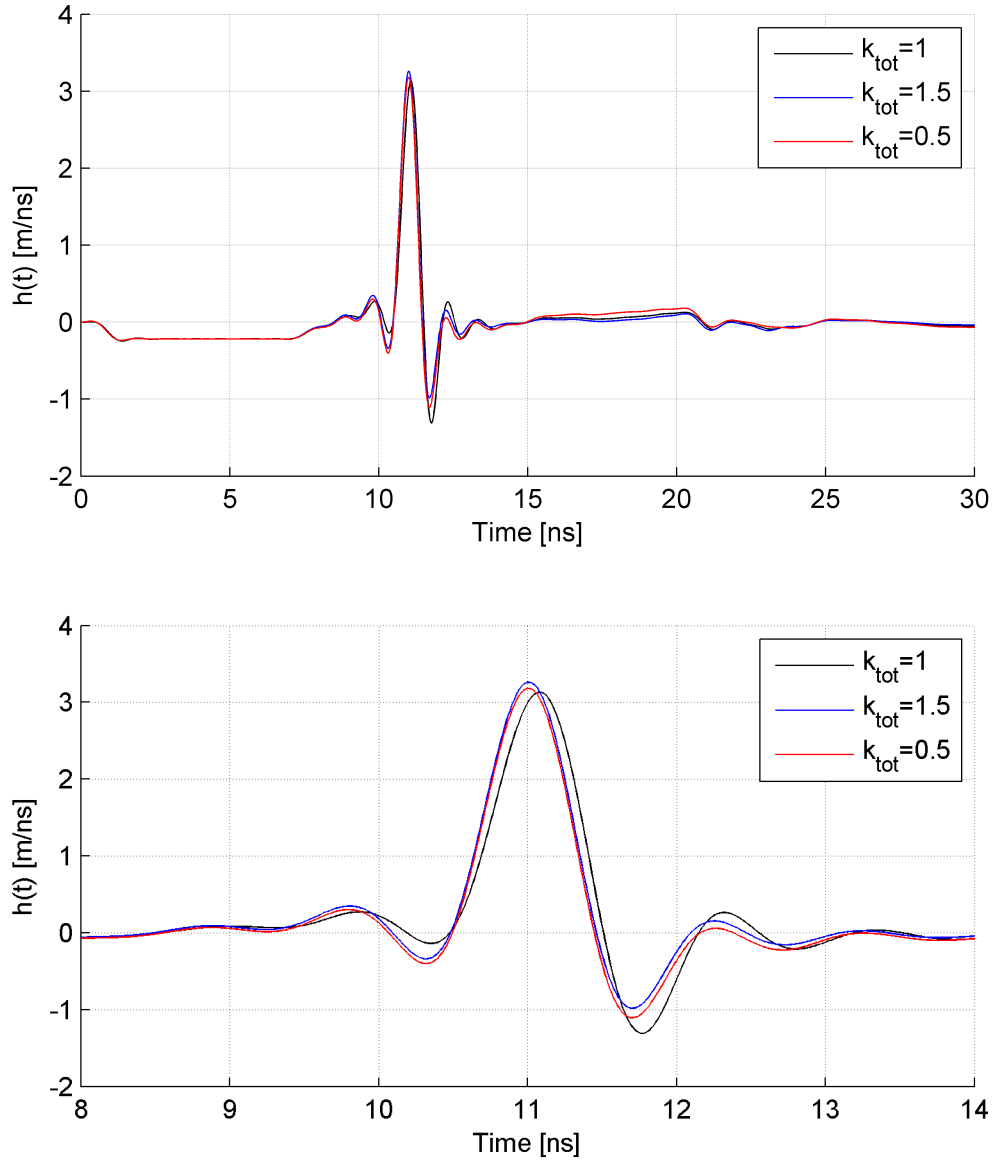
Figure A.15. Impulse response waveform, $h(t)$, for the boresight direction and dominant polarization. The impulse response is band-limited to 1 GHz.
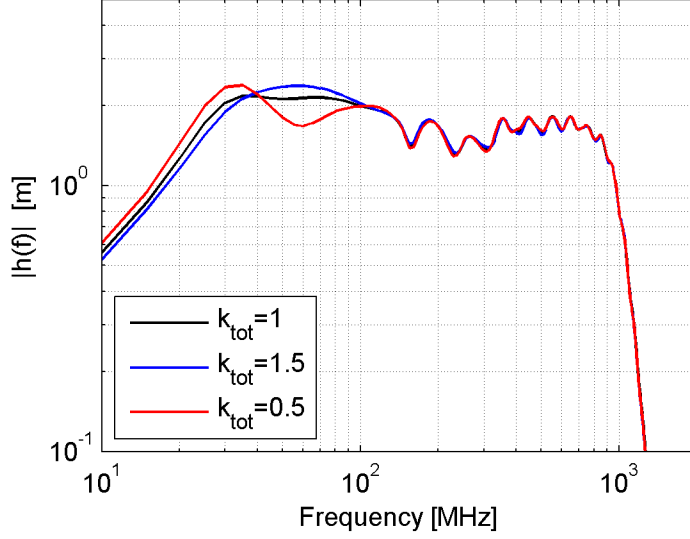
Figure A.16. Transfer function magnitude, $|\widetilde{h}|$, for the boresight direction and dominant polarization.

**Table A.1.** Time domain metrics of the NRTF 12-foot IRA. The impulse response is band-limited to 1 GHz, and the time scale for pulse width and ringing is nanoseconds instead of picoseconds. An additional ringing measurement point to 5% is introduced that incorporates the low-level late time response seen in Figure A.15.

		$k_{tot} = 1$	$k_{tot} = 1.5$	$k_{tot} = 0.5$
Peak $h(t)$	[m/ns]	3.13	3.26	3.18
Peak $|h^+(t)|$	[m/ns]	3.20	3.28	3.20
FWHM $h(t)$	[ns]	0.587	0.576	0.566
FWHM $|h^+(t)|$	[ns]	1.204	1.161	1.188
Ringing, $\tau_{r,0.22}$	[ns]	0.818	0.804	0.835
Ringing, $\tau_{r,0.10}$	[ns]	1.574	1.564	0.962
Ringing, $\tau_{r,0.05}$	[ns]	9.996	10.025	10.125

Appendix B. Utility Assessment for AFIT Noise Radar

The simulated performance of the 12-inch, $\phi_0 = 60°$ reflector IRA is compared to that of the current AFIT noise radar antenna to assess the overall potential for performance improvements. The log-periodic antenna (Figure B.1) was simulated using the same methodology as the reflector IRA in order to generate data for comparison.
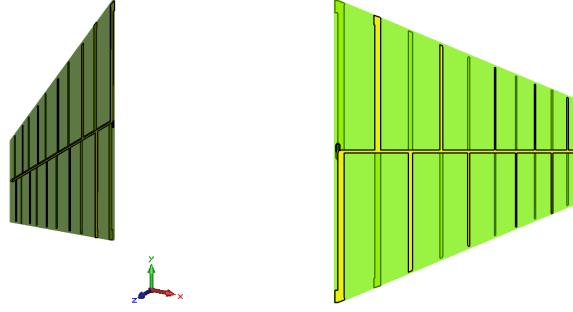
Figure B.1. Simulated log-periodic antenna for comparison to the reflector IRA.

B.1 Frequency Domain: Reflector IRA vs Log-Periodic

The log-periodic is a frequency domain antenna, so we begin the comparison there to highlight its relative strengths. The operating bandwidth of the AFIT noise radar is from approximately 300-750 MHz in two-channel mode; the hardware may support operations up to 1 GHz or slightly more, so the comparison between antennas is made primarily from 300-1000 MHz. The S_{11} and VSWR plots of Figure B.2 show that the log-periodic has low reflections throughout the stated operating band of 400-1000 MHz, but it is clearly characterized by the multiple resonances of the radiating elements. A comparison of the realized gain on boresight is shown in Figure B.3.

Note the use of realized gain instead of "standard" gain for this comparison; realized gain is referenced to the total stimulated power and accounts for reflections and impedance mismatch, while gain is referenced to only the accepted power. The
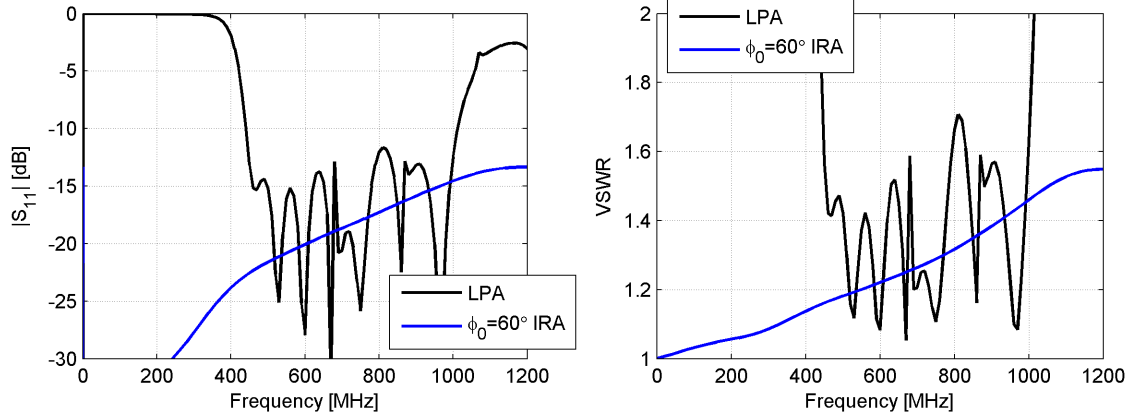
Figure B.2. Comparison of $|S_{11}|$ and VSWR of the log-periodic and reflector IRA. The reflector IRA has a smoother character than the log-periodic.
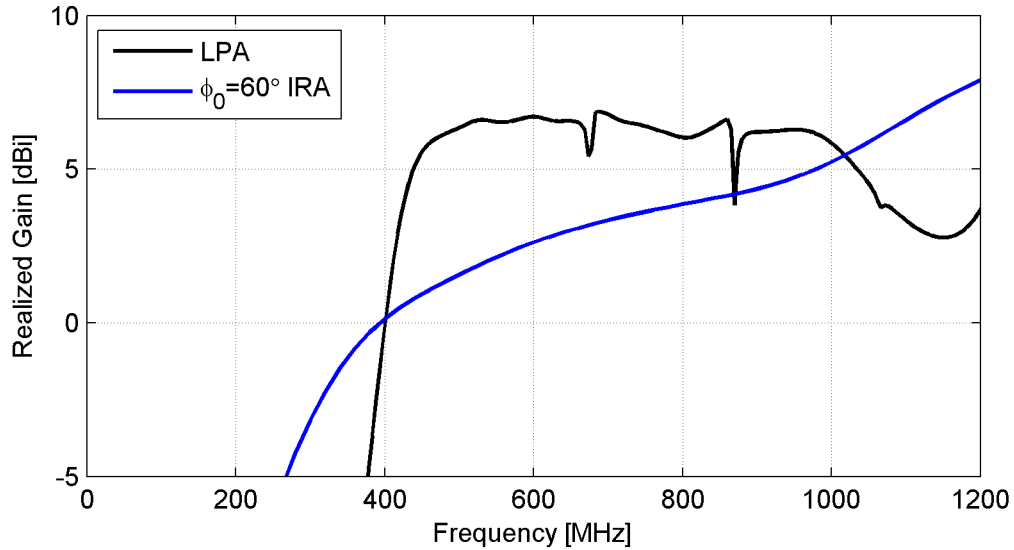
Figure B.3. Boresight realized gain of the log-periodic and reflector IRA.

log-periodic accepts very little power at 300 MHz, and this is important to note for the UWB operating mode. Regardless, the log-periodic is an efficient radiator across its stated operating band, as indicated by the consistent gain. The reflector IRA has lower gain, but it is worthwhile to note that *some* performance is achieved at 300 MHz, versus the relative lack of performance of the log-periodic at this frequency. Next, we consider the radiation in directions other than boresight. Realized gain is the norm for all remaining comparisons.
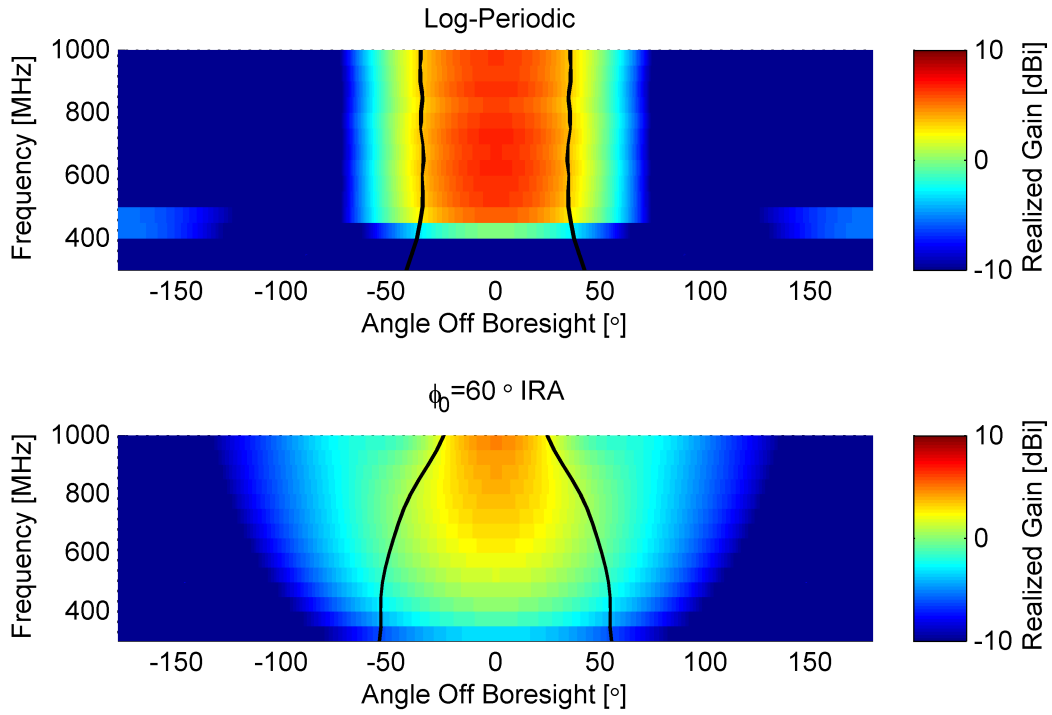
Figure B.4. E-Plane realized gain pattern vs frequency showing the -3 dB beamwidth.
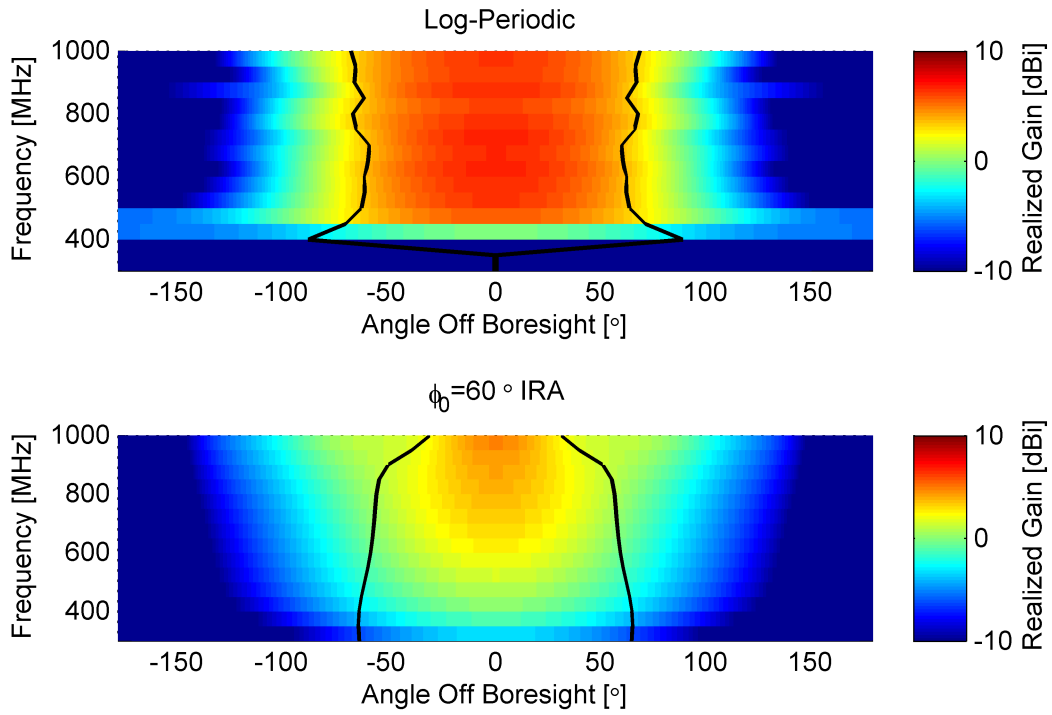
Figure B.5. H-Plane realized gain pattern vs frequency showing the -3 dB beamwidth.

In Figure B.4 and Figure B.5, a trace showing the -3dB beamwidth has been included to aid in the comparison between antenna characteristics. Similar to the boresight realized gain plot, the log-periodic appears to have a fairly consistent gain within the main beam as a function of frequency, and the beamwidths are also fairly steady with frequency. For both antennas, the H-Plane beamwidth is wider than the E-Plane beamwidth, but the difference in E- and H-Plane beamwidths for the reflector IRA is less pronounced. Also, the reflector IRA radiates essentially only in the forward hemisphere, while the log-periodic has some backlobes at the lower frequencies.

From the observations made up to this point, it is fair that the log-periodic might be chosen as the better of the two antennas based on its higher and more consistent gain across most of the bandwidth of interest. The radiation patterns don't indicate any big surprises, and the reflector IRA simply seems *okay* in comparison. For UWB operation, however, a comparison of the time domain characteristics is necessary.

B.2   Time Domain: Reflector IRA vs Log-Periodic

After comparing the log-periodic and reflector IRA for frequency domain characteristics, the log-periodic seems like the "winner". Now the time domain characteristics are compared for a full understanding of the antenna performance.

The boresight impulse response, $h(t)$, of the two antennas is shown in Figure B.6. The dramatic difference between the two antennas makes a graphical comparison difficult, but it is clear that the reflector IRA has a much higher peak and shorter duration than the log-periodic. A closer look at the log-periodic $h(t)$ alone is shown in Figure B.7, and a tabular listing of the key time-domain metrics is found in Table B.1.

From this comparison it is clear that the log-periodic antenna performs orders of

110
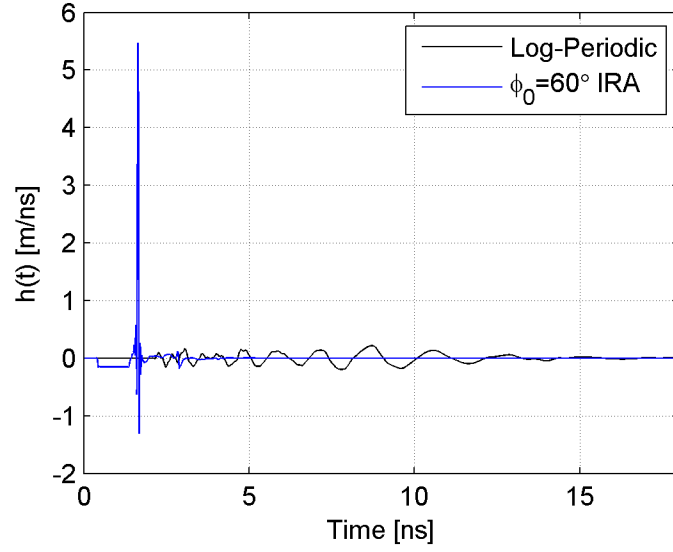
Figure B.6. Impulse response, $h(t)$, of the log-periodic and reflector IRA.
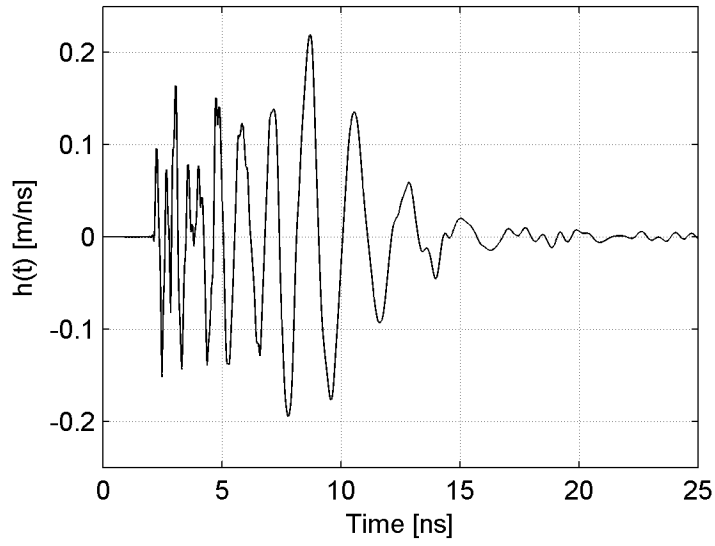
Figure B.7. A closer look at the impulse response of the log-periodic antenna. It is characterized by a wide response envelope and no clear peaks; the waveform shows a slowly decaying oscillatory behavior in the late time that continues for hundreds of nanoseconds (not shown).

Table B.1. Time domain metrics of the log-periodic and reflector IRA.

		Log-Periodic	IRA $\phi_0 = 60°$
Peak $h(t)$	[m/ns]	0.22	5.47
Peak $|h^+(t)|$	[m/ns]	0.24	5.49
FWHM $h(t)$	[ps]	561.4	29.1
FWHM $|h^+(t)|$	[ps]	8440	57.1
Ringing, $\tau_{r,0.22}$	[ps]	4318	39.3
Ringing, $\tau_{r,0.10}$	[ps]	5514	83.6

magnitude worse than the reflector IRA in time-domain or UWB pulsed operation. Given this contrast, the reduced gain performance of the reflector IRA may not be so bad after all.

B.3   Summary

The characteristics of the $\phi_0 = 60°$ standard reflector IRA and the current log-periodic antenna used with the AFIT noise radar were compared in the time- and frequency-domains. The reflector IRA was discovered to be slightly less capable than the log-periodic in frequency domain operation, but it dramatically outclassed the log-periodic in the time-domain, especially with regards to the ringing duration. This is a key area where performance improvement is desired for the AFIT noise radar system. Design changes to improve the gain of the reflector IRA may have the consequence of reducing the time-domain performance (possibly increased ringing), but because it is already so much better than that of the log-periodic, any trade-offs discovered will likely be deemed acceptable. We conclude that a 12-inch reflector IRA may be well-suited for application to the AFIT noise radar.

Appendix C. Comparison of Simulated and Measured IRA-3Q

The initial reason for simulating the Farr Fields IRA-3Q antenna was because published data on the time-domain performance of this antenna is available [1], along with enough details on its design and dimensions to make a fairly accurate model. The intent was to use it only for verification that the data processing techniques presented in Chapter III gave results that were the correct order of magnitude. The very close agreement in some portions of the spectrum compared with the larger differences seen especially at higher frequencies prompted a closer look to consider some of the reasons for the disparity.

C.1 Sources of Disagreement

In general, we can consider two primary sources of errors and inaccuracy in performing CEM work: disagreement between the simulation model and reality, and inaccuracies due to the simulation. In addition to these two main topics, it is also of interest to consider the measurement methodology used to characterize the actual antenna.

Disagreement Between Simulation Model and Reality.

Items discussed in this section are likely the primary sources of disparity between the simulated and measured IRA-3Q antennas.

- **Geometric Inaccuracies.** A complete schematic of the IRA-3Q is not available. The simulation models were built using only the stated diameter and F/D ratio of the reflector, the stated $\phi_0 = 60°$ design, and available relationships for designing the feed arms, along with estimated dimensions from photographs.

Additionally, the constructed model adheres to the theory as closely as possible and is constructed perfectly in that regard: the focal alignment of the feed is absolute, the paraboloid and feed arms are analytically perfect with no manufacturing irregularities, and defined symmetry planes guarantee ideal behavior in the boresight direction. For these reasons and more, it is clear that there could be quite large variations between the assumed geometry that was simulated and the actual antenna that was built.

- **Missing System Components.** Several items that may have affected actual antenna performance were not included in the simulation. These include the dielectric supports near the feed, the dielectric support and the metallic bracket at the end of the feed arms, mounting hardware and the splitter balun and coaxial cables that feed the antenna. The transmission line transitions at the balun and feed point are imperfect and have some reflections, as shown in Figure 2.4; it is possible that some resonances in the cables between the balun and feed degrade antenna performance.

Simulation Inaccuracies.

While a significant effort was placed on ensuring simulation accuracy for the primary thesis work, some additional compromises had to be made for the IRA-3Q model. The physical dimensions of the IRA-3Q are approximately 50% larger than those of the proposed 12-inch reflector IRA, but the simulation frequency settings remained the same. This resulted in the largest computational models that were attempted. The boundary conditions were modified so that the spacing around the antenna was reduced, nominally to $\lambda/4$ at 5 GHz, to help reduce the number of mesh cells in the computational domain. This is one possible source of simulation inaccuracy, but because the primary differences between the simulated and measured

IRA-3Q were seen above 5 GHz, this is not likely a significant contributor to the disparities. Additionally, some simulation experiments performed in the build up to thesis work suggested that the boundary conditions had a minimal impact on the antenna performance even at the lower frequencies, especially with the increased accuracy settings applied.

Measurement Methodology.

The most likely source of disparity between simulated and measured IRA-3Q discussed to this point is the fact that the constructed antenna and simulated antenna are not precisely the same. Asymmetries and imperfections in the realized antenna will most certainly have an effect on antenna performance that is not captured in a geometrically perfect simulation model. Because the primary discrepancies are in the high frequencies, it is additionally likely that the transition from coaxial cable to the coplanar plate feed structure is the source of much of the reduced performance seen in the actual antenna; the simulated feed is very precise and has a much smaller gap than is realistically possible to build. It is noted several times in Farr's work that feed point discontinuities reduce high frequency performance [9]. Another potential source for reduced high-frequency performance in the constructed antenna is in the measurement. Because the main beam becomes very narrow at high frequencies, any misalignments between the two measurement antennas will see a reduction in high-frequency content in the signals.

There is also some discrepancy between the simulated and measured performance at the lowest frequencies, where performance might be expected to be more stable against geometric imperfections. The source of this may also be attributable to the physical measurement methodology. The methodology is described in [1] and [9], wherein a time-domain antenna range is used to make wide frequency domain mea-

surements using narrow time pulses. These radiated pulses are generated by a small devices known as TEM sensors, which generate a nice impulse-like waveform at the early time but are not treated to reduce ringing, so all the data processing is performed on truncated or windowed time signals. Additionally, the TEM-1 sensor which was likely used to create the measured data is too small to have good low-frequency performance below approximately 1.5 GHz, and this is precisely one area where the simulated and measured transfer functions disagree slightly (see Figure 3.20).

C.2   Simulation Experiment

A simulation experiment was conducted to test out one hypothesis regarding the discrepancies. Instead of processing the impulse response for a geometrically perfect antenna perfectly on boresight, simulated field probes were placed slightly off boresight to simulate a measurement alignment error. The signals are recorded for the dominant polarization only, and the impulse response data was calculated using the methodology described in Chapter III. The probe names listed in Table C.1 are an indication of the placement; BS is the boresight probe, H_i is a probe in the H-Plane misaligned by i degrees, and the pattern follows for the E-Plane and the 45° diagonal plane for probes E_i and D_i respectively.

The data in the table clearly shows the dramatic effect small angular misalignments can have on the peak value of the impulse response. The H_2 probe results in properties that are very close to the measured data presented for the IRA-3Q, where the peak value of $h(t)$ was approximately 5 m/ns and the FWHM was 38 ps. The impulse response and transfer function for the boresight probe and the H_2 probe are plotted in Figure C.1 and Figure C.2, and the strong resemblance to the published measurement is again noted (compare Figures 3.22 and 3.20).

Though this was a simple experiment, it clearly demonstrates one potential source

Table C.1. Results of the measurement misalignment simulation experiment. The H_2 probe, which is misaligned by $2°$ in the **H-Plane** of the antenna, has very similar characteristics to the measured data for the **IRA-3Q.**

Probe	Peak $h(t)$ [m/ns]	FWHM $h(t)$ [ps]
BS	8.53	29.0
H_1	7.43	31.3
H_2	5.07	42.1
H_4	2.86	85.8
E_1	7.76	30.5
E_2	5.92	36.8
E_4	2.86	75.9
D_1	7.61	30.9
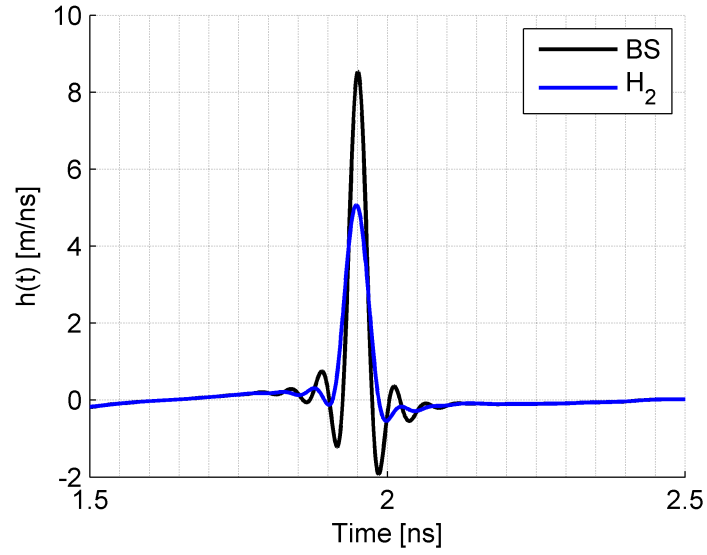
Figure C.1. Impulse response waveform, $h(t)$, for the boresight and H_2 probes.
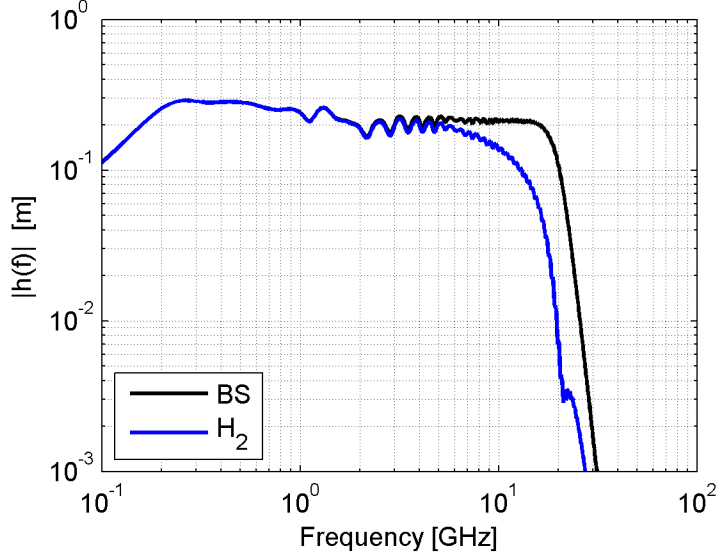
Figure C.2. Magnitude of the transfer function, $|\widetilde{h}|$, for the boresight and H_2 probes. The resemblance to the measured data shown in Figure 3.20 is quite remarkable.

of disagreement between the simulated data and measured data for the IRA-3Q antenna, though the reality is most likely a combination of factors resulting in the observed discrepancies. However, the relationship between the high-frequency content and peak of the impulse response waveform was further reinforced, especially for a nondispersive antenna such as a reflector IRA.

Bibliography

1. *Catalog of UWB Antennas and HV Components*. Specification documents, Farr Fields, LC, 2013. URL `http://www.farr-research.com/FFLC_Catalog.pdf`.

2. "IEEE Standard for Definitions of Terms for Antennas". *IEEE Std 145-2013 (Revision of IEEE Std 145-1993)*, 1–50, March 2014.

3. "The Simulation Method". *CST STUDIO SUITE Help*, 2014.

4. "Time Domain Solver Performance Improvements". *CST STUDIO SUITE Help*, 2014.

5. Baum, C.E. "Radiation of Impulse-Like Transient Fields". *Sensor and Simulation Note 321*, 1989.

6. Baum, C.E. "Some Topics Concerning Feed Arms of Reflector IRAs". *Sensor and Simulation Note 414*, Oct 1997.

7. Baum, C.E. "Selection of Angles Between Planes of TEM Feed Arms of an IRA". *Sensor and Simulation Note 425*, 1998.

8. Baum, C.E., E.G. Farr, and D.V. Giri. "Review of Impulse-Radiating Antennas". W.R. Stone (editor), *Review of Radio Science 1996-1999*. Wiley-IEEE Press, 1999. URL `http://www.farr-research.com/Papers/IRARevGA.pdf`.

9. Bowen, L.H., E.G. Farr, C.E. Baum, T.C. Tran, and W.D. Prather. "Results of Optimization Experiments on a Solid Reflector IRA". *Sensor and Simulation Note 463*, Jan 2002.

10. Cloude, S. *An Introduction to Electromagnetic Wave Propagation & Antennas*. Springer, 1995.

11. Farr, E.G. "A Power Wave Theory of Antennas (Fourth Revision)". *Sensor and Simulation Note 564*, Dec 2014.

12. Farr, E.G., C.E. Baum, and W.D. Prather. "Multifunction Impulse Radiating Antennas: Theory and Experiment". *Sensor and Simulation Note 413*, 1997.

13. Farr, E.G. and C.A. Frost. "Compact Ultra-Short Pulse Fuzing Antenna Design and Measurements". *Sensor and Simulation Note 380*, June 1995.

14. Hardin, J.A. *Information Encoding on a Pseudo Random Noise Radar Waveform*. Master's thesis, Air Force Institute of Technology, 2013.

15. Ludwig, M.T. *UHF Antenna Design for AFIT Random Noise Radar*. Master's thesis, Air Force Institute of Technology, 2012.

16. Manteghi, M. and Y. Rahmat-Samii. "Improved feeding structures to enhance the performance of the reflector impulse radiating antenna (IRA)". *IEEE Transactions on Antennas and Propagation*, 54(3):823–834, March 2006.

17. Manteghi, M. and Y. Rahmat-Samii. "On the characterization of a reflector impulse radiating antenna (IRA): full-wave analysis and measured results". *IEEE Transactions on Antennas and Propagation*, 54(3):812–822, March 2006.

18. Pozar, D.M. *Microwave Engineering*. John Wiley & Sons, 4th edition, 2012.

19. Rosenlind, J. *The Impulse-Radiating Antenna*. Master's thesis, Karlstads University, 2009.

20. Sczyslo, S., H. Thye, G. Armbrecht, S. Dortmund, and T. Kaiser. "Determination of the impulse response of UWB antennas using GTEM cells". *IEEE International Conference on Ultra-Wideband, 2009. ICUWB 2009.*, 753–758. Sept 2009.

21. Tyo, J.S. "Optimization of the TEM feed structure for four-arm reflector impulse radiating antennas". *IEEE Transactions on Antennas and Propagation*, 49(4):607–614, Apr 2001.

22. Tyo, J.S., E.G. Farr, J.S.H. Schoenberg, L.H. Bowen, and L.L. Altgilbers. "Effect of aperture feed and reflector configuration on the time- and frequency domain radiation patterns of reflector impulse radiating antennas". *IEEE Transactions on Antennas and Propagation*, 52(7):1767–1776, July 2004.

23. Valibeiglou, M. and A. Khaleghi. "A reflector impulse radiating antenna (IRA) with a new feeding structure". *8th European Conference on Antennas and Propagation (EuCAP), 2014*, 894–898. April 2014.

24. Wiesbeck, W., G. Adamiuk, and C. Sturm. "Basic Properties and Design Principles of UWB Antennas". *Proceedings of the IEEE*, 97(2):372–385, Feb 2009.

25. Wilson, R.D. IV. *Adaptations and Analysis of the AFIT Noise Radar Network for Indoor Navigation*. Master's thesis, Air Force Institute of Technology, 2013.

List of Acronyms

3D three-dimensional

3FA three feed arm

AFIT Air Force Institute of Technology

CEM computational electromagnetic

CST Computer Simulation Technology

DC direct current

EM electromagnetic

EMP electromagnetic pulse

FD frequency domain

FDTD Finite Difference Time Domain

FFT Fast Fourier Transform

FIT Finite Integration Technique

FWHM full width at half-max

IFFT Inverse Fast Fourier Transform

IRA impulse-radiating antenna

LPD low probability of detection

LPI low probability of intercept

LTI linear, time-invariant

MWS Microwave Studio

NRTF National RCS Test Facility

PCB printed circuit board

PEC perfect electric conductor

RCS radar cross section

RF radio frequency

RF-DNA radio frequency distinct native attributes

TD time domain

TDR time domain reflectometry

TEM transverse electromagnetic

TRP total radiated power

UHF ultra high frequency

UWB ultra-wideband

VHF very high frequency

VSWR voltage standing wave ratio

REPORT DOCUMENTATION PAGE

Form Approved
OMB No. 0704–0188

The public reporting burden for this collection of information is estimated to average 1 hour per response, including the time for reviewing instructions, searching existing data sources, gathering and maintaining the data needed, and completing and reviewing the collection of information. Send comments regarding this burden estimate or any other aspect of this collection of information, including suggestions for reducing this burden to Department of Defense, Washington Headquarters Services, Directorate for Information Operations and Reports (0704–0188), 1215 Jefferson Davis Highway, Suite 1204, Arlington, VA 22202–4302. Respondents should be aware that notwithstanding any other provision of law, no person shall be subject to any penalty for failing to comply with a collection of information if it does not display a currently valid OMB control number. **PLEASE DO NOT RETURN YOUR FORM TO THE ABOVE ADDRESS.**

1. REPORT DATE *(DD–MM–YYYY)*	2. REPORT TYPE	3. DATES COVERED *(From — To)*
26–03–2015	Master's Thesis	Sept 2013 — Mar 2015

4. TITLE AND SUBTITLE

Computational Electromagnetic Studies for Low-Frequency Compensation of the Reflector Impulse-Radiating Antenna

5a. CONTRACT NUMBER

2012-190

5b. GRANT NUMBER

5c. PROGRAM ELEMENT NUMBER

6. AUTHOR(S)

Fillmore, Casey E., Capt, USAF

5d. PROJECT NUMBER

15G104

5e. TASK NUMBER

5f. WORK UNIT NUMBER

7. PERFORMING ORGANIZATION NAME(S) AND ADDRESS(ES)

Air Force Institute of Technology
Graduate School of Engineering and Management (AFIT/EN)
2950 Hobson Way
WPAFB OH 45433-7765

8. PERFORMING ORGANIZATION REPORT NUMBER

AFIT-ENG-MS-15-M-011

9. SPONSORING / MONITORING AGENCY NAME(S) AND ADDRESS(ES)

National RCS Test Facility (96 TG Det 2)
872 DeZonia Dr.
Holloman AFB, NM 88330
DSN 349-3317, COMM 575-679-3317
Email: spencer.sellers@holloman.af.mil

10. SPONSOR/MONITOR'S ACRONYM(S)

NRTF

11. SPONSOR/MONITOR'S REPORT NUMBER(S)

12. DISTRIBUTION / AVAILABILITY STATEMENT

DISTRIBUTION STATEMENT A:
APPROVED FOR PUBLIC RELEASE; DISTRIBUTION UNLIMITED.

13. SUPPLEMENTARY NOTES

This material is declared a work of the U.S. Government and is not subject to copyright protection in the United States.

14. ABSTRACT

The reflector impulse-radiating antenna (IRA) is considered to meet the requirement for a wideband, directional antenna with short temporal response and small electrical footprint. Standard reflector IRA designs are modeled and performance is simulated using full-wave computational electromagnetic (CEM) software. Characterization of the standard designs reveals the possible existence of wide, frequency-independent backlobes containing nearly 40% of the radiated power at high frequencies. These undesirable backlobes have never been hypothesized, predicted or measured, likely due in part to their alignment outside the primary measurement planes.

At the lowest operating frequencies, the reflector IRA is unaffected by backlobes, but is characterized by low radiation efficiency and high resistive losses. Simulated studies are conducted to identify options for enhancing the low-frequency performance of the reflector IRA, including novel multi-arm feed structures and varied resistor distributions and values in the matching circuit component of the antenna design. Both techniques are predicted to provide viable options for enhancing and tuning the performance of the reflector IRA at low frequencies.

15. SUBJECT TERMS

16. SECURITY CLASSIFICATION OF:			17. LIMITATION OF ABSTRACT	18. NUMBER OF PAGES	19a. NAME OF RESPONSIBLE PERSON
a. REPORT	b. ABSTRACT	c. THIS PAGE			Dr. Peter J. Collins, AFIT/ENG
U	U	U	UU	136	19b. TELEPHONE NUMBER *(include area code)* (937) 255-3636, x7256; peter.collins@afit.edu

Standard Form 298 (Rev. 8–98)
Prescribed by ANSI Std. Z39.18